ATOMIC AND NUCLEAR INTERFERENCE AND COHERENCE PHENOMENA AND THEIR APPLICATIONS

A Dissertation

by

YELENA ANATOLYEVNA KUZNETSOVA

Submitted to the Office of Graduate Studies of
Texas A&M University
in partial fulfillment of the requirements for the degree of

DOCTOR OF PHILOSOPHY

May 2005

Major Subject: Physics

ATOMIC AND NUCLEAR INTERFERENCE PHENOMENA

AND THEIR APPLICATIONS

A Dissertation

by

YELENA ANATOLYEVNA KUZNETSOVA

Submitted to Texas A&M University
in partial fulfillment of the requirements
for the degree of

DOCTOR OF PHILOSOPHY

Approved as to style and content by:

Olga Kocharovskaya (Chair of Committee)	
Edward S. Fry (Member)	George R. Welch (Member)
Timothy R. Hughbanks (Member)	Edward S. Fry (Head of Department)

May 2005

Major Subject: Physics

ABSTRACT

Atomic and Nuclear Interference Phenomena
and Their Applications. (May 2005)
Yelena Anatolyevna Kuznetsova, B.S., Nizhny Novgorod State University, Russia;
M.S., Nizhny Novgorod State University, Russia
Chair of Advisory Committee: Dr. Olga Kocharovskaya

In this work, interference and coherence phenomena, appearing in atomic and molecular ensembles interacting with coherent light sources, as electromagnetically induced transparency (EIT), coherent population trapping (CPT), and slow group velocity of light are investigated. The goal of the project is to make the steps towards various applications of these phenomena, first, by studying them in solid media (which are the most advantageous for applications), second, by suggesting some novel applications such as CPT-based plasma diagnostics, and realization of new types of solid-state lasers (based on suppression of excited-state absorption via EIT). The third goal of the project is extension of coherence and interference effects well-known in optics to the gamma-ray range of frequencies and, correspondingly, from atomic to nuclear transitions. A particular technique of chirped pulse compression applied to Mössbauer transitions is considered and the possibility of compression of Mössbauer radiation into ultrashort gamma-ray pulses is analyzed.

The theoretical treatment of the interference and coherence effects is based on the semiclassical description of atom-light interaction, which is sufficient for correct analysis of the phenomena considered here. Coherent media are considered in two-, three-, and four-level approximations while their interaction with light is studied both analytically and numerically using the Maxwell-Bloch set of equations.

To my parents, Zinaida and Anatoly

ACKNOWLEDGMENTS

It is my pleasure to thank all those who helped me to complete this degree. First, I wish to say a very fond "thank-you" to my advisor, Professor Olga Kocharovskaya, who guided me in optics and physics in general, directed me into interesting projects and taught me by example what it takes to be a scientist. I am very grateful to Roman Kolesov, my husband and co-worker, whose devotion to physics always served as an inspiration for me, who constantly supported and helped me both scientifically and emotionally. I would like to thank my co-workers, Farit Vagizov, Yuri Rostovtsev, and Rinat Akhmedzhanov, who were a great help to me in my research and from whom I benefited tremendously.

Finally, I want to thank my friends, both here and in Russia, for years of support, advice and encouragement.

TABLE OF CONTENTS

CHAPTER Page

LIST OF TABLES

TABLE Page

LIST OF FIGURES

FIGURE Page

FIGURE Page

FIGURE Page

FIGURE Page

CHAPTER I

INTRODUCTION

Observation by R.W. Wood and A. Ellet [1] and interpretation by W. Hanle [2] of resonance fluorescence signal depolarization by an external magnetic field in mercury vapour started in 1924 the history of atomic and nuclear interference and coherence phenomena. This effect named after Hanle is a direct consequence of the Zeeman coherence created in the excited state by excitation with coherently polarized light. The phenomenon can be described as the result of a quantum-mechanical interference between the scattering amplitudes for the two possible routes from the ground state to the excited state and back. This quantum-mechanical interference manifests itself as a change in the polarization of the scattered resonance radiation as the separation of the Zeeman sub-levels of the excited level is varied. The interference effect disappears when these levels are separated by more than their width Γ. The Hanle effect provides a very reliable technique for measuring the lifetimes of excited levels of atoms and molecules. In fact, the Hanle effect together with the level-crossing phenomenon, which is its extension to nonzero magnetic fields and non-degenerate states, have long been the only available Doppler-free spectroscopic techniques [3]. Nowadays atomic coherence and interference phenomena include so well-studied effects as self-induced transparency [4]; spin [5], photon [6], and Raman [7] echoes; quantum [8], and Raman [9] beats; autoionization Fano-resonances [10], etc., and a wealth of coherent phenomena observed in radio-frequency/microwave-optical double resonance experiments such as Raman heterodyne technique [11], photon-echo nuclear double resonance [12], optical-pumping double resonance [13], coherent optical

---

The journal model is Physical Review A.

double resonance [14]. They found numerous applications in atomic and molecular spectroscopy.

In the last decade new interference phenomena, Coherent Population Trapping (CPT), Lasing Without Inversion (LWI) and Electromagnetically Induced Transparency (EIT), discovered in the late 1970s by G. Alzetta *et al.*, and H.R. Gray *et al.* [15], independently predicted in the works of O. Kocharovskaya and Y. Khanin, S.E. Harris and M.O. Scully in the late 1980s [16] - early 1990s [17], respectively, attracted enormous attention due to their unusual properties and potential applications. These interference phenomena take place in multilevel atomic and molecular systems interacting with coherent electromagnetic fields. The simplest system in which they are observed is a three-level atomic or molecular system, shown in Fig.1, coupled to two laser fields in such a way that the laser driven transitions are dipole allowed while the third transition, typically Zeeman or hyperfine, is dipole forbidden. The interference occurs between transition pathways induced by the fields within the internal quantum states of atoms and molecules. It can lead to dramatic modifications of the optical response of the system. In particular, absorption of a probe field tuned in resonance to some transition can be cancelled leading to an initially opaque medium being rendered transparent for the probe field. This effect is termed Electromagnetically Induced Transparency [18] owing to the fact that the transparency for the probe field is induced by another electromagnetic, called driving or control, field(s). First the destructive interference of this type leading to cancellation of the total transition probability was discovered by Fano [10] who found that the ionization rate of an atom shows pronounced reduction when the ionization can occur both by direct excitation into the continuum and by a transition to an auto-ionizing state, having bound-state character and lying in the continuum, followed by a rapid radiationless transition to the continuum. As was shown by Heller and Popov [19], this Fano-type interference

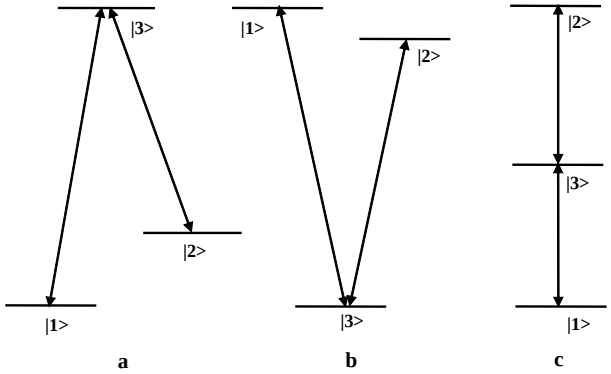

Fig. 1. Generic three-level atomic or molecular systems coupled with two electromagnetic fields in which the interference effects are most easily realized: a) Λ scheme; b) V scheme; c) ladder scheme.

can be realized even in the absence of the auto-ionizing state if an additional laser field couples some bound state to the continuum. In this way it admixes the bound state to the continuum thus creating an analog of an auto-ionizing state. This admixed state was named Laser Induced Continuum Structure [20].

The interference between transition pathways requires that the atomic or molecular system be in a superposition of its mutually coherent quantum states. The coherently prepared medium was named "phaseonium" [21]. It demonstrates a number of new phenomena among which are Coherent Population Trapping [22]; Coherent Population Transfer [23]; the possibility of manipulation of the group velocity of a light pulse propagating in the medium, i.e. to reduce it down to a few meters per second [24] or even bring the pulse to a complete stop [25], imprint the quantum state carried by pulse photons into a superposition of long-lived spin states of atoms and to later retrieve it with (ideally) no losses [26], thus realizing the first steps toward optically carried quantum information storage and processing and quantum computing.

Coherent Population Trapping was first observed by Alzetta [15] as suppression of resonant fluorescence from sodium vapor in the presence of a multimode laser field

applied to the Λ configuration of energy states shown in Fig.1a when the frequency difference of the laser modes matched the frequency difference of the ground hyperfine levels (two-photon resonance condition). In the absence of relaxation processes the probability amplitude of the excited state $|3>$ is governed by the equation:

$$\frac{\partial c_3}{\partial t} = i\left(\Omega_1 c_1 e^{i\Delta_{31}t} + \Omega_2 c_2 e^{i\Delta_{32}t}\right) = i\left(\Omega_1 c_1 e^{i\Delta t} + \Omega_2 c_2\right) e^{i\Delta_{32}t}, \tag{1.1}$$

where the laser fields are defined via their Rabi frequencies $\Omega_{1,2} = \mu_{31,32}E_{1,2}/2\hbar$ with $\mu_{31,32}$ and $E_{1,2}$ being the dipole moment matrix elements of the transitions $|3> \leftrightarrow |1>$ and $|3> \leftrightarrow |2>$ and slowly varying amplitudes of the laser field electric components, respectively; c_1, c_2 and c_3 are the probability amplitudes of the corresponding states in the interaction representation; $\Delta_{31,32} = \omega_{31,32} - \omega_{1,2}$ are the detunings of the laser fields, having frequencies $\omega_{1,2}$, from the corresponding transitions whose frequencies are $\omega_{31,32}$; $\Delta = \omega_{21} - (\omega_1 - \omega_2)$ is the two-photon detuning of the fields with respect to the dipole forbidden $|2> \leftrightarrow |1>$ transition. In the situation of exact two-photon resonance when $\Delta = 0$ Eq.(1.1) shows that there is a particular superposition of lower levels: $c_1/c_2 = -\Omega_2/\Omega_1$ from which atoms are not excited to the upper state, thus producing no fluorescence. This "dark" or "trapped" and orthogonal to it "bright" states are defined as:

$$|d> = \frac{\Omega_2}{\Omega}|1> - \frac{\Omega_1}{\Omega}|2>, \tag{1.2}$$

$$|b> = \frac{\Omega_1}{\Omega}|1> + \frac{\Omega_2}{\Omega}|2>, \tag{1.3}$$

where $\Omega = \sqrt{\Omega_1^2 + \Omega_2^2}$ is the effective Rabi frequency of the fields. The "dark" state is completely decoupled from the excited state and once the system is in this state it becomes transparent for the applied optical fields. The "bright" state is coupled to the excited state and eventually all its population is transferred to the "dark" state by

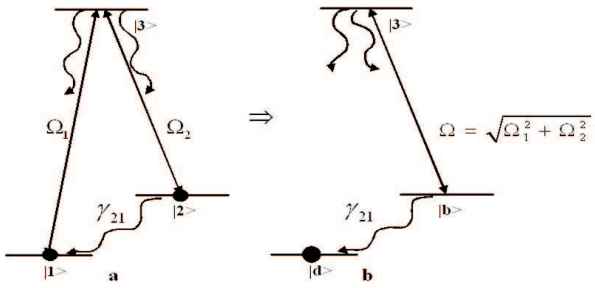

Fig. 2. a) The Λ energy level scheme interacting with two cw electromagnetic fields in which CPT is typically observed; b) Alternative description in terms of "dark" $|d>$ and "bright" $|b>$ states, illustrating population transfer into the "dark" state by optical pumping.

the excited state spontaneous decay which goes into both states, so that the medium ends up in a coherent superposition of lower states given by Eq.(1.2) and no longer interacts with the fields (see Fig.(2)).

When both electromagnetic fields are of comparable strength, both lower levels have comparable populations in the "dark" state. If one of the fields is much stronger than the other, for example $\Omega_2 \gg \Omega_1$, as follows from Eq.(1.2) the "dark" state in this situation coincides with $|1>$ (EIT situation). The system being pumped into the "dark" state leads to vanishing of the imaginary part of the susceptibility, linear in the probe field strength, at two-photon resonance between the probe and control fields. The susceptibility consists of two terms, the first one describes the direct absorption process at the $|1> \rightarrow |3>$ transition, the second one is responsible for the second possible path to the upper state involving the state $|2>$, namely, it includes processes as $|1> \rightarrow |3> \rightarrow |2> \rightarrow |3>$, $|1> \rightarrow |3> \rightarrow |2> \rightarrow |3> \rightarrow |2> \rightarrow |3>$, etc. The second term has a negative sign with respect to the first one and, if the state $|2>$ is metastable, these terms exactly cancel each other. The probe absorption profile, determined by the imaginary part of the linear susceptibility, shows a narrow

dip at exact two-photon resonance. The width of the resonance is determined neither by the Doppler nor by the homogeneous/radiative widths of the transitions to the upper state but rather by the decay rate of the phase coherence between amplitudes of states $|1>$ and $|2>$, which can be extremely small if the state $|2>$ is metastable. It is worth noting that while CPT deals with an atomic response in the presence of external fields, EIT, LWI and slow light describe self-consistent nonlinear propagation of a bichromatic field through an optically thick resonant medium. The essence of EIT is the possibility of propagation without absorption of a two-component strong field under the condition of two-photon resonance while each component would be strongly absorbed if propagates through the medium alone. According to the Kramers-Kronig relation [27], a narrow dip in the imaginary part of the linear susceptibility is accompanied by a steep non-anomolous dispersion feature in the real part of the susceptibility. As was pointed out in [28], this dispersion can result in a small group velocity of a light pulse propagating in a medium with EIT when the intensity of the pulse is small compared to the intensity of the control field. This prediction was confirmed later in a large number of experiments in gases, both hot and cold (BEC), and solid-state materials, mostly in transition metal and rare-earth ion doped crystals and semiconductors. The possibility of changing the velocity of a light pulse by adjusting the intensity of an external control field is promising for devices such as optical buffers and optical delay lines. As was mentioned above, this property of the EIT effect allows one to map quantum states of photons of the probe pulse into spin excitations of coherently driven atomic media. This happens due to existence in the EIT medium of a combined excitation of photons of the probe field and spins, called a "dark-state" polariton [26]. Its properties, namely, propagation velocity and the ratio of photonic and spin components, is governed by an external classical control field. By adiabatically switching the control field off the polariton can be made completely spin-like

and stopped, which results in the mapping of the photonic quantum state onto spin states of an atomic ensemble. Later on the probe pulse can be retrieved by switching the control field on and it will have the same quantum state as before.

EIT makes possible nonlinear mixing processes under the two-photon condition. Indeed, nonlinear interactions are greatly enhanced at resonance, however, linear absorption is also greatly enhanced. EIT allows one to eliminate linear absorption leaving unchanged or even enhanced higher order susceptibilities (for example, second and third) due to constructive interference of probability amplitudes [29]. Since the control field threshold intensity required to establish EIT is typically much less than the saturation intensity, it makes possible to realize nonlinear effects at the intensity level corresponding to a single photon [30]. Using EIT many well-studied and new nonlinear phenomena such as nonlinear frequency conversion [31] up to vacuum ultraviolet frequency range [32], optical phase conjugation [33], four-wave mixing [34], etc. can be realized with much lower laser intensities. Recently, four-wave mixing in cold ^{87}Rb atoms was demonstrated requiring extremely low pump powers of a few nanowatts and energies of less than a picojoule [35]. EIT results also in resonantly enhanced Kerr nonlinearities with extremely low-power laser fields [36], which could be used in Cavity Quantum Electrodynamics as a means for enhancing photon-photon interaction strength in a cavity under conditions of weak atom-cavity field coupling, which is essential for realization of some quantum logic operations [37]. It also became a basis of the so-called "nonlinear optics with maximum coherence", when a medium initially prepared in a superposition state having large atomic or molecular coherence serves as a local oscillator for nonlinear frequency conversion with an exceptionally high conversion efficiency [38]. This technique was used to generate a broad spectrum of optical sidebands due to refractive index modulation of the medium by two laser fields applied in almost two-photon resonance with a pair of molecular states in

molecular deuterium [39]. The generated spectrum of sidebands can be compressed into a train of subfemtosecond pulses; in a recent work [40] a single-cycle optical pulse of 0.5 fs duration was obtained using this technique.

It was recognized early that by using quantum interference to suppress absorption while having stimulated emission unaffected lasers with reduced pump intensity, or even without population inversion, can be realized [41]. LWI holds promise for obtaining laser action in spectral domains, e.g. the x-ray and gamma-ray range, where conventional methods requiring population inversion and thus incoherent pump scaling with the transition frequency at least as ν^3 necessary to overcome spontaneous emission from the metastable laser level are not available or difficult to implement [42]. Incoherent pumping of population into upper states can also lead to appearance of spectral regions with a resonantly enchanced refractive index [43] with at the same time vanishing absorption.

Extremely narrow resonances associated with EIT and CPT can be naturally applied for high-precision measurements, spectroscopy, and metrology, for example, atomic clocks [44] and magnetometry [45].

One of the directions in nuclear spectroscopy attracting now a lot of attention is application of optical techniques in the gamma-ray range of frequencies (mostly to Mössbauer nuclear transitions owing to their narrow widths). This is a promising approach since optical methods are already well-developed and understood. Thus their extension to gamma rays would allow one to combine benefits of widely and successfully used optical methods with advantages of an extremely short wavelength of a gamma photon. It is especially interesting to extend interference phenomena to gamma-rays, because they would offer the possibility of fine manipulation of gamma photons. Such interference phenomenon as quantum beats resulting from different transitions in a nucleus has long been observed at Mössbauer transitions [46]. An-

other interesting effect also resulting from interference of probability amplitudes of transitions originating from initially phased states was observed recently [47]: the radiative decay rate of a radioactive nucleus ^{57}Fe in $^{57}FeBO_3$ was controlled by abrupt (within the natural decay time of a nucleus excited state) switching of a crystal magnetization. Namely, when an external magnetic field controlling magnetization was switched off the coherent nuclear decay was significantly reduced. Switching back at later times restored it, starting with an intense radiation spike. Suppression and restoration of the coherent nuclear decay originate in this experiment from drastic changes of the nuclear states and of the interference within the nuclear transitions caused by the magnetic switching. The central idea was to study the possibility of storing excitation energy by suppressing the coherent decay and releasing the stored energy later.

As was already mentioned before, such interference effect as LWI holds promise for resolving the long-standing problem of a gamma-ray laser. Work in this direction has already started in 90's with observation of Rabi-splitting of a Mössbauer resonance line due to radio-frequency driving of the hyperfine-split ground state of a composite nuclear-electronic system [48]. The next step was a demonstration of an analog of electromagnetically induced transparency for gamma rays, when gamma radiation absorption in a resonant Mössbauer absorber was reduced due to interference between two paths from excited state hyperfine sublevels to a common ground state [49]. The sublevels were moved to the point of level crossing by a dc magnetic field collinear to the electric field gradient axis of the absorber material, and a dc transverse magnetic field produced an anti-crossing effect, mixing the sublevels thus giving rise to a coherence between them which resulted in the interference and absorption suppression. Recently, it has been suggested in Ref.[50] that the coherent effects can also be observed at the Mössbauer transitions via optical driving of electronic transi-

tions. Various modifications of Mössbauer gamma-ray absorption spectra (splitting, shifting, broadening, and narrowing of lines) by a coherent optical driving field have been predicted.

Most coherence and interference effects with Mössbauer radiation are though observed in scattering experiments as the radiation field emitted by a radioactive spontaneously decaying nuclear source interferes with the absorbed and re-emitted (forward scattered) radiation field of the resonant absorber. If a phase of the Mössbauer source radiation field is rapidly shifted by π, then the so-called gamma-echo is observed [51]. The explanation for this effect is that the phase shift turns the destructive interference between the source and scattered radiation into constructive one resulting in an echo. Interference can also take place between forward scatterred waves, and a nuclear exciton is the most famous example [52]. The exciton is the delocalized excited state of an ensemble of nuclei created by a single gamma-quantum. In other words, it is a spatially coherent superposition of excited states of all nuclei in the ensemble, in each contributing term of the superposition one nucleus is excited with a definite probability amplitude while all others are in the ground state. When the phase correlation of the partial nuclear excitations is preserved during the lifetime of the excited state, interference of the waves re-radiated by the nuclei occurs and a coherent radiation field is built up in nuclear resonant scattering. The development of synchrotron radiation sources allowed to observe new coherence phenomena in nuclear forward scattering, including the nuclear exciton, due to the fact that the excitation by a synchrotron radiation pulse is short compared to the nucleus excited state lifetime and the forward scattering is well separated in time from excitation. In the experiments with a Mössbauer source the forward scattered radiation is always coupled with the incident radiation. This led to observation of such effects stemmimg from the exciton formation as super-radiance [53], manifested as a huge increase of the

coherent scattering intensity, and a speeding up of the nuclear decay, and dynamical beats (modulation of the scattered intensity in time and in space, which is related to sequential absorptions and re-emissions of gamma-photons by nuclei) [54].

The techniques, described above, which are based on interference within nuclear transitions or different components of scattered fields, become complementary to traditional Mössbauer spectroscopy. Their advantage is that they utilize not only the amplitude, but also the phase of the radiation field, while the traditional spectroscopy deals only with the strength of the field. Thus interference techniques provide refined information about hyperfine interactions.

This research project pursues two major goals. First, to apply the coherence and interference effects discussed above to media, such as doped crystals and plasma, which are relatively less explored compared to gaseous media, suggesting along the way new applications, including CPT - based magnetic field diagnostics in plasmas and suppression of excited-state absorption in laser crystals. The second goal is to extend the range of frequencies available for interference phenomena from optical to gamma-ray range by studying them at nuclear transitions. A particular technique of chirped pulse compression, well-known in optics, is considered in the project applied to Mössbauer transitions and the possibility of compression of Mössbauer radiation into ultrashort pulses is analyzed.

The organization of the dissertation is as follows. In Chapter II a method of magnetic field diagnostic in a plasma, based on the coherent population trapping effect, is considered. Theory and experiment are presented, demonstrating the capability of the technique to measure both the strength and the orientation of the field. Estimates are given for the range of plasma parameters where the method can be applied.

In Chapter III a theoretical analysis of the basic requirements necessary for realization of atomic interference and coherence phenomena: EIT, CPT, slow light

and low-intensity nonlinear interactions, in solids is carried out. A class of materials, namely, rare-earth and transition metal ion doped crystals, which are known to have both narrow optical and spin transitions, is considered. Estimates are derived for required laser intensities and expected efficiency of nonlinear interactions in these materials.

In Chapter IV a method of suppression of excited-state absorption (ESA) preventing laser action in many laser crystals is considered, using the effect of electromagnetically induced transparency. Estimates for the efficiency of ESA reduction and required intensities of the driving field are presented for typical parameters of dielectric host materials doped with rare-earth ions. Two particular crystals are considered in more detail, in which ESA suppression may result in laser action in the ultraviolet and visible regions. Next, a pulsed regime of amplification in a crystal with suppressed excited-state absorption is analyzed. Evolution of the probe and control fields is studied both analytically and numerically. Estimates for the ultimate probe pulse intensity, temporal width, and velocity are given for the amplifiers made of rare-earth ion doped crystals.

In Chapter V the possibility to realize the well-known in optics chirped-pulse compression technique in the gamma frequency range in order to produce short pulses of Mössbauer radiation is theoretically considered.

CHAPTER II

MAGNETIC FIELD DIAGNOSTIC OF PLASMAS BASED ON COHERENT POPULATION TRAPPING

A detailed knowledge of an internal magnetic field is of great importance in various fields of science and applications. Biomedical applications mostly rely on SQUID (superconducting quantum interference device) detectors [55], in geophysics and archaeology optical pumping magnetometers [56] are used. The idea of using ultranarrow coherent population trapping resonances for high-resolution magnetometry was proposed by M.O. Scully and M. Fleischhauer [45]. Later this idea was realized experimentally in a number of groups (D. Budker, *et al.* [45], A. Nagel, *et al.* [45], I. Novikova, *et al.* [45]), the magnetometric techniques utilized either absorptive or dispersive (Nonlinear Magneto-Optical Rotation) properties of the transparency resonance. CPT-based magnetometers that use alkali metal vapors achieve sensitivities of ~ 1 fT $\mathrm{Hz}^{-1/2}$ [57], comparable to the SQUID sensitivity, and can be successfully applied to measure small changes of magnetic fields. Recently a millimiter size CPT-based magnetic sensor was realized in a sodium vapor with a sensititvity of 50 pT $\mathrm{Hz}^{-1/2}$ [58], integrated on a chip and potentially scalable to even smaller size.

It looks attractive to apply the same technique to measure magnetic fields in a plasma, since CPT resonances can be observed in a fluorescence signal, thus permitting spatially localized detection of the magnetic field. Namely, if the plasma contains atoms or ions with magnetic field dependent level splitting (Zeeman or hyperfine), then resonant fluorescence from these test particles vanishes, provided that the frequency difference of two laser beams sent through the plasma exactly matches the frequency of the split transition.

The spectral resolution of the CPT signal is determined by the minimum width of

the resonance in the fluorescence signal. It is given basically by the Zeeman sublevel coherence decay rate for the unsaturated CPT limit, when the laser field intensities do not significantly exceed the threshold value, necessary for CPT to be establish. This threshold intensity is typically lower than the intensity required to saturate an optical transition. The Zeeman coherence decay rate can be orders of magnitude smaller than the optical transition's natural and Doppler widths, which makes the spectral resolution of the CPT signal quite high.

A number of techniques are used to measure magnetic fields in plasmas [59]. The most popular one utilizes external or internal probes, which are basically wire coils. External probes measure a magnetic field distribution outside the plasma and reconstruction methods are applied to calculate the internal fields. Internal probes are inserted into the plasma and detect the field directly. The coils can measure small flux densities with a less than millimiter spatial resolution and temporal resolution given by the integration time of an integrating curcuit. The drawbacks of the colis are: first, they disturb the plasma and are not applicable in hot plasmas, and second, they respond to the rate of change of the field, not the field itself, which limits their efficiency in detection of steady fields. Other methods are mostly laser-aided, they use either Faraday rotation of e.m. field polarization if the magnetic field is present in the plasma, or laser-induced fluorescence collected from particles naturally present in the plasma or intentionally sent in for test purposes [60]. The Faraday effect gives a line-of-sight integral of the field, thus the corresponding diagnostic is not local. The method using laser-induced fluorescence detection is local, since a crossed exciting and viewing beams are used, meaning that the fluorescence is observed from a well-defined region. The laser-induced fluorescence technique, though, typically has poor accuracy, since the fluorescence comes from Zeeman split transitions not resolved because of large Doppler broadening. In order to get rid of the Doppler broadening

an energetic neutral beam is usually injected into the plasma. A lithium beam is typically used, since lithium has lines to the groud state of long (visible) wavelength (670.8 nm). The main difficulty here is to produce a beam sufficiently energetic to penetrate the plasma but sufficiently monoenergetic as not to obscure the Zeeman splitting by the Doppler broadening. Another way to measure both the strength and the direction of the magnetic field with the help of neutral beams (especially hydrogen beams) is to utilize the motional Stark effect, when significant linear Stark energy shifts are induced due to fast movement of neutral atoms in the magnetic field. Sometimes solid pellets (often made of neutral lithium) are injected into the plasma; while moving through the plasma, the pellet's boundary gets ablated, lithium atoms in the surrounding cloud become excited and reradiate at some characteristic wavelength, due to the magnetic field the emission profile will show Zeeman splitting, allowing to determine the magnitude of the field. The direction of the field can be measured by viewing the emission from ionized atoms from the pellet, since they will be moving along the lines of the field.

The general idea of the CPT-based method of magnetic field measurement in plasmas is illustrated schematically in Fig.3 and can be explained in the following way. Suppose that two laser beams with close wavelengths propagate in a plasma and intersect at the point of interest, where the magnetic field is to be measured. It is assumed that the plasma contains atoms or ions with an optical transition close to a resonance with the optical field and ground or/and excited state of this transition is split by the magnetic field into a set of Zeeman sublevels. By adjusting the frequencies of the laser beams, the two-photon resonance condition can be satisfied and the CPT dip in the fluorescence profile will be detected. By measuring the fluorescence spectrum from the intersection volume of the two beams as a function of their frequency shift, the magnetic field magnitude and direction can be deduced from the positions

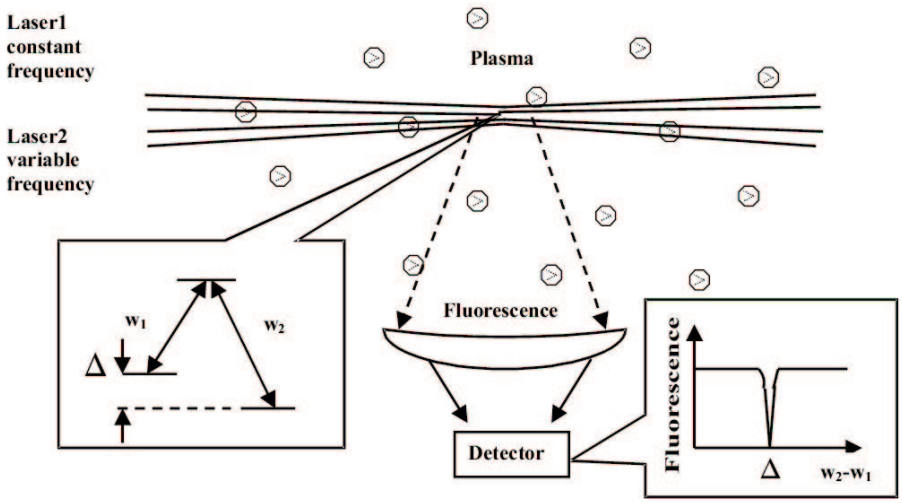

Fig. 3. Schematic of the diagnostic method.

and amplitudes of the CPT resonances, as is shown below. This idea was suggested and realized experimentally in our works [61, 62]. A similar technique was developed independently and used recently in two-dimensional (2D) imaging of spatially inhomogeneous magnetic fields [63]. It was realized experimentally in a Na atomic vapor, though, not in a plasma. It allows one to obtain 2D contours of constant magnetic field in alkaline atomic vapors with high field resolution of the order of $1 - 100$ mG.

A. Theoretical background

The simplest atomic system suitable for the technique is a four-level system, depicted in Fig.4, where the upper level is a singlet and the lower level is a triplet state. An external magnetic field splits it into three Zeeman sublevels with level separation equal to the Larmor frequency $\omega_L = g\mu_B B/\hbar$. Here g is the Lande factor of the lower level, μ_B is the Bohr magneton, B is the magnetic field strength.

Consider two electromagnetic waves E_1 and E_2 with frequencies ω_1 and ω_2, respectively, both propagating in the z-direction. The waves are linearly polarized such

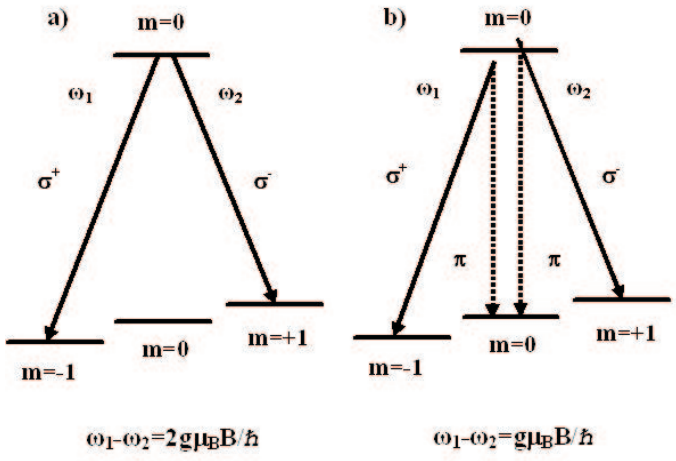

Fig. 4. Laser-coupling schemes, showing CPT resonance configurations in the atomic system, studied in the experiment.

that either $\mathbf{E_1}, \mathbf{E_2} || \hat{\mathbf{e}}_\mathbf{x}$ or $\mathbf{E_1}, \mathbf{E_2} || \hat{\mathbf{e}}_\mathbf{y}$ with $\hat{\mathbf{e}}_\mathbf{i}$ being the unit vector of the i polarization. The arbitrarily oriented magnetic field is described by the angles α and β, see Fig.5. We choose the quantization axis along $\mathbf{k} || \hat{\mathbf{e}}_\mathbf{z}$.

For a given magnetic field, depending on the selection rules for the angular momentum, which are determined by laser field polarizations and magnetic field orientation, CPT resonances will be observed in a fluorescence spectrum whenever the two-photon resonance condition is satisfied:

$$\omega_1 - \omega_2 = \pm\omega_L, \pm 2\omega_L.$$

In the case $\mathbf{B}$ is along $\mathbf{k}$, each linearly polarized e.m. field can be decomposed into a combination of σ^+ and σ^- components, for which only transitions with $\Delta m = \pm 1$ are respectively allowed. Therefore, if the two-photon detuning is varied, only the CPT resonance at the double Larmor frequency, when $\omega_1 - \omega_2 = \pm 2\omega_L$, will be observed (Fig.4a). The situation is changed if the magnetic field is tilted with respect to $\mathbf{k}$ such that it now has a projection on the e.m. wave polarization direction.

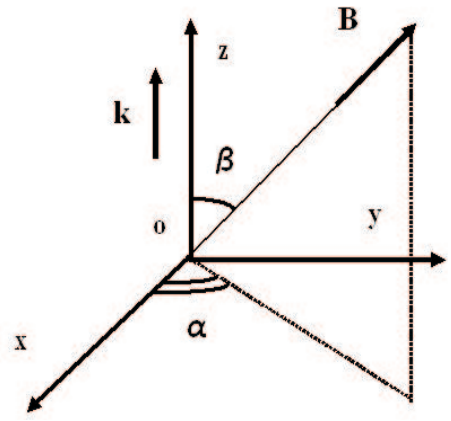

Fig. 5. Magnetic field orientation.

In this case selection rules also allow for the transition with $\Delta m = 0$ due to the fact that the e.m. fields now have an admixute of a π component. As a result an additional resonance appears at the single Larmor frequency $\omega_1 - \omega_2 = \pm\omega_L$ (Fig.4b). A theoretical analysis of the interaction of two laser fields with the four-level system, depicted in Fig.4a, shows that the magnetic field orientation can be determined from the ratio of the fluorescence intensities of the CPT resonances at single and double Larmor frequencies. The main assumptions used in the analysis are: 1) the laser field intensities do not significantly exceed the CPT saturation limit; 2) the Doppler width of the optical transition exceeds the Zeeman splitting; 3) the homogeneous linewidth of the optical transition is smaller than the Zeeman splitting; 4) an average over the distribution of optical transition frequencies due to the Doppler effect is carried out.

The fluorescence intensity is proportional to a steady-state upper level population ρ_{44}. In the Λ-system of Fig.4a formed by the σ^--component of the first field and the σ^+-component of the second field, ρ_{44} reduction $\Delta\rho_{44}$ owing to CPT is proportional to the product of the intensities of the laser fields resonantly applied to the arms of the system, each intensity being multiplied by the strength of the corresponding

transition, given by the square of the dipole moment:

$$\Delta\rho_{44} \sim I_1 \left|\mu_{41}^1\right|^2 \times I_2 \left|\mu_{43}^2\right|^2 \sim \left|\Omega_1^{41}\right|^2 \left|\Omega_2^{43}\right|^2,$$

where I_1, I_2 are the laser field intensities, μ_{41}^1, μ_{43}^2 are the dipole moments of the $4 \rightarrow 1$, $4 \rightarrow 3$ transitions, which take into account the field polarizations, and the Rabi frequencies of the laser fields are

$$\Omega_j^{4i} = \frac{\mu_{4i}^j E_j}{2\hbar} = \frac{\mu E_j}{2\hbar} f_{4i}(\alpha, \beta) = \Omega_j f_{4i}(\alpha, \beta),$$

where the indicies $i = 1, 2, 3$ and $j = 1, 2$ denote the Zeeman sublevels of the lower level and laser fields, respectively; μ contains an integral over the radial parts of the lower and upper state wave functions; $\Omega_j = \mu E_j / 2\hbar$ are the angular independent Rabi frequencies of the laser fields; and $f_{4i}(\alpha, \beta)$ gives the angular dependence of the dipole moment. For identical polarizations f_i is the same for E_1 and E_2.

In the case of resonance at the single Larmor frequency, shown in Fig.4b, two Λ-schemes are formed by the $\sigma^{-(+)}$ and π-components of the fields. These Λ schemes are resonant with different groups of atoms, simmetrically Doppler-shifted with respect to the central frequency of the optical transition. The two groups give contributions to ρ_{44} proportional to $\left|\Omega_1^{41}\right|^2 \left|\Omega_2^{42}\right|^2$ and $\left|\Omega_1^{42}\right|^2 \left|\Omega_2^{43}\right|^2$, respectively. In the unsaturated CPT limit, when $\left|\Omega_1\right|^2 + \left|\Omega_2\right|^2 \sim \Gamma W_D$ (Γ is the Zeeman coherence decay rate, W_D is the optical transition Doppler linewidth [64]), the proportionality coefficients containing information about the resonance profiles turn out to be identical for the three Λ systems, considered above.

The ratio of the fluorescence intensities is then given by the following expression:

$$r = \frac{I^{w_1 - w_2 = w_L}}{I^{w_1 - w_2 = 2w_L}} = \frac{\left|\Omega_1^{41}\right|^2 \left|\Omega_2^{42}\right|^2 + \left|\Omega_1^{42}\right|^2 \left|\Omega_2^{43}\right|^2}{\left|\Omega_1^{41}\right|^2 \left|\Omega_2^{43}\right|^2}. \tag{2.1}$$

For the case $\mathbf{E_1}, \mathbf{E_2} || \hat{\mathbf{e}}_\mathbf{x}$,

$$f_{41} = -f_{43}^* = i \sin\alpha + \cos\alpha \cos\beta,$$

$$f_{42} = -\sqrt{2} \sin\beta \cos\alpha.$$

The ratio of intensities Eq.(2.1) has the form:

$$r_x = \frac{4 \sin^2\beta}{\tan^2\alpha + \cos^2\beta}.$$

For the case $\mathbf{E_1}, \mathbf{E_2} || \hat{\mathbf{e}}_\mathbf{y}$,

$$f_{41} = -f_{43}^* = -i \cos\alpha + \sin\alpha \cos\beta,$$

$$f_{42} = -\sqrt{2} \sin\beta \sin\alpha.$$

This time the ratio Eq.(2.1) is given by:

$$r_y = \frac{4 \sin^2\beta}{\cot^2\alpha + \cos^2\beta}.$$

From r_x and r_y one can determine $\cos^2\beta$ and $\tan^2\alpha$. This gives one four possible directions of the magnetic field. In order to choose the right one, some additional knowledge about the magnetic field geometry is required. The anvantage of this method is that $r_{x(y)}$ is independent of the intensities of the fields and is determined only by the geometry of the experiment.

B. Experimental results

To demonstrate the feasibility of the described technique we performed an experiment in a plasma of a low-pressure glow neon discharge. The neon atomic energy levels are shown in Fig.6. The electric-dipole allowed transition $2p^5 3s^3P_1(J=1) \rightarrow 2p^5 3p^3P_0(J=0)$ of wavelength 607.4 nm was chosen for a number of reasons: 1) it is

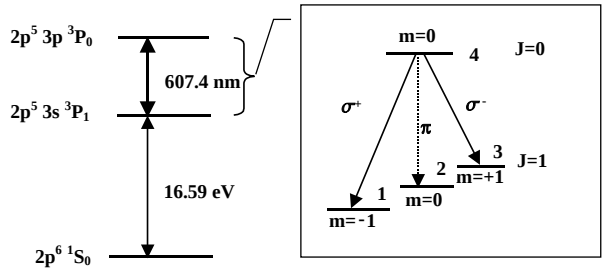

Fig. 6. Energy level diagram of a Ne atom. In the inset selection rules for different polarizations of laser fields are depicted.

within the wavelength range of a typical dye laser; 2) the simple four-level structure allows analytical expressions for CPT parameters be derived, as was shown in the previous section; 3) the lower level has $J = 1$ (with the Lande factor $g = 1.464$) and decays radiatively to the ground state with a decay rate $\sim$ 9 MHz, comparable to that of the upper level. This makes the Zeeman coherence lifetime of the same order as the time required to establish CPT. Therefore, it is important to verify that the technique will work even in such unfavorable conditions.

The experimental setup, used in the present experiment, is illustrated schematically in Fig.7. A single-mode dye laser output at 607.4 nm, tuned to the $2p^5 3s^3P_1 \rightarrow 2p^5 3p^3P_0$ transition of a Ne atom, was split into two beams. The frequency of one beam was shifted by an acousto-optic modulator (AOM) by $\Delta\omega = 110$ MHz. After being recombined beams were propagated along the axis of a discharge tube. A tube with a neon glow discharge (Ne pressure 1.5 Torr, discharge current 40 mA) was placed into an external magnetic field. Its longitudinal component $\mathbf{B_l}$ was produced by a solenoid and the transverse component $\mathbf{B_{tr}}$ by Helmholtz coils. The Zeeman splitting was varied for given laser field frequencies by sweeping the longitudinal component of the magnetic field. The sweeping frequency was tuned in the range $20 - 40$ Hz to minimize low-frequency noise. It is worth noting that discharge parameters were

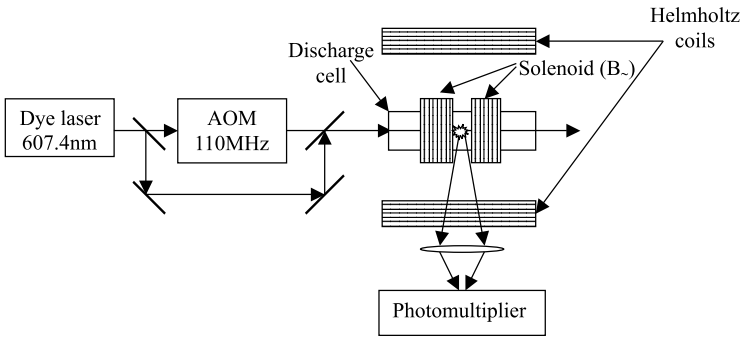

Fig. 7. Experimantal setup.

slightly modulated by the alternating magnetic field. Fluorescence emitted from the discharge in the direction perpendicular to the laser beam propagation direction was separated by a monochromator and detected by a photomultiplier. The laser fields had identical linear polarizations, which could be rotated to be either parallel or perpendicular to $\mathbf{B_{tr}}$. The powers of the laser beams were equal (approximately 2.5 mW in each beam) with a beam spot of $\sim$ 1 mm in diameter, the resulting intensities correspond to the unsaturated CPT regime, so power broadening of resonances is not expected in the experiment.

In the course of the experiment we set $\mathbf{B_{tr}}||\mathbf{ox}$, which corresponds to $\alpha = 0$ in the notations of Fig.5. According to Eq.(2.1) this gives

$$r_x = 4\tan^2\beta = 4\frac{B_{tr}^2}{B_l^2}, \qquad r_y = 0, \tag{2.2}$$

the last result means that no CPT resonance at the single Larmor frequency will be observed if $\mathbf{E_1}, \mathbf{E_2}||\widehat{\mathbf{e}}_\mathbf{y}$, since in this case the magnetic field is perpendicular to the laser beam polarization.

A series of CPT spectra in the presence of a static transverse magnetic field is shown in Fig.8. The magnitude of the transverse field is given in terms of the current

I through the Helmholtz coils. In the case of small B_{tr} ($I \leq 200$ mA) CPT dips are observed only at frequency shifts $\omega_1 - \omega_2 = 0, \pm 2\omega_L$. The resonance at zero shift, which is due to formation of CPT in a degenerate Λ system, is of no interest for us since it carries no information about the magnetic field. As the current is increased, the resonance at the single Larmor frequency $\omega_1 - \omega_2 = \pm\omega_L$ appears.

The position of the CPT dip at the double Larmor frequency for $I = 0$ ($B_{tr} = 0$) gives the total magnetic field magnitude for a fixed laser beams frequency difference:

$$B_{tot} = B_l = \frac{\Delta\omega\hbar}{2g\mu_B}. \tag{2.3}$$

In our case for $\Delta\omega = 110$ MHz the resonance was detected for $B_{tot} = 26.2$ G. As can be seen from Fig.8, it shifts to smaller values of B_l as B_{tr} increases, as expected. Eventually, for currents greater 550 mA the resonance strongly overlaps with the resonance at $B_l = 0$ and is no longer detectable.

As can be seen from Fig.8, the width of the resonance at $\omega_1 - \omega_2 = 2\omega_L$ in the absence of the transverse field ($I = 0$) is $\sim$ 10 G, which corresponds to a spectral width (FWHM) $\sim$ 42 MHz. This means that the Zeeman coherence decay rate in our experiment, given by one-half of this value, is $\sim$ 21 MHz. It is the sum of the radiative decay rate of 9 MHz and the collisional decay rate, which turns out to be 12 MHz, due to collisions with ground-state neon atoms. Although the Zeeman coherence decay rate is two times larger than the radiative decay rate of the upper level, the resonances are still detectable.

In order to test the validity of Eq.(2.2), we calculated B_{tr} from the ratio r_x of intensities of CPT resonances, observed in the experiment. It should be stressed here that, if the frequency shift $\Delta\omega$ is varied for a fixed magnetic field magnitude and orientation, then the use of Eq.(2.2) is straightforward: B_{tot} is determined from the position of the CPT dip at either the double or single Larmor frequency, B_{tr} and B_l

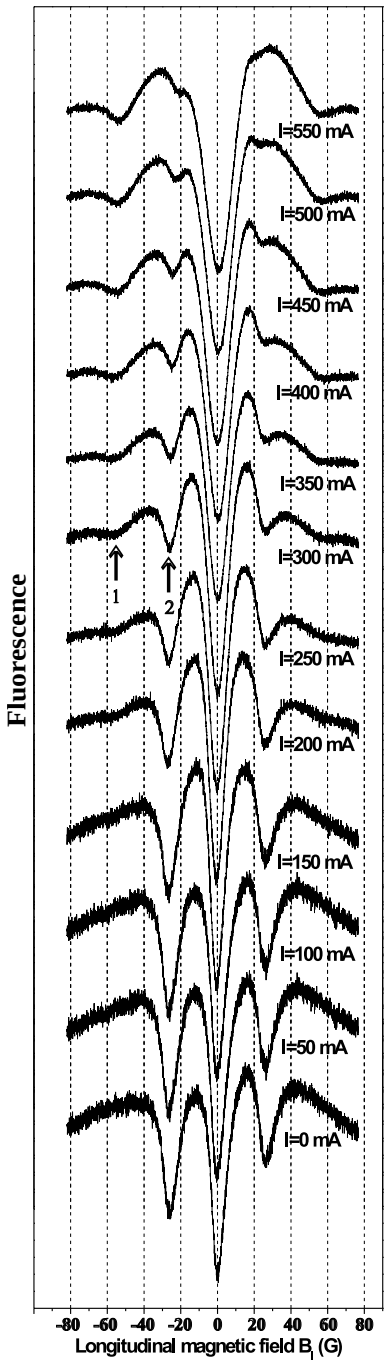

Fig. 8. Experimental fluorescence intensity dependences on the longitudinal component B_l for a number of values of the transverse component B_{tr}, expressed in terms of the current I through the Helmholtz coils; 1 - resonance at $\omega_1 - \omega_2 = \omega_L$; 2 - resonance at $\omega_1 - \omega_2 = 2\omega_L$.

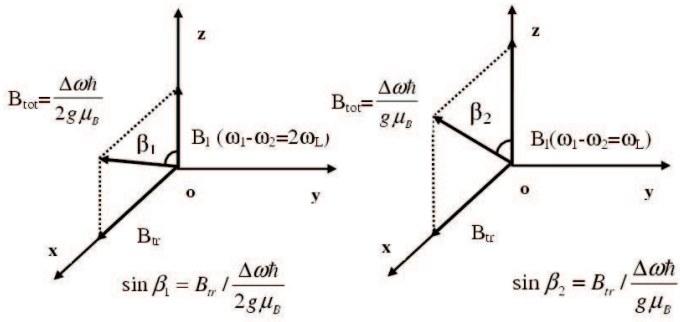

Fig. 9. Difference in magnetic field magnitude and orientation between two types of CPT resonances, observed in experiment.

are calculated from r_x according to the following expressions:

$$B_l = 2B_{tot}\sqrt{\frac{1}{4+r_x}},$$

$$B_{tr} = B_{tot}\sqrt{\frac{r_x}{4+r_x}}.$$

In the experiment B_l was swept for fixed $\Delta\omega$, therefore Eq.(2.2) has to be modified to give the correct values of B_{tr}. As is illustrated in Fig.9, CPT resonances at single and double Larmor frequencies occur for different values of B_{tot} and β. To take this into account we turn to the original expression Eq.(2.1) for r_x, which gives:

$$r_x = \frac{4\cos^2\beta_2\sin^2\beta_2}{\cos^4\beta_1} = \frac{4\left(B_{tr}/\frac{\Delta\omega\hbar}{g\mu_B}\right)^2\left(1-\left(B_{tr}/\frac{\Delta\omega\hbar}{g\mu_B}\right)^2\right)}{\left(1-4\left(B_{tr}/\frac{\Delta\omega\hbar}{g\mu_B}\right)^2\right)}$$

From this expression B_{tr} is derived:

$$B_{tr} = \frac{\Delta\omega\hbar}{g\mu_B}\sqrt{\frac{2r_x+1-\sqrt{3r_x+1}}{2(4r_x+1)}}. \tag{2.4}$$

The spectra in Fig.8 were fitted with several Lorentzians, one Lorentzian for each CPT peak, two Lorentzians for the resonance at $B_l = 0$, and one for a smooth

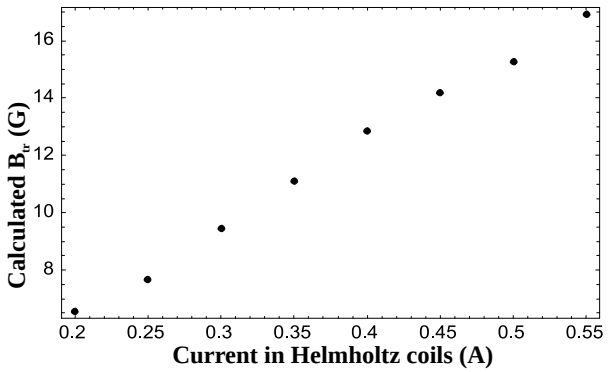

Fig. 10. B_{tr} calculated from experimental CPT spectra according to Eq.(2.4).

background. The amplitudes of the Lorentzians were used as the intensities of the CPT resonances. The resulting dependence of B_{tr}, calculated according to Eq.(2.4), on the current I through the Helmholtz coils is presented in Fig.10. The dependence is linear, as expected; the slope 30.2 G/A of the linear fit to this dependence agrees well with the magnetic constant 31.7 G/A of the Helmholtz coils, obtained from an independent measurement by a magnetometer.

C. Discussion

The magnetic field measurement accuracy in the proposed technique is determined by the spectral resolution of the CPT signal. It is usually very high, depending neither on the Doppler and natural linewidths of the optical transition, nor on the laser linewidth provided the two beams are from the same laser source. In the unsaturated CPT case the spectral resolution is given by the Zeeman coherence decay rate Γ. For a metastable lower level this rate can be of the order of 100 kHz and the corresponding field resolution is hundreds of milligauss; for a radiative lower level (as is the case for the transition studied) the decoherence rate is $1 - 10$ MHz, the corresponding resolution is lower - several gauss. It is worth noting that excited states are strongly

influenced by collisions. Thus the Zeeman coherence decay rate in the limit of unsaturated CPT provides information about collisional rates, if the decoherence collisional mechanisms are known. This method does not have any principal limitations on the strength of the magnetic field; the only difficulty in the case of large fields, leading to large Zeeman splittings, is in phase locking the laser fields if they come from different sources, but currently available optical methods solve this problem [65]. This technique, though, is particularly advantageous for measuring small magnetic fields (up to 1 kG), which are difficult to detect using conventional spectroscopic plasma diagnostics, since they produce a tiny Faraday rotation and Zeeman splittings much smaller than the Doppler width of any optical line.

The technique allows one to study nonstationary processes. The temporal resolution is given by the CPT preparation time. This time, in turn, is proportional to the radiative lifetime of the upper optical level. For a typical electric dipole-allowed transition with oscillator strength $f \sim 1$ the radiative lifetime is $\tau \sim 10 - 100$ ns. The temporal resolution $\sim 10\tau \sim 0.1 - 1$ μs is obtained from the requirement that the CPT has enough time to form.

It is essential also that the time required to establish CPT be smaller than the Zeeman coherence lifetime, otherwise the effect is not observed (it is worth noting that in the experiment the Zeeman coherence decayed faster than the excited state population, but the resonance was still detectable). It imposes a limit on the rates of decoherence processes in the plasma of interest.

There is a requirement that the signal-to-noise ratio suffices to reliably detect CPT resonances. It gives the minimum density of test particles and determines the spatial resolution. Let us analyse it for an experimental situation where the main source of noise is the background plasma emission at the resonant wavelength. During the detection time $\Delta\tau$ the number of resonantly emitted photons is N_r, while

the background plasma produces N_{pl} spontaneous photons. A useful fluorescence signal is reliably detected if its intensity suffuciently exceeds the root-mean-square value of the noise $\sqrt{N_{pl}}$:

$$N_r \geq 3\sqrt{N_{pl}}. \tag{2.5}$$

The number of resonantly emitted photons is proportional to the volume l^3 with l being the required spatial resolution, while N_{pl} originates from the whole plasma volume $l^2 L$ along the collection optics field of view, where L is the characteristic scale of the plasma. The condition Eq.(2.5) can be rewritten in the following form [61]:

$$\sqrt{Al^4 \Omega_{solid} \eta t \Delta\tau / 4\pi L} \frac{\Delta N_{up}}{\sqrt{N_{up}}} \geq 3, \tag{2.6}$$

where A is the radiative decay constant of the upper state, $\Omega_{solid}/4\pi$ is the solid angle observed by the collection optics, η is the quantum efficiency of the photodetector, t is the transmission coefficient of the collection optics, N_{up} is the density of spectroscopic particles excited by the discharge to the upper level, ΔN_{up} is the increase of the upper level population density due to the action of the lasers.

Let us analyse the last two limitations of the method separately for cold and hot plasmas. For cold, partially ionized plasmas, typically found in different types of discharges, this technique is expected to be particularly useful due to the low values of the magnetic field ($\leq 0.2 - 0.3$ T), where application of other diagnostics may be difficult. These discharges are characterized by ion temperatures in the range of $0.025 - 5$ eV, electron temperatures from 1 to 20 eV and ion/electron densities of $10^9 - 10^{12}$ cm^{-3}. In such plasmas neutral atoms might be used as test particles. The Zeeman coherence decays mainly due to neutral-neutral collisions, with a rate $\nu_{neut} = \sigma N_{neut} v_{neut}^T$, where $\sigma \sim 8{\cdot}10^{-15}$ cm^2 is the coherence-destroying collision cross-section for a radiative level [66] (for a metastable level it is typically lower), N_{neut} is

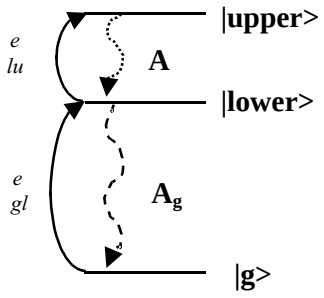

Fig. 11. Illustration of the calculation of population densities of upper and lower states. Here A, A_g are radiative decay constants of the lower and upper levels, ν^e_{gl}, ν^e_{lu} are the excitation rates due to inelastic collisions with electrons.

the density of neutral atoms, and the thermal velocity $v^T_{neut} = \sqrt{3kT/m} \sim 3 \cdot 10^4 - 10^6$ cm/s. The collisional rate will be less than $\tau^{-1} = 10$ MHz for $N_{neut} < 10^{16} - 4 \cdot 10^{17}$ cm^{-3}, which corresponds to pressures of several Torrs.

Let us turn now to the signal-to-noise ratio calculation. In Eq.(2.6) we assume that the upper level population density increase by the lasers action is of the order of the initial density difference of the lower and upper states, $\Delta N_{up} \simeq N_{low} - N_{up}$. The population densities of the upper and lower states are calculated from the requirement of a balance between the excitation processes due to inelastic collisions with electrons, which have a significantly larger temperature in comparison with atoms, and radiative processes. We use the model of a test plasma atom, which includes the ground and two excited states, as depicted in Fig.11, neglecting excitation into higher lying excited states.

The population densities are easily calculated:

$$N_{up} = \nu^e_{lu} N_{low}/A,$$

$$N_{low} = \nu^e_{gl} N_0/A_g,$$

where N_0 is the population density of the ground state. The excitation rates due to inelastic collisions with electrons are [67]

$$\nu^e_{gl} = 3.2 \cdot 10^{-7} f_{gl} \left(\frac{Ry}{E_{low}}\right)^{3/2} e^{-E_{low}/kT_e} \sqrt{E_{low}/kT_e} p(E_{low}/kT_e) N_e,$$

$$\nu^e_{lu} = 3.2 \cdot 10^{-7} f_{lu} \left(\frac{Ry}{\Delta E}\right)^{3/2} e^{-\Delta E/kT_e} \sqrt{\Delta E/kT_e} p(\Delta E/kT_e) N_e. \qquad (2.7)$$

Here $f_{gl,lu}$ is the oscillator strength of the $|g> \rightarrow |lower>$, $|lower> \rightarrow |upper>$ transition, E_{low} is the energy of the lower state, ΔE is the energy difference of the lower and upper states, kT_e is the electron temperature in eV, $Ry = 13.6$ eV, and N_e is the electron density in cm^{-3}. We take the values $kT_e = 10$ eV and $N_e = 10^{10}$ cm^{-3}, typical for a cold plasma, the typical energies $E_{low} \sim 15$ eV, and $\Delta E \sim 2 - 5$ eV, and the radiative decay constants $A,\ A_g \sim 10^7 - 10^8$ s^{-1}, typical for an electric dipole-allowed transition ($f_{gl,lu} \sim 1$). The p function is equal to 0.1 for the $|g> \rightarrow |lower>$ and 0.3 for $|lower> \rightarrow |upper>$ transitions. This gives excitation rates $\nu^e_{gl} \approx 100$ s^{-1}, $\nu^e_{lu} \approx (2-6) \cdot 10^3$ s^{-1}. We then have

$$\frac{\Delta N_{up}}{\sqrt{N_{up}}} \sim \frac{N_{low} - N_{up}}{\sqrt{N_{up}}} = \sqrt{N_0} \sqrt{\frac{\nu^e_{gl}/A_g}{\nu^e_{lu}/A}} (1 - \nu^e_{lu}/A) \sim$$

$$\sim \sqrt{N_0} \sqrt{\frac{\nu^e_{gl}}{\nu^e_{lu}}} \approx (0.1 - 0.2)\sqrt{N_0}.$$

This allows us to estimate the minimum density of test particles required by the need for an adequate signal-to-noise ratio. Plugging into Eq.(2.6) the typical parameters of a collection system ($\Omega_{solid}/4\pi \sim 10^{-2}$, $\eta \sim 10^{-2}$, $t = 0.5$), the characteristic plasma scale $L = 1$ m, and spatial and temporal resolution $l \sim 1$ cm and $\Delta\tau \sim 1$ μs, we get $N_0 \geq 10^7 - 10^8$ cm^{-3}. The range of parameters of a cold plasma at which the technique is applicable, calculated according to the model we used above, is depicted in Fig.12.

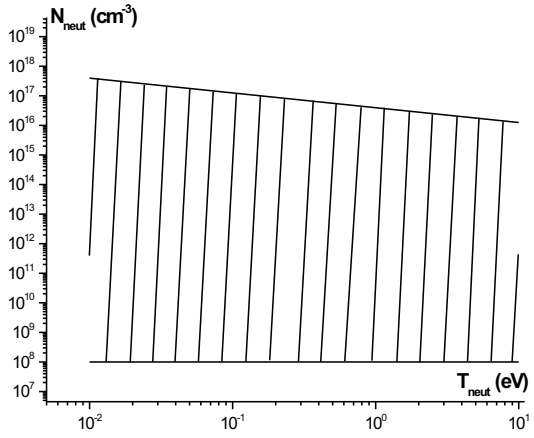

Fig. 12. The approximate range of cold plasma parameters, where the method works.

In hot, fully ionized plasmas, ions might be used as test particles. If the temperature of a plasma is very high, the main source of Zeeman decoherence is the particle flight out of the laser beam, and it sets a limit on the thermal velocity of the atoms/ions. Namely, the time-of-flight of a spectroscopic particle through the laser beam has to exceed the CPT preparation time: $\tau < l/v^T$, where l is the laser beam diameter, v^T is the thermal velocity. For $l = 1$ cm and $\tau = 10$ ns the maximum velocity is $v^T < 10^6$ m/s, or, equivalently, the maximum temperature $T < 10$ keV (here and in the rest of the text the mass $m \sim 10m_p$ is used in estimates). The main coherence dephasing mechanism at smaller temperatures is ion-ion and ion-electron collisions. For an estimate, we use integrated ion-ion and ion-electron elastic collision rates [68]:

$$\nu_{ii} = \frac{16\pi e^4 Z^4 N_i L_i}{(3kT_i)^{3/2} m_i^{1/2}}, \tag{2.8}$$

$$\nu_{ei} = \frac{4\pi e^4 Z^2 N_e L_e}{(3kT_e)^{3/2} m_e^{1/2}}. \tag{2.9}$$

Here N_i, N_e are the ion and electron densities; m_i and m_e are their masses, Z is the ion

charge number, $L_i = 23 + 3/2 ln T_{i,e} - 1/2 ln N_i$, $L_e = 24 + ln T_e - 1/2 ln N_e$ for $T_e > 10$ eV - Coulomb logarithms ($T_{i,e} = \min(T_i, T_e)$, T_i, T_e are in eV, N_i, N_e are in cm^{-3}). The rate of inelastic collisions with electrons can be estimated using Eq.(2.7). For an estimate we take $L_i = L_e = 10$, $T_i = T_e = 10 - 10^4$ eV, and $Z = 1$. The condition $\nu_{ii}, \nu_{ei}, \nu^e_{lu} < 10\ MHz$ is satisfied for ion and electron densities $N_i, N_e < 10^{14} - 10^{15}$ cm^{-3}. The higher the electron/ion temperature, the higher are the ion and electron densities allowed as is clear from Eqs.(2.7)-(2.9).

Let us now estimate from Eq.(2.6) the minimum ion density reqiured to discriminate a signal against noise. Supposing a thermalized plasma, we have $\Delta N_{up} \simeq N_{low} - N_{up} = N_0 \exp(-E_{low}/kT)(1 - \exp(-\Delta E/kT))$. The condition Eq.(2.6) assumes the form:

$$\sqrt{Al^4 \Omega_{solid} \eta t \Delta\tau N_0 / \pi L} \exp(-E_{low}/2kT) \sinh(\Delta E/2kT) \geq 3.$$

Let us estimate the detection limit for the case of high temperature, which is obviously the worst from the signal-to-noise point of view due to the almost equal population of levels by the discharge. For the same parameters of the collection system, plasma scale, spatial and temperature resolution, for a dipole-allowed optical transition with $\Delta E = 2 - 5$ eV, and taking the electron/ion temperature $T = 10 - 10^4$ eV, the detection limit is $N_0 \geq 10^5 - 10^{10}$ cm^{-3}. This reasoning is summarized in Fig.13.

D. Conclusion

A local magnetic field diagnostic based on the coherent population trapping effect is developed. The diagnostic is an extension of the laser induced fluorescence technique, providing sub-Doppler and sub-natural spectral resolution by the use of a two-photon Raman transition. The high spectral resolution of the CPT signal, determined by the

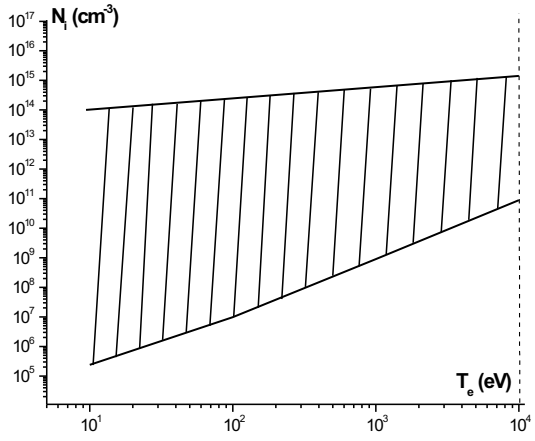

Fig. 13. The range of hot plasma parameters, where the diagnostic is applicable. $T_i = T_e$ was assumed.

Zeeman sublevel coherence decay rate, leads to a high magnetic field measurement accuracy, nicely combined with good temporal and spatial resolution. The technique is able to measure both the strength and the orientation of the field.

A demonstration experiment was carried out in a plasma produced in a low-pressure neon glow discharge. It was shown that from the position of a CPT resonance in the fluorescence spectrum the strength of the local magnetic field can be obtained. By utilizing the dependence of the dipole moments of optical transitions from different Zeeman sublevels of a lower level to a common upper level on magnetic field orientation and laser field polarizations, it was demonstrated that the direction of the field can be determined from the ratio of the fluorescence intensities of the two types of CPT resonances. We made theoretical estimates of the range of temperatures and densities for cold and hot plasmas, where the technique can be applied. The estimates show that the technique is applicable to a variety of plasma configurations. It might be particularly useful in magnetic confinement devices with low magnetic

fields, where application of other diagnostics may be difficult.

CHAPTER III

ATOMIC INTERFERENCE AND COHERENCE PHENOMENA IN SOLIDS WITH A LONG-LIVED SPIN COHERENCE

Most of the theoretical and experimental work on EIT and CPT so far (with the exception of a few experiments [69]-[79]) has delt with gaseous media. Motivated by practical considerations to implement them in real devices one turns to solid materials. Indeed, the obvious advantages of solids are high density of atoms, compactness, absence of atomic diffusion (which is especially important for optical memory), and simplicity and convenience in preparation and usage. On the other hand, the commonly known difficulties with realization of atomic interference effects in solids are typically very broad optical lines and fast decay of any coherence.

At the moment a few proof-of principle EIT experiments have been fulfilled in three different types of solid materials: in transition metal [69] and rare-earth ion doped crystals with forbidden transitions lying in the band gap of a crystal [71]-[74], in nitrogen vacancy centers in diamond [75, 76] and in semiconductors [77] on inter-sub-band transitions in quantum wells, including EIT due to tunneling into the same energy continuum [78], and in an exciton-biexciton system [79]. Transparency of the order of 100% was achieved in some of them [71, 76, 77, 78]. However, this required much higher intensities than in gaseous media and resulted in larger EIT linewidths. The obvious difficulty of dealing with semiconductors is the very fast decay (subpicosecond time) of electronic coherence. On the other hand, the spin coherence decay time in EIT experiments with defect levels in crystals [71, 76] is of the same order of magnitude (tens or hundreds of μs) as in experiments with gases [80]. Rare-earth and transition metal ion activated crystals having discrete energy levels lying in the band gap of the crystal are a solid-state analog of atomic gases,

since they offer narrow electronic transitions. The combination of narrow optical transitions with a long-lived spin coherence makes them promising for realization of the described above interference and coherence phenomena.

Several questions arise. (i) What is the threshold for the driving field providing EIT in solid materials? (ii) What is the EIT linewidth dependence on the intensity of the driving field and other parameters of the system? (iii) What determines the efficiency of nonlinear transformations and quantum light storage in solids? In order to answer these questions, to explain the recent experimental data [71, 76], and to identify the optimal regimes and the most suitable materials for realization of EIT, we here generalize the theory of EIT for the case of solids with a long-lived coherence [64]. We take into account the major specifics of these materials as compared to gaseous media, namely, homogeneous and inhomegeneous line broadening of both optical and spin transitions as well as the difference between the longitudinal T_1=spin-lattice and transverse T_2=spin-spin relaxation times in a low-frequency transition. In gases T_1 and T_2 are typically indistiguishable, being defined by the lifetime of the atoms in the light beam.

A. Susceptibility of a Λ system

Let us consider the energy scheme depicted in Fig.14. In this three-level Λ scheme one of the two lower-levels (c) is coupled to the upper level (a) by a coherent driving laser and the transition $a \rightarrow b$ is probed by a weak coherent field. The atomic decays as indicated ensure that each atom will come to a steady state condition.

In the present analysis we use the following assumptions: 1) The decay rates of the transitions $a \rightarrow b$ (γ) and $a \rightarrow c$ (γ') are assumed to be the same (γ); 2) the probe field is weak so that a first order analysis is valid; 3) the strong driving field is

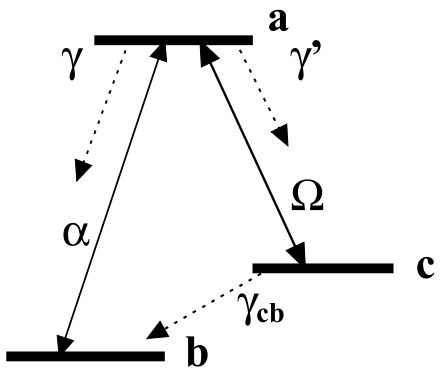

Fig. 14. Λ-scheme under consideration.

on resonance with the $a \rightarrow c$ transition.

The semiclassical Hamiltonian describing the atom-field interaction for the system under consideration can be written in the rotating wave approximation as

$$V = -\hbar\alpha e^{-i\nu t}|a><b| - \hbar\Omega e^{-\nu_0 t}|a><c| + H.c., \tag{3.1}$$

where $\Omega = \mu_{ac}E_d/2\hbar$ is the Rabi-frequency of the driving field; the Rabi frequency of the probe field is defined by $\alpha = \mu_{ab}E_p/2\hbar$; μ_{ab}, μ_{ac} are the matrix elements of the dipole moment between levels a and b, a and c, respectively; and ν and ν_0 are the frequencies of the probe and driving fields. The equations of motion for the density matrix elements are

$$\dot{\rho}_{ab} = -\Gamma_{ab}\rho_{ab} - i\alpha(\rho_{aa} - \rho_{bb}) + i\Omega\rho_{cb}, \tag{3.2}$$

$$\dot{\rho}_{cb} = -\Gamma_{cb}\rho_{cb} - i\alpha\rho_{ca} + i\Omega\rho_{ab}, \tag{3.3}$$

$$\dot{\rho}_{ac} = -\Gamma_{ac}\rho_{ac} - i\alpha\rho_{bc} - i\Omega(\rho_{aa} - \rho_{cc}), \tag{3.4}$$

$$\dot{\rho}_{cc} = -w_{cb}\rho_{cc} + w_{ac}\rho_{aa} + w_{cb}\rho_{bb} - i\Omega(\rho_{ca} - \rho_{ac}), \tag{3.5}$$

$$\dot{\rho}_{aa} = -(w_{ab} + w_{ac})\rho_{aa} - i\alpha(\rho_{ab} - \rho_{ba}) - i\Omega(\rho_{ac} - \rho_{ca}), \tag{3.6}$$

$$\rho_{aa} + \rho_{bb} + \rho_{cc} = 1. \tag{3.7}$$

Here the Rabi frequencies were assumed real, Γ_{ij} are defined as $\gamma_{ij} + i\Delta_{ij}$, w_{ij} are the population relaxation rates, $w_{cb} = w_{bc}$ so that before the action of the driving field the levels b and c are equally populated (which is typical for spin transitions in solids even at very low temperatures), and $\gamma_{ab} = \gamma_{ac} = \gamma$. The Δ_{ij}'s are given by $\Delta_{ab} = \omega_{ab} - \nu = \Delta + \Delta\omega_{ab}$, $\Delta_{ac} = \omega_{ac} - \nu_0 = \Delta_0 + \Delta\omega_{ac}$, $\Delta_{cb} = \omega_{cb} - \nu + \nu_0 = \Delta - \Delta_0 + \Delta\omega_{cb}$, and $\Delta\omega_{ac} = \Delta\omega_{ab} - \Delta\omega_{cb}$. Here ω_{ab}, ω_{ac} and ω_{cb} are the frequencies of the corresponding transitions, $\Delta\omega_{ab}$ and $\Delta\omega_{cb}$ are the deviations of the atomic frequencies of the $a \rightarrow b$ and $c \rightarrow b$ transitions from the corresponding inhomogeneous line centers, and Δ and Δ_0 are the detunings of the probe and the driving fields from the line centers.

In the absence of the probe field the steady state solutions for the populations are obtained from Eqs.(3.2)-(3.7) as

$$\rho_{aa}^{(0)} = \frac{2w_{cb}\Omega^2}{2D}, \tag{3.8}$$

$$\rho_{bb}^{(0)} = \frac{4\gamma X w_{cb} + 2w_{cb}\Omega^2 + 2\gamma\Omega^2}{2D}, \tag{3.9}$$

$$\rho_{cc}^{(0)} = \frac{4\gamma X w_{cb} + 2w_{cb}\Omega^2}{2D}, \tag{3.10}$$

where

$$X = \frac{\gamma^2 + \Delta_{ac}^2}{2\gamma}, D = 4\gamma X w_{cb} + \gamma\Omega^2(1 + \frac{3w_{cb}}{w_{ac}}).$$

In terms of these populations ρ_{ab}, governing the linear susceptibility of the medium at the probe field wavelength, can be found to first order in the probe field as

$$\rho_{ab} = \frac{-i\alpha}{\Gamma_{ab}\Gamma_{cb} + \Omega^2}\left[\Gamma_{cb}(\rho_{aa}^{(0)} - \rho_{bb}^{(0)}) + \frac{\Omega^2}{\Gamma_{ca}}(\rho_{cc}^{(0)} - \rho_{aa}^{(0)})\right]. \tag{3.11}$$

Let us assume that the driving field is resonant, such that $\Delta_0 = 0$. Then ρ_{ab} can be

written as

$$\rho_{ab} = \frac{-i\alpha}{Y}\frac{1}{2D}\left[-(\gamma_{cb} + i\Delta_{cb})(4X\gamma w_{cb} + 2\Omega^2\gamma) + \frac{\Omega^2}{\gamma - i\Delta\omega_{ac}} 4\gamma X w_{cb}\right], \qquad (3.12)$$

where

$$Y = (\gamma + i\Delta + i\Delta\omega_{ab})(\gamma_{cb} + i\Delta_{cb}) + \Omega^2.$$

In an inhomogeneously broadened solid system, the susceptibility should be averaged over the entire range of the frequencies of the corresponding transition, which is determined by the inhomogeneity of the crystaline fields in solids. Similarly, in EIT experiments in gases the inhomogeneous Doppler broadening at the optical transitions should be taken into account [81]. Inhomogeneous broadening at the low-frequency (hyperfine or Zeeman) transition, caused in the case of co-propagating fields by the residual Doppler effect $(k_2 - k_1)v$, can be neglected as compared to the homogeneous width of the transition determined by the time-of-flight of an atom through a laser beam, because $\omega_{cb} << \omega_{ab},\ \omega_{ac}$. However, in EIT experiments in solids (as well as in gases with large ω_{cb} [17]) inhomogeneous broadening at both one-photon and two-photon transitions play an important role. Averaging of the susceptibility over inhomogeneous profiles is described in the Appendix.

B. EIT-linewidth

In order to estimate the linewidth of the EIT resonance we evaluate the imaginary part of the susceptibility, which is the sum of three terms $\chi^{''} = \chi^{''}_{11} + \chi^{''}_{12} + \chi^{''}_{21}$, calculated in the Appendix.

The susceptibility strongly depends on two parameters:

$$x = \frac{\Omega^2\gamma}{2w_{cb}(W^{ab})^2},$$

$$z = \frac{\gamma W^{cb}}{w_{cb} W^{ab}}, \tag{3.13}$$

where $2W^{ab(cb)}$ is the width of the inhomogeneously broadened optical (low-frequency) transition. The parameter x can be presented in the form: $x = \Omega^2/\Omega_{inh}^2$, where $\Omega_{inh}^2 = 2w_{cb}(W^{ab})^2/\gamma$ gives the characteristic value of the driving field intensity ($I_{inh} \sim \Omega_{inh}^2$) providing optical pumping for all atoms within an inhomogeneously broadened optical line. Hence the parameter x defines the degree of optical pumping of atoms into the ground state. The parameter z is defined by the ratio of the relative broadenings at the low-frequency and optical transitions.

In a gaseous medium in the Λ scheme with co-propagating fields, where inhomogeneous broadening at the low-frequency transition (defined by the residual Doppler effect, $(k_2 - k_1)v$) is negligible (and hence W^{cb} should be replaced by w_{cb}) this parameter takes the form: $z = \gamma/W^{ab}$, i.e., it does not exceed 1. In a Bose-Einstein condensate $z = 1$. In a solid medium it may be either less than or greater than 1, depending on the magnitude of the inhomogenous broadening at the low-frequency transition characterizing the dephasing between spins of different ions.

Usually the inhomogenous broadening at a spin transition is orders of magnitude smaller than at an optical transition. Hence the term $\chi_{12}^{''}$, which is W^{cb}/W^{ab} times smaller than $\chi_{11}^{''}$, can be neglected.

Typical shapes of $\chi_{11}^{''}$ and $\chi_{21}^{''}$ for different regimes of EIT are shown in Figs.15-19.

In order to estimate the linewidth of the EIT resonance we first find that the maximum of $\chi'' = \chi_{11}'' + \chi_{21}''$ is $\chi_{\max}'' \approx \eta/W^{ab}$ at $\Delta \approx \pm\Omega$. As the next step we calculate the minimum absorption at zero detuning of the probe field, which is given by the expression

$$\chi''(\Delta = 0) = \frac{\eta}{W^{ab}} \frac{x + z/2 + z\sqrt{x}/2}{(1 + \sqrt{x})(x + z/2)(1 + 2\sqrt{x}/z)}. \tag{3.14}$$

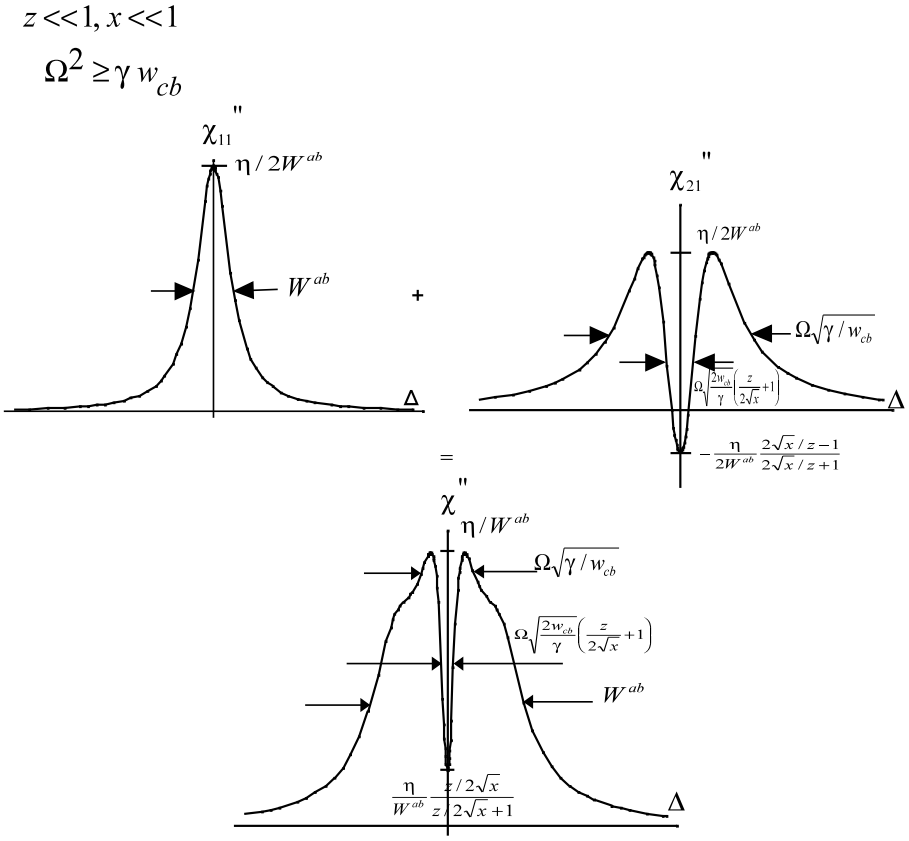

Fig. 15. A numerical calculation of susceptibility components under conditions $z << 1$, $x << 1$, $\Omega^2 \geq \gamma w_{cb}$. An antihole forms in $\chi_{21}^{''}$ and is clearly seen in the resulting $\chi^{''}$ profile.

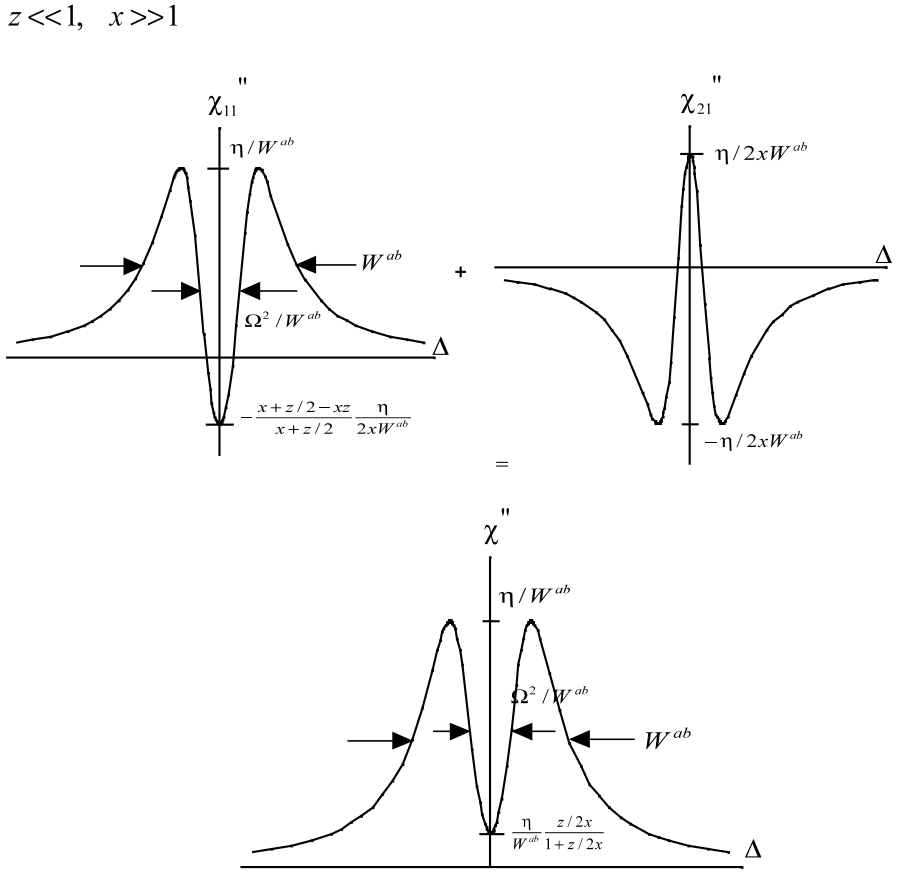

Fig. 16. Susceptibility components under conditions $z << 1$, $x >> 1$. EIT resonance is power-broadened.

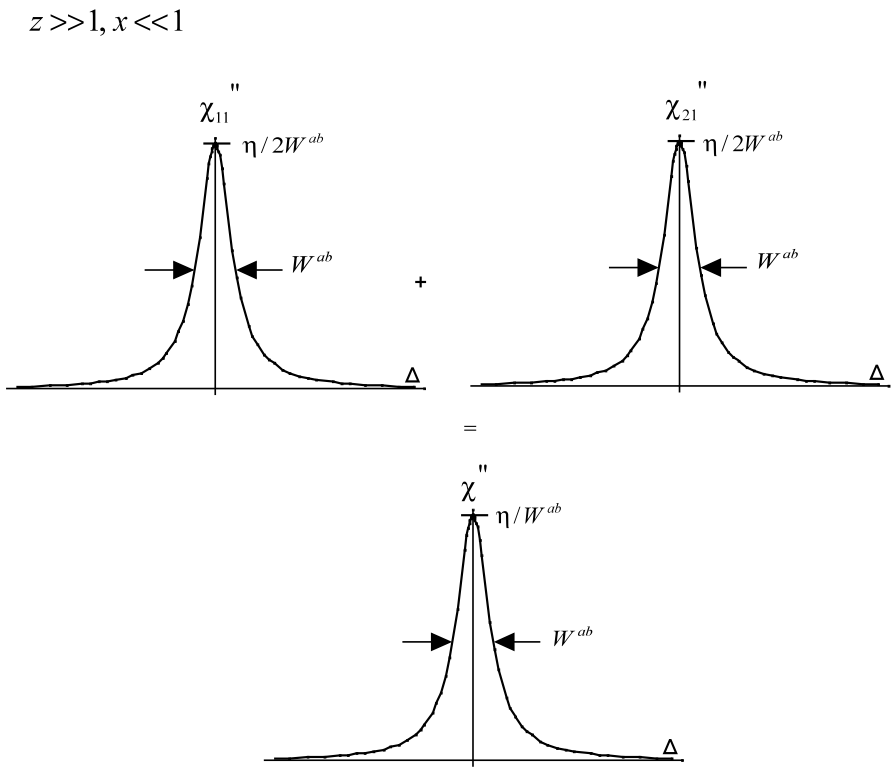

Fig. 17. Susceptibility components in the case $z >> 1$, $x << 1$. There is no EIT in this regime.

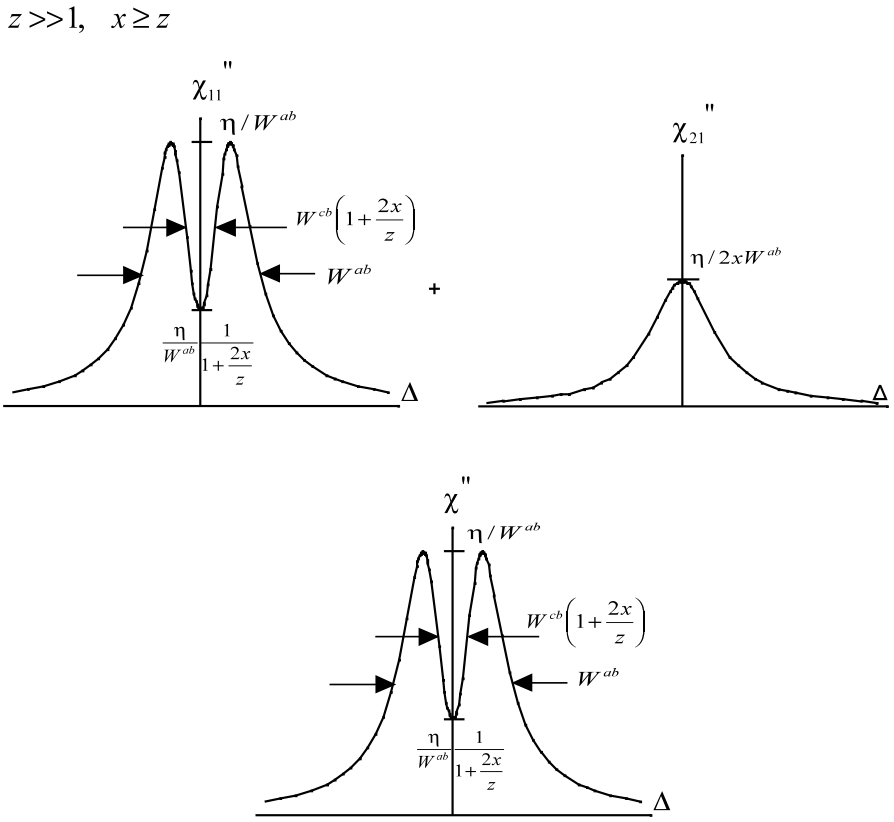

Fig. 18. Susceptibility in the case $z >> 1$, $x \geq z$. EIT sets in when the driving laser intensity exceeds a threshold value ($\Omega^2 > W^{ab}W^{cb}$), EIT resonance is power-broadened.

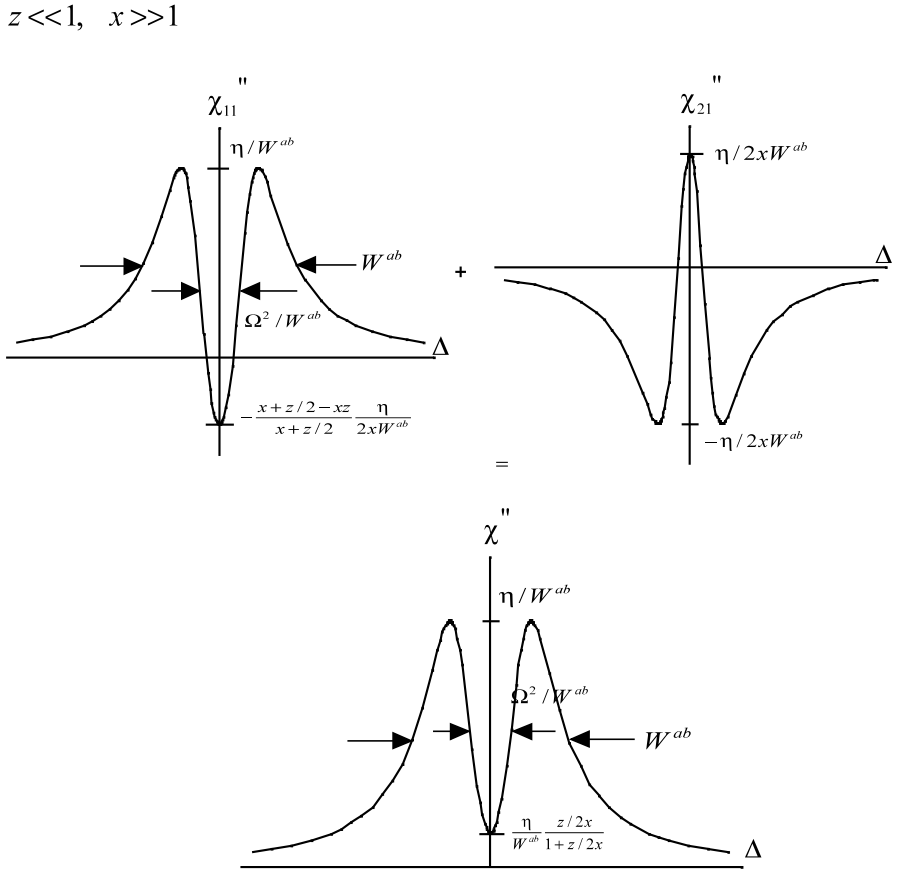

Fig. 19. A numerical calculation of susceptibility under conditions $z >> 1$, $x >> z$. EIT amplitude is 100%, the resonance is power-broadened.

Let us define Γ_{EIT} as $\chi''(\Delta = \Gamma_{EIT}) = (\chi''_{\max} + \chi''(\Delta = 0))/2$. Then the width of the EIT resonance is obtained as

$$\Gamma^2_{EIT} = \frac{2\sqrt{x}}{z}(W^{cb})^2 \frac{(1 + x\sqrt{x} + 2x(1+x)/z)\,(1 + \sqrt{x}/z + x/z)}{x + \sqrt{x} + 1 + 2x(1+\sqrt{x})/z} \times$$

$$\times \left[1 + \left\{1 + \frac{z^2}{4x} \frac{(1+2x/z)^2\,(1+2\sqrt{x}/z)^2\,(x+\sqrt{x}+1+2x(1+\sqrt{x})/z)^2}{(1+x\sqrt{x}+2x(1+x)/z)^2\,(1+\sqrt{x}/z+x/z)^2}\right\}^{1/2}\right]. \tag{3.15}$$

Let us define also the transmission coefficient T as

$$T = exp\left[-\frac{2\pi k L \eta}{W^{ab}} \frac{1 + \sqrt{x} + \frac{2x}{z}}{(1+\sqrt{x})(1+\frac{2x}{z})(1+\frac{2\sqrt{x}}{z})}\right], \tag{3.16}$$

where $k = \nu c$ is the wave number of the probe field, L is the length of the medium, and $\eta = N\mu^2_{ab}/2\hbar$.

The threshold intensity of the driving field providing EIT and the dependence of the EIT linewidth broadening and the transmission coefficient on the intensity are essentially determined by the parameter z. Let us analyze two extreme limits: $z << 1$ and $z >> 1$.

1) $z << 1$.

This limit might be realized in solids with a relatively small inhomogeneous width W^{cb} of the low-frequency transition.

For low intensities of the driving laser ($x << 1$) the second term χ''_{21} gives an antihole (see Fig.15), formed due to absorption by the atoms resonantly pumped from the state c to the ground state b. The width of the antihole is defined by the magnitude of the maximal detuning for which atoms are optically pumped for a given intensity: $\Delta_{ant} = \Omega\sqrt{\gamma/w_{cb}}$. This antihole is imposed on a broad background with the width W^{ab} representing the absorption of off-resonant atoms, which is described by the term χ''_{11}.

The line center absorption in this limit is $\chi''(\Delta = 0) \approx \eta/(W^{ab}(1 + 2\sqrt{x}/z))$, so EIT becomes observable as $\sqrt{x}/z \sim 1$ or $\Omega^2 \sim \gamma(W^{cb})^2/w_{cb}$. As long as this condition is satisfied, $\chi''(\Delta = 0)$ is vanishingly small as $\eta z/2W^{ab}\sqrt{x}$ when $x << 1$ and as $\eta z/2W^{ab}x$ when $x >> 1$.

The linewidth for low driving laser intensity, when some of the atoms (with detunings within the antihole width) is optically pumped into the state b, i.e., $x << 1$, is

$$\Gamma_{EIT}^2 = \frac{2\sqrt{x}}{z}(W^{cb})^2\left(1 + \sqrt{x}/z\right)\left[1 + \left\{1 + \frac{(1 + z/2\sqrt{x})^2}{(1 + \sqrt{x}/z)^2}\right\}^{1/2}\right].$$

As EIT sets in with $\sqrt{x}/z \sim 1$, the linewidth is $\Gamma_{EIT} \sim W^{cb}$. Note that, generally speaking, the threshold intensity ($\Omega^2 \sim \gamma(W^{cb})^2/w_{cb}$) is larger than in a homogeneously broadened medium ($\Omega^2 \sim \gamma\gamma_{cb}$) by a factor $(W^{cb})^2/\gamma_{cb}w_{cb} > 1$. For higher intensities, when $\sqrt{x}/z >> 1$ but still $x << 1$, we easily obtain

$$\Gamma_{EIT} \Longrightarrow \Omega\sqrt{\frac{2w_{cb}}{\gamma}}. \tag{3.17}$$

According to Eq.(3.17) the linewidth of EIT is linearly proportional to Ω, the Rabi frequency of the driving field (i.e. the square root of the intensity) and is independent of the inhomogeneous width W^{ab}. For very high intensities of the driving laser ($x >> 1$) when all atoms are optically pumped into the state b the general formula (8a) takes the form of the traditional power broadening law:

$$\Gamma_{EIT} \Longrightarrow \frac{\Omega^2}{W^{ab}}. \tag{3.18}$$

In Fig.20 the EIT linewidth and transmission coefficient dependence on the characteristic combination of parameters $2\sqrt{x}/z = \Omega\sqrt{2w_{cb}/\gamma(W^{cb})^2}$ in the case $z << 1$ is highlighted. The logarithmic plot shows that at low intensity of the drive laser ($2\sqrt{x}/z < 1$) the width is constant, but at higher ($2\sqrt{x}/z > 1$) it changes along a

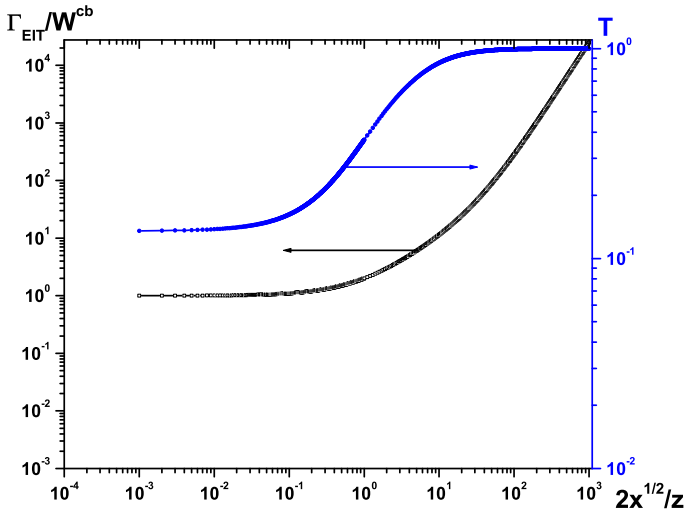

Fig. 20. Logarithmic plot illustrating EIT linewidth and transmission dependence on the characteristic parameter $2\sqrt{x}/z$ in the case $z << 1$.

line with slope 1, and at even higher intensity ($2\sqrt{x}/z \sim 10^2$) the slope changes to 2.

It is worth noting that with the introduction of an effective width δ_{eff} defined as the magnitude of the maximum detuning for which atoms are optically pumped into the ground state b, the EIT linewidth can always be presented in the form $\Gamma_{EIT} = \Omega^2/\delta_{eff}$, which is similar to the EIT linewidth in a homogeneously broadened medium, where $\Gamma_{EIT} = \Omega^2/\gamma$.

The physical reason for a linear dependence of the EIT linewidth on Ω in the case $x << 1$ is that δ_{eff} (which is defined in this range of intensities by the width of the antihole) is proportional to Ω, i.e., more and more far-detuned atoms become optically pumped into the ground state as Ω increases. On the other hand, at very high intensity ($x >> 1$), when all atoms are optically pumped and hence δ_{eff} does not increase any more after reaching its maximum value at $x = 1$, W^{ab}, the EIT linewidth broadens proportionally to the intensity.

A similar linear dependence of the width of some sub-Doppler resonances on Ω (see Eq.(3.17)) was obtained in earlier work by Feld and Javan in three-level laser gain systems [82]. In the situation under study in [82] the relaxation rates at the one-photon and two-photon transitions were of the same order, so that the resonance width was fully determined by the Rabi frequency in the whole range of intensities. A linear dependence of the EIT linewidth on the drive field Rabi frequency was found in [81], where inhomogeneous broadening at the two-photon transition was ignored, and also in [83] (though in a different regime corresponding to trapping of all atoms ($\gamma_{bc} = 0$) and a relatively strong signal field contributing to the line broadening).

Note that at an arbitrary fixed value of intensity and given homogeneous broadening the EIT linewidth in an inhomogeously broadened medium ($\Gamma_{EIT} = \Omega^2/\delta_{eff}$) is essentially narrower than in a homogeneously broadened medium ($\Gamma_{EIT} = \Omega^2/\gamma$). The physical reason for this EIT line-narrowing effect is that power-broadening of the line is weaker for off-resonant atoms. This line-narrowing effect is similar to that discussed earlier by Feld and Javan [82]. At the same time the EIT linewidth can never be reduced beyond its ultimate limit defined by W^{cb}.

2)$z >> 1$.

Here no EIT is observed until $x \sim z$, when $\chi''(\Delta = 0) \approx \eta/(W^{ab}(1 + 2x/z))$; for $x >> z$ absorption at the line center is small as $\eta z/2W^{ab}x$.

The corresponding linewidth for low intensity is

$$\Gamma_{EIT}^2 = \frac{2x}{z}(W^{cb})^2\,(1 + x/z)\left[1 + \left\{1 + \frac{(1 + z/2x)^2}{(1 + x/z)^2}\right\}^{1/2}\right],$$

so again EIT starts with $\Gamma_{EIT} \sim W^{cb}$, but in this case with much higher intensity $\Omega^2 \sim W^{ab}W^{cb}$ ($x \sim z$). For higher intensities ($x >> z$)

$$\Gamma_{EIT} \Longrightarrow \frac{\Omega^2}{W^{ab}}.$$

For media with a large inhomogeneous width of the $c \rightarrow b$ transition, characterized by the condition $z >> 1$, we see that a considerably higher (by the factor $W^{ab}W^{cb}/\gamma\gamma_{cb}$) intensity is required for EIT to be observed than in a homogeneously broadened medium, and there is no linear dependence on the Rabi frequency of the driving field as we found in the limit $z << 1$. From the very begining, when the intensity of the driving laser exceeds the threshold intensity ($\Omega^2 \sim W^{ab}W^{cb}$) the linewidth is power-broadened.

C. Group velocity in an inhomogeneously broadened EIT medium

The dispersive properties of an electromegnetically induced transparent medium are as interesting as its absorption characteristics. It has been demonstrated both theoretically and experimentally [24] that EIT is accompanied by steep frequency dispersion (large derivative $dn/d\nu$) near the line center, which leads to a time delay of the probe pulse and reduction in its group velocity. As is well known the group velocity of light in a medium is given by

$$V_g = \frac{c}{n + \nu dn/d\nu},$$

where $n \simeq n_0 + 2\pi\chi'$.

Under the experimental conditions of Refs.[24],[69]-[76] the refractive index $n_0 \sim 1 - 2$ and in the EIT regime we can neglect n_0 in comparison with $\nu dn/d\nu$, so that $V_g = c/(2\pi\nu d\chi'/d\nu)$.

The time delay for a pulse in a sample of length L is then

$$T_D = L(1/V_g - 1/c) = \frac{2\pi\nu L}{c}\frac{\partial\chi'}{\partial\nu}.$$

For the inhomogeneously broadened system considered in section B the steepness of

the dispersion function is given by the expression:

$$\left.\frac{\partial\chi'}{\partial\nu}\right|_{\nu=\omega_{ab}} = \frac{\eta}{W^{ab}W^{cb}}\frac{2\sqrt{x}/z}{1+\sqrt{x}}\frac{1+\sqrt{x}+x+4x(1+\sqrt{x})/z+4x^2/z^2}{(1+2\sqrt{x}/z)^2(1+2x/z)^2}.$$

Let us again consider limits $z << 1$ and $z >> 1$.

1) $z << 1$

For low driving field intensities ($x << 1$) EIT becomes observable when $\sqrt{x} \sim z$, and

$$\left.\frac{\partial\chi'}{\partial\nu}\right|_{\nu=\omega_{ab}} \approx \frac{\eta}{W^{ab}}\frac{2\sqrt{x}/z}{W^{cb}} = \frac{\eta}{W^{ab}}\frac{2\sqrt{x}}{z}\frac{1}{\Gamma_{EIT}}.$$

When $x << 1$ and $\sqrt{x} >> z$

$$\left.\frac{\partial\chi'}{\partial\nu}\right|_{\nu=\omega_{ab}} \approx \frac{\eta}{W^{ab}}\frac{1}{\Omega\sqrt{2w_{cb}/\gamma}} = \frac{\eta}{W^{ab}}\frac{1}{\Gamma_{EIT}}.$$

For high driving laser intensities corresponding to $x >> 1$ the steepness is

$$\left.\frac{\partial\chi'}{\partial\nu}\right|_{\nu=\omega_{ab}} \approx \frac{\eta}{\Omega^2} = \frac{\eta}{W^{ab}}\frac{W^{ab}}{\Omega^2} = \frac{\eta}{W^{ab}}\frac{1}{\Gamma_{EIT}}.$$

2) $z >> 1$

In this limit EIT becomes observable when $x \sim z$. At this time

$$\left.\frac{\partial\chi'}{\partial\nu}\right|_{\nu=\omega_{ab}} \approx \frac{\eta}{W^{ab}}\frac{2x/z}{(1+2x/z)^2}\frac{1}{W^{cb}} = \frac{\eta}{W^{ab}}\frac{2x/z}{(1+2x/z)^2}\frac{1}{\Gamma_{EIT}}.$$

For $x >> z$

$$\left.\frac{\partial\chi'}{\partial\nu}\right|_{\nu=\omega_{ab}} \approx \frac{\eta}{\Omega^2} = \frac{\eta}{W^{ab}}\frac{W^{ab}}{\Omega^2} = \frac{\eta}{W^{ab}}\frac{1}{\Gamma_{EIT}}.$$

As we can see, in general case under EIT conditions the group velocity and accordingly the time delay of the pulse are defined as:

$$V_g/c = \frac{1}{\pi\omega}\frac{\hbar\Gamma_{EIT}W^{ab}}{N\mu_{ab}^2}, \tag{3.19}$$

$$T_D = \frac{\pi\omega L}{c}\frac{N\mu_{ab}^2}{\hbar W^{ab}\Gamma_{EIT}}.$$

Note that this is the last parameter T_D which also defines the efficiency of the non-linear transformations. So when the driving field intensity exceeds a threshold value and EIT sets in, it is followed by steep dispersion, which is inversely proportional to the EIT linewidth Γ_{EIT}. In its turn, the group velocity of the probe pulse is linearly proportional to the EIT width. So the smaller Γ_{EIT}, the slower the group velocity of light, which is fundamentally limited by the coherence lifetime γ_{cb} in a Doppler broadened gaseous medium or by the inhomogeneous broadening of the low-frequency transition W^{cb} in a solid medium.

D. Comparison of the theory with the experiments on EIT and SGV

It is interesting to compare recent experiments on EIT and SGV with the results of the above theory. In Refs.[71, 76] EIT was observed in a rare-earth doped crystal (Pr^{3+} doped Y_2SiO_5 or Pr :YSO), and in N-V color centers in diamond respectively. All relevant experimental parameters are listed in Table I.

Here w_{ab}, w_{cb} are the population relaxation and γ_{ab}, γ_{cb} are the coherence relaxation rates for $a \rightarrow b$ and $c \rightarrow b$ transitions; $\Delta\nu_{jit}$ is the laser jitter; λ is the linewidth of the $a \rightarrow b$ transition; f is the optical transition oscillator strength; and I is the intensity of the driving laser.

Given the oscillator strength, the dipole moment of the optical transition can be estimated as

$$\mu_{ab}^2 = f\frac{e^2}{\hbar c}\frac{\hbar^2\lambda}{4\pi m_e}, \tag{3.20}$$

and, based on the intensity of the driving field, its Rabi frequency is

$$\Omega = \frac{\sqrt{2\pi}\mu_{ab}}{\hbar\sqrt{cn_0}}\sqrt{I}.$$

We estimated the Rabi frequency used in Ref.[71] to be 500 kHz for $I = 90$

Table I. The parameters of the solid media in the EIT experiments in Refs.[71, 76].

	$2W^{ab}$, GHz	$2W^{cb}$, kHz	w_{ab}^{-1}, μs	γ_{ab}^{-1}, μs	$\Delta\nu_{jit}$, MHz
Pr:YSO	4	< 30	164	111	1
N-V diamond	750	$5.5 \cdot 10^3$	$1.3 \cdot 10^{-2}$	$3.3 \cdot 10^{-3}$	100
	w_{cb}^{-1}, s	γ_{cb}^{-1}, μs	λ, nm	f	I, W/cm^2
Pr:YSO	100	500	605.7	$3 \cdot 10^{-7}$	90
N-V diamond	$5 \cdot 10^{-3}$	40	637	0.1	280

W/cm^2 in the Pr:YSO case, in Ref.[76] the Rabi frequency 160 MHz is cited for the N-V diamond case. The density of Pr-ions in [71] was $N = 4.7 \cdot 10^{18}$ cm^{-3} and the absorption coefficient was $\alpha = 10$ cm^{-1}; for the N-V color centers in [76] the density of centers was $N = 3 \cdot 10^{18}$ cm^{-3} and the peak optical density was ~ 0.3.

In Ref.[71] the system was rather six-level than three-level, and an additional repump field was used, which made only a small fraction of Pr ions, confined within the laser linewidth, interact with the laser fields. For these ions a six-level system was reduced to a three-level Λ scheme with the laser jitter serving as an effective inhomogeneous broadening at the optical transitions, resulting in the width of the absorption spectrum $2W_{eff}^{ab} \sim 1.2$ MHz. Accordingly, the effective density of Pr ions with laser jitter was $4.7 \cdot 10^{18} \cdot \frac{1.2 \cdot 10^6}{4 \cdot 10^9} = 1.41 \cdot 10^{15}$ cm^{-3} or even less depending on the intensity of the repump laser.

The experimental and calculated values of the EIT linewidth and transmission

T and estimates for parameters z and x are given in Table II. As we can see, the theoretically calculated value of the EIT linewidth for Ref.[71] is larger than was observed in the experiment. A possible explanation is that the medium was optically thick (at the 9 mm length of the crystal the optical density was 9) and additional line narrowing of the EIT resonance is expected in this situation [84]. The descripancy in the observed and calculated transmissions for Ref.[76] (about seven times) is probably due to the use of a repump laser, necessary to prevent reorientation of the N-V centers in the diamond lattice.

Using the relation between the dipole moment and oscillator strength (3.20) the ratio of the group velocity to the speed of light, according to (3.19), is

$$V_g/c = \frac{2m_e}{\pi\hbar c}\frac{1}{f}\frac{\hbar c}{e^2}\frac{1}{N/(\Gamma_{EIT}W^{ab})}. \tag{3.21}$$

A group velocity of the order of $1 - 10$ m/s has been achieved in recent experiments in gases. The parameters and results for the group velocity in gases are summarized in Tables III,IV. As it is clear from Table IV, they are in good correspondence with the theoretical calculations on the basis of Eq.(3.21). Note that in the experiment by L.V. Hau *et al.* [24] the Rabi-frequency of the driving laser was an order of magnitude greater than the threshold Rabi-frequency at which EIT starts, so the resonance was power-broadened, which means that $\Gamma_{EIT} = \Omega^2/\gamma_{ab}$. If it were not power-broadened, the EIT width would be just the coherence relaxation rate of the low-frequency transition γ_{cb}, which would lead to $V_g/c \simeq 1.3 \cdot 10^{-10}$ ($V_g \approx 6$ cm/s).

Let us compare now the group velocity, observed in a recent experiment by A.V. Turukhin *et al.* in Pr^{3+}:YSO [24] with the prediction of the above theory. The results are given in Table II and in Fig.8. In Table II we list the experimental value of the group velocity of 45 m/s and the corresponding calculated value of 4000 m/s. The origin of the large difference in V_g (about 90 times) remains unclear. A possible

Table II. The experimental and calculated EIT linewidth, transmission and group velocities for EIT in solid media experiments.

	$2\Gamma_{EIT}^{exp}$, kHz	$2\Gamma_{EIT}^{cal}$, kHz	T^{exp}, %	T^{cal}, %	z	x	V_g^{exp} m/s	V_g^{cal} m/s
Pr^{3+}:YSO	30	230	36	31	$3 \cdot 10^4$	10^5	45	4000
N-V diamond	8500	7800	70	11	5	0.1	–	470

explanation of this descripancy may be the square shape of the probe pulses used in this experiment. A pulse of such shape is considerably modified during propagation in a resonant medium, which may cause an uncertainty in the actual delay time and group velocity. A more detailed comparison with this experiment is shown in Fig.21, where calculated and experimentally observed group velocities (normalized to their maximum values) are given for a range of driving field intensities. We can see that the experimentally observed and theoretically calculated curves look very similar to each other. Also, in Table II we give the theoretical prediction for the possible group velocity in another solid system, namely, N-V color centers in diamond, where EIT has been observed recently [11], but the group velocity has not been measured yet.

E. Solids vs. gases. Potential advantages of solids

As it is clear from the above discussion, the minimum value of the EIT linewidth is defined by W^{cb} and it is achieved when the intensity of the driving laser is about the threshold value needed to observe EIT. In order to minimize inhomogeneous broadening at the spin transition it is preferable to use hyperfine rather than Zeeman splitting, choosing a lattice with the smallest possible nuclear spin of ligands. In some

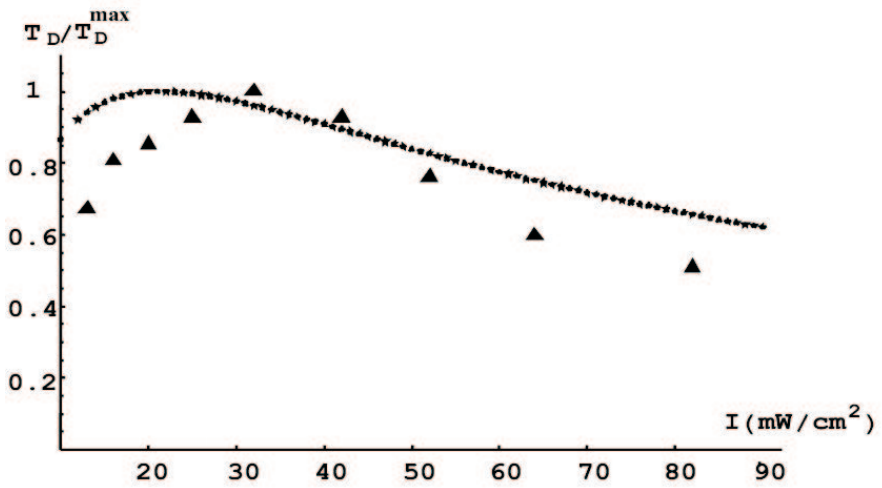

Fig. 21. Experimentally observed (triangles) and calculated (stars) time delay for Pr^{3+}:YSO in the experiment by A.V. Turukhin *et al.* [24].

Table III. The experimental parameters of EIT in gaseous media experiments.

	W^{ab}, MHz	W^{cb}, kHz	γ_{ab}, MHz	w_{ab}, MHz	w_{cb} Hz
M.M. Kash *et al.* [24]	270	10^3	150	3	10^3
L.V. Hau *et al.* [24]	10	20	10	10	$1.6 \cdot 10^4$
	γ_{cb}, Hz	λ, nm	I, mW/cm^2	N, cm^{-3}	f
M.M. Kash *et al.* [24]	10^3	795	10	$2 \cdot 10^{12}$	0.33
L.V. Hau *et al.* [24]	$1.6 \cdot 10^4$	589	12	$8 \cdot 10^{13}$	1

Table IV. The experimental and calculated group velocities for EIT experiments in gaseous media.

	M.M. Kash *et al.* [24]	L.V. Hau *et al.* [24]	D. Budker *et al.* [24]
V_g^{exp}, m/s	90	17	8
V_g^{cal}, m/s	350	21	5

rare-earth doped crystals (for example, Eu^{3+}:Y_2SiO_5, Pr^{3+}:Y_2SiO_5, N-V color centers in diamond) W^{cb} can be of the order of $1-10$ kHz, i.e., of the same order of magnitude as in some EIT experiments in hot gases (M.M. Kash *et al.* [24]) and Bose-Einstein Condensates (BEC's) (L.V. Hau *et al.* [24]), where it is typically defined by the time of flight of atoms through a laser beam. However, W^{cb} in solid materials can not overcome the record value of 1 Hz achieved in experiments with a paraffin coated Rb cell (D. Budker *et al.* [24]).

The EIT threshold intensity in an inhomogeneously broadened medium in general is higher than that in a homogenously broadened medium ($\Omega^2 > \gamma\gamma_{cb}$) by the factor $(W^{cb})^2/\gamma_{cb}w_{cb}$ if $z < 1$ or by the factor $W^{ab}W^{cb}/\gamma\gamma_{cb}$ if $z > 1$. The way to reduce the requirement for the threshold intensity is to use materials with the smallest possible inhomogeneous broadening of the spin transition. Note that for solids with $z < 1$ it does not depend on W^{ab}, while for solids with $z > 1$ it is proportional to the inhomogeneous broadening of an optical transition. In the experiments with solids discussed above $z > 1$ (see Table II). This is the reason the threshold intensities were much higher than in gases. The typical value of the threshold intensity for gaseous media with the parameters listed in Table III is of the order of mW/cm^2 while in experimental works with solids with the parameters listed in Table I it is of the order of $10 - 10^3$ W/cm^2. In the case $z > 1$ it is reasonable

also to use electric-dipole allowed optical transitions in combination with the smallest possible inhomogeneous broadening of the optical transition. There is a wide class of rare-earth ion doped dielectrics possesing a zero phonon line at low temperature (up to 10 K) at the electric-dipole allowed $f - d$ transitions lying in the band-gap of a host matrix. Some examples include: Yb^{2+}:MgF_2, Pr^{3+}:Cs_2NaYCl_6, Ce^{3+}:Cs_2NaYCl_6, Ce^{3+}:$LuPO_4$, Ce^{3+}:YPO_4, Ce^{3+}:YAG, Ce^{3+}:$CaSO_4$, Tb^{3+}:$LiYF_4$, Eu^{2+}:CaS, Eu^{2+}:MgS, Eu^{2+}:MgF_2, Eu^{2+}:CaF_2, Np^{4+}:$ZrSrO_4$, Pa^{4+}:Cs_2ZrCl_6. Although the inhomogeneous width of a dipole-allowed optical transition is usually greater than that of a dipole-forbidden, there is no linear dependence between the dipole moment and the inhomogeneous width, so the later can be reduced by controlling the quality of the crystal sample. There are some rare-earths, namely, Pr^{3+} [85], Ce^{3+} [98], Eu^{2+} [87] and Tb^{3+} [88], whose dipole-allowed $f - d$ transitions in different hosts have relatively small inhomogeneous optical line broadening, ranging from 40 GHz to 300 GHz. Note that inhomogeneous line broadening can be effectively reduced down to the magnitude of the laser jitter (which can be as small as 1 kHz [89]) using an optical repump scheme as it was done in [71]. This effectively reduces the requirement for the EIT threshold intensity. The price to be paid for this is a corresponding reduction in the effective atomic density of the dopants participating in EIT.

Let us compare now the dispersive properties of EIT in gases and solids in order to estimate the potential of solid materials for the slowing of light and realization of nonlinear interactions.

On the basis of Eq.(3.21) the general recipe for achieving a slow group velocity is using highest possible dopant density, electric-dipole allowed transitions, and the smallest possible inhomogeneous line broadening at both the spin and optical transitions.

One of the major advantages of solids as compared to gases is the high concentration. The concentration of dopants in solids can be much greater (about $10^{18} - 10^{22}$ cm^{-3}) than the atomic density in gases (about $10^{10} - 10^{13}$ cm^{-3}) for which atomic collisions do not broaden the optical and spin transitions. This is crucial for the slowing of light and for the efficiency of nonlinear processes.

Taking a combination of favorable parameters such as the density of impurity ions of $N \sim 10^{22}$ cm^{-3}, the inhomogeneous width of the spin transition $W^{cb} \sim 10$ kHz and the inhomogeneous width of the dipole-allowed ($f \sim 0.1$) optical transition $W^{ab} \sim 50$ GHz, and assuming that the EIT resonance is not power-broadened, one can obtain:

$$V_g/c \simeq 10^{-13} \ (V_g \approx 30 \mu m/s).$$

Unfortunately in real materials it is difficult to realize such a favorable combination of parameters.

Let us consider Ce^{3+} doped crystals like YAG, $LuPO_4$, YPO_4, $YLiF_4$, and Cs_2NaYCl_6. The relatively high oscillator strength $f \sim 10^{-4}$ in these materials is nicely combined with relatively small inhomogenous broadening of the optical transition: $W^{ab} \sim 100$ GHz [90]. Unfortunately there is no hyperfine structure (the spin of Ce nuclei is zero) and inhomogeneous broadening at the Zeeman transition is typically rather large: $W^{cb} \sim 1 - 10$ MHz [91]. At the density of dopants $N = 10^{20}$ cm^{-3}, it would give us $V_g \approx 200$ m/s. The required intensity to observe EIT in such crystal would be rather high, $I_{thres} \approx 5$ kW/cm^2.

Another example is Eu^{2+}-doped crystals like Eu^{2+}:CaF_2, Eu^{2+}:SrF_2, Eu^{2+}:MgF_2, and Eu^{2+}:MgS. In these materials inhomogeneous broadening of the spin transition is rather small: $W^{cb} \sim 10$ kHz [92], $W^{ab} = 40 - 60$ GHz [87], and the density of dopants can be relatively large: $N \approx 10^{19}$ cm^{-3}. There is also a zero-phonon line

at the $4f - 5d$ electric-dipole allowed optical transition with the oscillator strength $f \sim 10^{-4}$ [87] and the wavelengths $\lambda = 401 - 424$ nm. According to Eq.(3.21), at the density of dopants $N = 10^{19}$ cm^{-3}, this should lead to $V_g \approx 10$ m/s. The EIT threshold intensity would be $I_{thres} \approx 400$ W/cm^2. In Eu^{2+}:MgS the inhomogeneous width of the $f - d$ transition is rather large $W^{ab} \sim 6$ THz [93], but the oscillator strength of the transition is $f \sim 0.01 - 0.02$ [93, 94]. The wavelength of the $4f - 5d$ transition is $\lambda = 578$ nm in this crystal. If we assume the width of the spin transition $W^{cb} \sim 10$ kHz and the density of dopant ions $N = 10^{19}$ cm^{-3}, this gives the group velocity estimate $V_g \approx 20$ m/s. The intensity of the driving laser required for EIT to be observed would be $I_{thres} \approx 600$ W/cm^2.

It is worth mentioning one more requirement to the proposed solid materials. It is desirable that in the Λ-system under consideration both optical transitions be of comparable strength to avoid using high laser power. In principle, if the lower levels are different spin levels, both transitions to a common upper level cannot be allowed, since spin is conserved in optical transitions. This restriction can be overcome eigher by mixing of spin levels by an external magnetic field [76] or by using atoms or ions with strong spin-orbit coupling in the case of electronic Zeeman lower levels, or strong spin-orbit and hyperfine interactions for hyperfine lower levels. These interactions lead to mixing of different electronic (nuclear) spin wave functions with spatial ones, thus making both optical transitions allowed. The rare-earth ions doped into dielectric crystals which we discuss above possess strong spin-orbit interaction because of their high atomic numbers, so transitions from Zeeman sublevels to a common upper level may be of equal strength [95]. In the case of hyperfine lower levels it is harder to find transitions with comparable strength, since the hyperfine interaction is small, and generally only transitions that preserve the nuclear spin I_z, are allowed. However, in hosts where a rare-earth ion occupies a site of low symmetry, nuclear state mixing by

the crystal field can give rise to $\Delta I_z \neq 0$ transitions of comparable intensity [95, 96].

CHAPTER IV

SUPPRESSION OF EXCITED-STATE ABSORPTION IN LASER CRYSTALS USING ELECTROMAGNETICALLY INDUCED TRANSPARENCY

Currently, a lot of experimental effort in solid-state optics is devoted to searching for laser materials suitable for tunable lasing, primarily in ultraviolet (UV) and vacuum ultraviolet (VUV) spectral regions. Mainly, researchers focus on optical crystals doped with either transition metal or rare-earth ions [97]. The latter doped into wide bandgap dielectric crystals have spectrally broad vibronic emission bands associated with $4f^{n-1}5d \leftrightarrow 4f^n$ interconfigurational transitions, whose energies lie mostly in UV or VUV regions of the spectrum. The transitions are electric dipole allowed; therefore have large absorption and emission cross-sections, and are promising for efficient tunable laser action. Interest in impurity-doped crystals is also motivated by the fact that similar lasing media in the visible and near infrared are very robust and easy to operate. The most famous examples are Ti:Sapphire, Cr:LiCaF, Ce:LiCaF, and fixed-wavelength Nd:YAG, Nd:YLF, and Yb:YAG systems which can deliver high laser power both in continuous wave and pulsed regimes.

However, not much progress has been made in developing solid-state UV and VUV lasers. Thus far laser action in the UV was realized in several Ce^{3+} doped dielectric host materials, emitting wavelengths tunable in the range $270 - 310$ nm [98]; in the VUV region only Nd^{3+}:LaF_3 demonstrates lasing with exceptionally large photon energy corresponding to 172 nm wavelength with the possibility of tuning from 170 nm to 175 nm [99]. Most of the materials in which laser oscillation has been observed are listed in [97, 100].

There are two major obstacles in the way of making an impurity-doped crystal lase in the UV or VUV. First of all, one has to create population inversion at an

operating transition, which requires very high pump power densities, scaling as ν^3 with the frequency of the pump. This problem can be rather satisfactorily solved by introducing two- or three-step pumping via intermediate states of a dopant ion with visible or near-UV light (see, for example, [101]). It also helps to prevent formation of color center defects, produced by strong UV pumping and causing additional optical losses. The second problem is more fundamental. It is the so called excited-state absorption (ESA), i.e. absorption from metastable laser levels to higher-energy states. The terminal state for ESA can be either a higher-lying discrete level or the conduction band (CB) of a crystal. In the majority of rare-earth ion doped materials ESA at emission or/and pump wavelengths reduces the efficiency or completely prohibits laser action. This happens if the ESA cross-section σ_{ESA} exceeds the stimulated-emission cross-section σ_{SE}. For Nd^{3+}:LaF_3 and Ce^{3+} doped materials lasing is possible because, luckily, $\sigma_{SE} > \sigma_{ESA}$. Moreover, in many cases ESA prevents lasing not only in the UV and VUV parts of the spectrum, but also in the visible and in the infrared. Some (but not the only) examples of the materials in which laser action cannot be observed due to ESA are the following: Ce^{3+}:YAG [103] (red to green luminescence), Yb^{2+}:CaF_2 [100] (red to blue luminescence), Yb^{2+}:MgF_2 [104] (blue luminescence), Eu^{2+}:CaF_2 [106] (blue luminescence), Pr^{3+}:YAG [102] (blue to near UV luminescence), Pr^{3+}:YLF [105] (UV luminescence), Nd^{3+}:YLF [107] (VUV luminescence) and many others.

In this chapter a method for reduction of excited-state absorption is considered [108], which makes use of the EIT phenomenon [17, 18]. Namely, absorption from a populated excited electronic state can be suppressed under the action of an additional driving coherent field, resonantly coupling the terminal state of ESA to some intermediate discrete state. We mainly focus on the possibility to suppress ESA at a desired wavelength of laser oscillation in rare-earth ion doped laser materials.

A. Typical ESA configurations

Let us first review common configurations in which ESA can prevent laser action. The main focus will be on ESA reduction in wide bandgap optical crystals doped with divalent or trivalent rare-earth ions because these materials are considered to be the most promising for UV and VUV solid-state lasing.

Typically, rare-earth ions enter crystals in a trivalent state, but some of them (Ce, Eu, Yb, Tm, and Sm) can be stabilized in a divalent state. In both cases the ground state of a rare-earth ion is $4f^n$ with Ce^{2+} being the only exception [109]. Energies of excited $4f^n$ levels typically extend from the IR into the VUV region while energies of $4f^{n-1}5d$ levels mostly lie in the UV and VUV parts of the spectrum. Parity-forbidden $4f^n \leftrightarrow 4f^n$ transitions are rather weak (typical absorption and stimulated emission cross-sections are $\sigma \sim 10^{-21} \div 10^{-20}$ cm^2) compared to much stronger parity-allowed $4f^n \leftrightarrow 4f^{n-1}5d$ transitions ($\sigma \sim 10^{-19} \div 10^{-18}$ cm^2). Having at the same time broad emission and absorption bands, these interconfigurational transitions offer the potential for wavelength-tunable laser operation. $4f^n \leftrightarrow 4f^n$ transitions can be used for laser operation at a fixed wavelength in the UV or VUV.

The terminal level for ESA can be either a higher lying discrete state (Fig.22a) or continuum states in the CB (Fig.22b). In the next subsections we will analyze these two configurations separately and derive conditions for ESA suppression due to EIT. ESA can also originate from charge transfer processes, but we do not consider this situation.

1. Discrete terminal level for ESA

Consider the situation, depicted in Fig.22a, in which ESA occurs from an upper operating state of a laser transition to a higher-lying discrete state. By resonantly

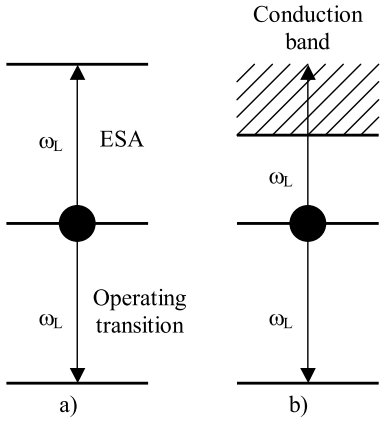

Fig. 22. ESA at the laser oscillation wavelength in crystals activated with rare-earth and transition metal ions.

coupling the terminal state 4 of the ESA transition to some auxiliarly state 3 by an additional driving field, one can suppress absorption of the emitted field, as is depicted in Fig.23.

It is worth to mention that in Refs.[110] the idea of using an additional control field in order to manipulate absorption properties of a medium was applied to inhibit two-photon absorption (TPA). TPA from a ground state to some excited state as well as stepwise excitation were suppressed by using the control field, coupling an intermediate state via which TPA occured, to some auxiliarly state. In the system which we consider it is absorption from the excited, not the ground, state that is to be suppressed; therefore the additional driving field has to couple the auxiliarly state to the terminal rather than to the initial state of the ESA transition. In the case of a discrete terminal level, as in Fig.23, the additional state 3 can be either of lower or higher energy with respect to the terminal state 4, so that the ESA transition $2 \leftrightarrow 4$ and the adjacent transition $3 \leftrightarrow 4$ can form either Λ- or ladder-systems, provided that the coherence at the two-photon transition $2 \leftrightarrow 3$ is sufficiently long-lived.

In order to derive conditions, at which laser oscillation can be achieved, we

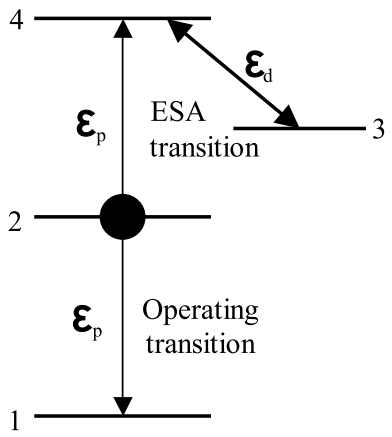

Fig. 23. ESA to discrete terminal level and the scheme of its suppression by an additional coherent driving field.

consider linear gain/loss for a weak probe field ε_p in an active medium. To that end we calculate the total optical polarization of the medium due to the probe field resonant with transitions $2 \leftrightarrow 1$ and $4 \leftrightarrow 2$. The ultimate goal is to obtain conditions under which the probe field is amplified in the presence of the driving field while in the absence of one it is absorbed.

Density matrix equations, describing medium polarization in a linear approximation with respect to the probe field, can be written in the following form:

$$\dot{\sigma}_{42} + i\left(\omega_{42} - \omega_p\right)\sigma_{42} + i\frac{\varepsilon_p \mu_{42}}{2\hbar}(\rho_{44} - \rho_{22}) - i\frac{\varepsilon_d \mu_{43}}{2\hbar}\sigma_{32} = -\gamma_{42}\sigma_{42}, \tag{4.1}$$

$$\dot{\sigma}_{21} + i\left(\omega_{21} - \omega_p\right)\sigma_{21} + i\frac{\varepsilon_p \mu_{21}}{2\hbar}(\rho_{22} - \rho_{11}) = -\gamma_{21}\sigma_{21}, \tag{4.2}$$

$$\dot{\sigma}_{32} + i\left(\omega_{32} + \omega_d - \omega_p\right)\sigma_{32} - i\frac{\varepsilon_d^* \mu_{43}^*}{2\hbar}\sigma_{42} + i\frac{\varepsilon_p \mu_{42}}{2\hbar}\sigma_{43}^* = -\gamma_{32}\sigma_{32}, \tag{4.3}$$

$$\dot{\sigma}_{43} + i\left(\omega_{43} - \omega_d\right)\sigma_{43} + i\frac{\varepsilon_d \mu_{43}}{2\hbar}(\rho_{44} - \rho_{33}) - i\frac{\varepsilon_p \mu_{42}}{2\hbar}\sigma_{32}^* = -\gamma_{43}\sigma_{43}. \tag{4.4}$$

Here ω_p and ω_d are the frequencies of the probe and driving fields respectively, μ_{mn} is the dipole moment of the $m \leftrightarrow n$ transition, σ_{mn} are the complex amplitudes of the off-diagonal density matrix elements in the rotating-wave approximation (RWA) and

γ_{mn} are their corresponding decay rates.

A steady-state solution of the above set of equations yields the following result for the complex amplitude of a net polarization of the medium at the probe field frequency:

$$P = N\left(\sigma_{21}\mu_{12} + \sigma_{42}\mu_{24}\right) = i\frac{\varepsilon_p N}{2\hbar}\left(\frac{|\mu_{21}|^2(\rho_{11}-\rho_{22})}{i(\omega_{21}-\omega_p)+\gamma_{21}} + \right.$$
$$\left. + \frac{|\mu_{42}|^2\left(\rho_{22}-\rho_{44}+|\frac{\varepsilon_d\mu_{43}}{2\hbar}|^2\frac{\rho_{33}-\rho_{44}}{(i(\omega_{43}-\omega_d)-\gamma_{43})(i(\omega_{32}-\omega_p+\omega_d)+\gamma_{32})}\right)}{i(\omega_{42}-\omega_p)+\gamma_{42}+\left|\frac{\varepsilon_d\mu_{43}}{2\hbar}\right|^2\frac{1}{i(\omega_{32}-\omega_p+\omega_d)+\gamma_{32}}}\right), \tag{4.5}$$

where we neglect inhomogeneous broadening of both the one- and two-photon transitions. The negative or positive sign of the imaginary part of Eq.(4.5) determines whether the probe field is amplified or absorbed, respectively, in the medium. We are interested in the case of exact resonance of the probe field with the inverted transition $2 \leftrightarrow 1$ ($\omega_p = \omega_{21}$) and exact resonance of the driving and probe fields with the two-photon transition $3 \leftrightarrow 2$ ($\omega_p - \omega_d = \omega_{32}$). Let us assume also that initially only state 2 is populated. Then, the imaginary part of the polarization takes the form:

$$Im(P) = -\frac{\varepsilon_p N}{2\hbar}\left(\frac{|\mu_{21}|^2}{\gamma_{21}} - \frac{|\mu_{42}|^2\left(\gamma_{42}+|\Omega_d|^2/\gamma_{32}\right)}{(\omega_{42}-\omega_p)^2+\left(\gamma_{42}+|\Omega_d|^2/\gamma_{32}\right)^2}\right), \tag{4.6}$$

where $\Omega_d = \varepsilon_d\mu_{43}/2\hbar$ is the Rabi frequency of the driving field.

All terms in Eq.(4.6) have clear physical meaning. The first one describes amplification of the probe field in the presence of inversion at the laser transition $2 \leftrightarrow 1$ while the second one describes ESA, modified by the driving field. If $\Omega_d = 0$ (no driving field), the imaginary part of the polarization reads

$$Im(P) = -\frac{\varepsilon_p N}{2\hbar}\left(\frac{|\mu_{21}|^2}{\gamma_{21}} - \frac{|\mu_{42}|^2\gamma_{42}}{(\omega_{42}-\omega_p)^2+\gamma_{42}^2}\right). \tag{4.7}$$

A positive sign of this expression means that $\sigma_{ESA} > \sigma_{SE}$ and no gain for the probe field is possible in the medium. However, for rather strong driving field ($|\Omega_d|^2 >$

$|\Omega_{th}|^2 = \gamma_{32}\gamma_{42}$) ESA can be suppressed by a factor of $|\Omega_d|^2/\gamma_{32}\gamma_{42}$ in the center of the ESA line. Note that the threshold Rabi frequency Ω_{th} of the driving field corresponds to the standard EIT threshold [17]. It is expected since transitions $2 \leftrightarrow 4$ and $3 \leftrightarrow 4$ form a Λ-system, in which one-photon absorption from state 2 is suppressed due to EIT if a strong driving field is applied to the adjacent transition. In order to achieve gain the driving field Rabi frequency has to match the condition

$$|\Omega_d|^2 > |\Omega_0|^2 = \frac{\sigma_{ESA}}{\sigma_{SE}}\Omega_{th}. \tag{4.8}$$

In the above analysis inhomogeneous broadening was not taken into account. In a solid medium the standard EIT threshold Rabi frequency in a Λ-system is modified. As is shown in Chapter III, in the case of rare-earth ion doped crystals the modification is that inhomogeneous linewidths of transitions have to be substituted instead of homogeneous ones, so that $|\Omega_{th}|^2 = W_{42}^{inh}W_{32}^{inh}$.

2. Suppression of ESA at infrared transitions with a visible control field used also as a pump

Let us consider the level scheme depicted in Fig.24, which is typical for ESA in transition metal ion doped crystals. Emission from the metastable laser level 3 terminates in the phonon sideband of the ground state, and the phonon state 2 rapidly (in *ps* time) decays into the ground electronic state 1. ESA originates from the excited electronic state 3 and typically terminates in some state 5 in the absorption band of a higher-lying excited electronic state 4. The state 5 also rapidly decays to the electronic state 4. So in the scheme of Fig.24 states 1, 3 and 4 are metastable and the states 2, 5 are rapidly decaying. It is desirable that the state 4 rapidly decay non-radiatively to the state 3 so that it does not accumulate population. We also assume that the decay from the state 4 goes mostly to the state 3.

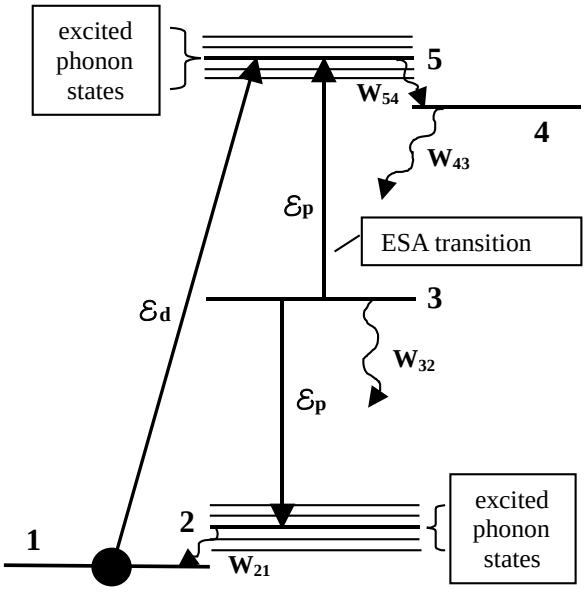

Fig. 24. Typical ESA configuration in transition metal ion doped laser crystals.

Excited-state absorption in this case can be suppressed using the driving field of shorter wavelength, as is shown in Fig.24. An additional advantage of this scheme is that the driving field can also serve as a pump, transferring population from the ground state 1 to the upper laser level 3.

In order to obtain the conditions at which amplification is possible in the system, we again analyze linear gain/loss for a weak probe field in the presence of a strong driving field, assuming that initially all population is in the ground state. Two electromagnetic fields are applied:

$$\varepsilon = \frac{1}{2}\sum_j \varepsilon_i e^{-i\omega_j t + ik_j z} + c.c.,\ j = p, d,$$

where ε_p, ε_d are the slowly varying amplitudes of the electric field components of the probe and driving fields, respectively; $\omega_{p,d}$ and $k_{p,d}$ are the corresponding frequencies and wavenumbers. Fields are assumed to be plane waves propagating in the z-direction.

Solution of the following dynamic equations for amplitudes σ_{ml} of the density matrix elements ρ_{ml}, determined in RWA by standard formulae: $\rho_{32} = \sigma_{32}e^{-i\omega_p t + ik_p z}$, $\rho_{53} = \sigma_{53}e^{-i\omega_p t + ik_p z}$, $\rho_{31} = \sigma_{31}e^{-i(\omega_d - \omega_p)t + i(k_{d-}k_p)z}$, $\rho_{51} = \sigma_{51}e^{-i\omega_d t + ik_d z}$, will give the medium polarization in a linear approximation with respect to the probe field:

$$\dot{\sigma}_{32} + \left(\gamma_{32} + i(\omega_{32} - \omega_p)\right)\sigma_{32} + i\frac{\varepsilon_p \mu_{32}}{2\hbar}\left(\rho_{33} - \rho_{22}\right) = 0, \tag{4.9}$$

$$\dot{\sigma}_{53} + \left(\gamma_{53} + i(\omega_{53} - \omega_p)\right)\sigma_{53} + i\frac{\varepsilon_p \mu_{53}}{2\hbar}\left(\rho_{55} - \rho_{33}\right) - i\frac{\varepsilon_d \mu_{51}}{2\hbar}\sigma_{31}^* = 0, \tag{4.10}$$

$$\dot{\sigma}_{31} + \left(\gamma_{31} + i(\omega_{31} - \omega_d + \omega_p)\right)\sigma_{31} + i\frac{\varepsilon_d \mu_{51}}{2\hbar}\sigma_{53}^* - i\frac{\varepsilon_p^* \mu_{53}^*}{2\hbar}\sigma_{51} = 0, \tag{4.11}$$

$$\dot{\sigma}_{51} + \left(\gamma_{51} + i(\omega_{51} - \omega_d)\right)\sigma_{51} + i\frac{\varepsilon_d \mu_{51}}{2\hbar}\left(\rho_{55} - \rho_{11}\right) - i\frac{\varepsilon_p \mu_{53}}{2\hbar}\sigma_{31} = 0, \tag{4.12}$$

where ω_{ml} is the frequency of the $m \leftrightarrow l$ transition, μ_{ml} is the corresponding dipole moment, and γ_{ml} is the decay rate of the coherence at the corresponding transition. In

the steady-state regime the solution of these equations gives the following expression for the medium polarization at the probe field wavelength:

$$P = N(\sigma_{32}\mu_{23} + \sigma_{53}\mu_{35}) = i\frac{\varepsilon_p N}{2\hbar}\left(\frac{|\mu_{32}|^2(\rho_{22}-\rho_{33})}{i(\omega_{32}-\omega_p)+\gamma_{32}}+\right.$$

$$\left.+|\mu_{53}|^2\frac{(\rho_{33}-\rho_{55})(\gamma_{31}-i(\omega_{31}-\omega_d+\omega_p))-|\Omega_d|^2\frac{\rho_{11}-\rho_{55}}{\gamma_{51}-i(\omega_{51}-\omega_d)}}{(\gamma_{53}+i(\omega_{53}-\omega_d))(\gamma_{31}-i(\omega_{31}-\omega_d+\omega_p))}\right). \quad (4.13)$$

We need to analyze the case of an exact one- and two-photon resonance: $\omega_p = \omega_{32} = \omega_{53}$ and $\omega_d - \omega_p = \omega_{31}$, since in this case EIT is the most prominent.

The imaginary part of the polarization is:

$$Im(P) = \frac{\varepsilon_p N}{2\hbar}\left(\frac{|\mu_{32}|^2(\rho_{22}-\rho_{33})}{\gamma_{32}} + |\mu_{53}|^2\frac{(\rho_{33}-\rho_{55})\gamma_{31}-|\Omega_d|^2(\rho_{11}-\rho_{55})/\gamma_{51}}{\gamma_{53}\gamma_{31}+|\Omega_d|^2}\right). \quad (4.14)$$

The first term in Eq.(4.14) describes amplification of the probe field in the presence of inversion at the laser transition $3 \leftrightarrow 2$, the second one describes ESA of the probe field from the upper operating level 3 and the third term gives the modification of ESA by the driving field and originates from the coherence σ_{31}.

Since the driving field also serves as a pump, it also determines level populations, so that

$$\rho_{11} = \frac{1+2\frac{|\Omega_d|^2}{W_{54}\gamma_{51}}}{1+2\frac{|\Omega_d|^2}{\gamma_{51}}\left(\frac{1}{W_{32}}+\frac{1}{W_{43}}\right)}, \quad (4.15)$$

$$\rho_{22} = \frac{2\frac{|\Omega_d|^2}{W_{21}\gamma_{51}}}{1+2\frac{|\Omega_d|^2}{\gamma_{51}}\left(\frac{1}{W_{32}}+\frac{1}{W_{43}}\right)}, \quad (4.16)$$

$$\rho_{33} = \frac{2\frac{|\Omega_d|^2}{W_{32}\gamma_{51}}}{1+2\frac{|\Omega_d|^2}{\gamma_{51}}\left(\frac{1}{W_{32}}+\frac{1}{W_{43}}\right)}, \quad (4.17)$$

$$\rho_{55} = \frac{2\frac{|\Omega_d|^2}{W_{54}\gamma_{51}}}{1+2\frac{|\Omega_d|^2}{\gamma_{51}}\left(\frac{1}{W_{32}}+\frac{1}{W_{43}}\right)}, \quad (4.18)$$

$$\rho_{44} = 1-\rho_{11}-\rho_{22}-\rho_{33}-\rho_{55}, \quad (4.19)$$

where W_{ml} are population decay rates (see Fig.24), we assumed that $W_{21},\ W_{54} \gg W_{32},\ W_{43}$. Taking into account that $W_{43} >> W_{32}$ and that the driving field is suffuciently strong such that $|\Omega_d|^2 >> \gamma_{51}W_{32}$, the populations are

$$\rho_{11} \approx \frac{1}{1+\frac{2|\Omega_d|^2}{\gamma_{51}W_{32}}} \approx 0,$$

$$\rho_{22} \approx \frac{W_{32}}{W_{21}} \approx 0,$$

$$\rho_{33} \approx \frac{\frac{2|\Omega_d|^2}{\gamma_{51}W_{32}}}{1+\frac{2|\Omega_d|^2}{\gamma_{51}W_{32}}} \approx 1,$$

$$\rho_{55} \approx \frac{W_{32}}{W_{54}} \approx 0,$$

$$\rho_{44} \approx 0.$$

Finally we arrive at the following result for the imaginary part of the polarization:

$$Im(P) = \frac{\varepsilon_p N}{2\hbar} \frac{2\left|\Omega_d\right|^2/\gamma_{51}W_{32}}{1+\frac{2|\Omega_d|^2}{\gamma_{51}W_{32}}} \left(-\frac{\left|\mu_{32}\right|^2}{\gamma_{32}} + \frac{\left|\mu_{53}\right|^2}{\gamma_{53}} \frac{1-W_{32}/2\gamma_{31}}{1+\frac{|\Omega_d|^2}{\gamma_{53}\gamma_{31}}} \right), \tag{4.20}$$

which shows that ESA can be suppressed in the EIT regime, when the driving field Rabi frequency exceeds a threshold value:

$$\left|\Omega_d\right|^2 \gg \left|\Omega_d\right|^2_{th} = \gamma_{53}\gamma_{31} \tag{4.21}$$

such that the second term in Eq.(4.20) is less than the first one resulting in $Im(P) < 0$, i.e., amplification.

3. ESA into the conduction band

In this subsection we show that ESA terminating in the CB of a host material can be reduced in a similar way as in the case of a discrete terminal level. The phenomenon of inhibited photoionization has been known since 1961 when Fano theo-

retically explained experimental data on photoionization reduction in helium arising from interaction of a discrete autoionizing state, imbedded into the continuum, with continuum states [10]. The origin of the reduction is the destructive interference of probability amplitudes of two pathways leading to ionization. Later, it was discovered that a Fano-type continuum structure can be realized in a structureless continuum by admixing a bound electronic state into the continuum with a laser [19]. This phenomenon is called laser-induced continuum structure (LICS) and it is very well studied in rare gases (for recent experimental results, see, for example, [111] and references therein).

In order to show that ESA into the CB can be reduced in the same manner as in the previous subsection, we consider a simple four-level model system, depicted in Fig.25, in which the state 4 is now replaced by continuum electronic states in the CB. We treat it as a structureless non-degenerate one-dimensional continuum, which means that each electronic energy state in the CB is described by only one quantum number - its energy. This assumption will make our consideration much simpler and reveal the essential physics of the problem. In reality, however, more than one continuum can be involved in the ESA process. For example, in the case of ESA originating from a $4f^{n-1}5d$ level, the terminal state of an electron in the CB can be either p-like or f-like.

The following assumptions are used in the analysis: 1) the medium is prepared in state 2, so that no other state is populated; 2) both probe and driving fields couple corresponding discrete levels to the same continuum; 3) fields are resonant only with transitions designated in Fig.25; 4) wave-mixing processes are neglected; 5) only the linear response of the medium to the probe field is analyzed in order to calculate the linear gain.

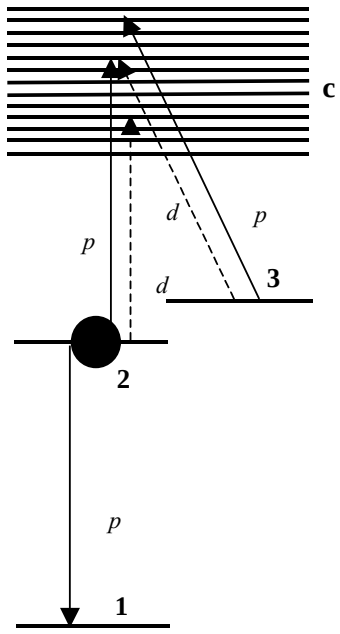

Fig. 25. ESA to continuum terminal levels.

The wave function, describing this three-level+continuum system, is

$$|\Psi >= A_1|1 > +A_2|2 > +A_3|3 > + \int C|c > dE_c.$$

The Hamiltonian of the system is $\widehat{H} = \widehat{H}_0 + \widehat{V}$, where the non-perturbed and perturbation Hamiltonians are given by the expressions:

$$\widehat{H}_0 = E_1|1 >< 1| + E_2|2 >< 2| + E_3|3 >< 3| + \int E_c|c >< c|dE_c,$$

$$\widehat{V} = -\mu_{21}\varepsilon|2 >< 1| - \int \mu_{c2}\varepsilon|c >< 2|dE_c - \int \mu_{c3}\varepsilon|c >< 3|dE_c + h.c.,$$

and two laser fields are applied:

$$\varepsilon = \sum_j \frac{\varepsilon_j}{2} e^{-i\omega_j t + ik_j z} + c.c.,\ j = p, d.$$

Similar to the previous subsection ε_p is the probe field, which is absorbed from the emitting level 2 into the continuum and amplified at the $2 \leftrightarrow 1$ transition; ε_d is the driving field, applied at the adjacent $3 \leftrightarrow c$ transition, which inhibits ESA of the probe field if certain conditions are met, as will be shown below. Both fields are assumed to be plane waves propagating in the z-direction.

Writing the complex amplitudes of the quantum states in the form $a_n = A_n e^{iE_n t/\hbar}$, $c = Ce^{iE_c t/\hbar}$, using the RWA, and adiabatically eliminating the continuum following the procedure of Ref.[19], we effectively reduce the system to a three-level one:

$$i\hbar\frac{\partial a_1}{\partial t} = -\frac{\mu_{12}\varepsilon_p^*}{2}a_2 e^{-i((E_2-E_1)/\hbar-\omega_p)t-ik_p z}, \tag{4.22}$$

$$\begin{aligned} i\hbar\frac{\partial a_2}{\partial t} = &-\frac{\mu_{21}\varepsilon_p}{2}a_1 e^{i((E_2-E_1)/\hbar-\omega_p)t+ik_p z} - a_2\left(\frac{|\varepsilon_p|^2}{4\hbar}\left(P_2^p + i\Gamma_2^p/2\right) + \frac{|\varepsilon_d|^2}{4\hbar}\left(P_2^d + i\Gamma_2^d/2\right)\right) \\ &-a_3\frac{\varepsilon_p^*\varepsilon_d}{4\hbar}e^{-i((E_3-E_2)/\hbar-\omega_p+\omega_d)t-i(k_p-k_d)z}\left(\Pi_{23}^d + iG_{23}^d/2\right), \end{aligned} \tag{4.23}$$

$$\begin{aligned} i\hbar\frac{\partial a_3}{\partial t} = &-a_3\left(\frac{|\varepsilon_p|^2}{4\hbar}\left(P_3^p + i\Gamma_3^p/2\right) + \frac{|\varepsilon_d|^2}{4\hbar}\left(P_3^d + i\Gamma_3^d/2\right)\right) \\ &-a_2\frac{\varepsilon_p\varepsilon_d^*}{4\hbar}e^{i((E_3-E_2)/\hbar-\omega_p+\omega_d)t+i(k_p-k_d)z}\left(\Pi_{32}^p + iG_{32}^p/2\right). \end{aligned} \tag{4.24}$$

Here we introduce the following notations:

$$\begin{aligned} P_m^l + i\Gamma_m^l/2 &= \lim_{\eta\to+0}\int\frac{|\mu_{cm}|^2\,dE_c}{(E_c-E_m)/\hbar-\omega_l-i\eta} = \\ &= P\int\frac{|\mu_{cm}|^2\,dE_c}{(E_c-E_m)/\hbar-\omega_l} + i\pi\hbar\,|\mu_{cm}|^2_{E_c=E_m+\hbar\omega_l}, \end{aligned} \tag{4.25}$$

$$\begin{aligned} \Pi_{sq}^l + iG_{sq}^l/2 &= \lim_{\eta\to+0}\int\frac{\mu_{sc}\mu_{cq}dE_c}{(E_c-E_m)/\hbar-\omega_l-i\eta} = \\ &= P\int\frac{\mu_{sc}\mu_{cq}dE_c}{(E_c-E_m)/\hbar-\omega_l} + i\pi\hbar\mu_{sc}\mu_{cq}|_{E_c=E_m+\hbar\omega_l}, \end{aligned} \tag{4.26}$$

with $s, q, m = 2$ or 3 and $l = p$ or d. In the above expressions P_m^l is the dynamic Stark shift of the m-th state due to interaction with the l-th component of the optical

field, Γ_m^l is the ionization rate of the m-th level due to the l-th field, and Π_{sq}^l and G_{sq}^l together determine the magnitude and the phase of the coherence at the transition $s \leftrightarrow q$ excited due to a Raman process via the continuum.

Let us now turn to the dynamic equations for amplitudes σ_{ml} of the density matrix $\rho_{ml} = A_m A_l^*$, determined by standard formulae: $\sigma_{21} = \rho_{21} e^{-i\omega_p t + ik_p z}$, $\sigma_{32} = \rho_{32} e^{-i(\omega_p - \omega_d)t + i(k_p - k_d)z}$, $\sigma_{31} = \rho_{31} e^{-i(2\omega_p - \omega_d)t + i(2k_p - k_d)z}$. From Eqs.(4.22)-(4.24) one finds:

$$\frac{\partial \sigma_{21}}{\partial t} = -\sigma_{21}\Delta_{21} + i\Omega_p(\rho_{11} - \rho_{22}) + i\frac{\varepsilon_p^* \varepsilon_d}{4\hbar^2}\sigma_{31}\left(\Pi_{23}^d + iG_{23}^d/2\right), \tag{4.27}$$

$$\frac{\partial \sigma_{32}}{\partial t} = -\sigma_{32}\Delta_{32} - i\Omega_p^*\sigma_{31} + i\frac{\varepsilon_p \varepsilon_d^*}{4\hbar^2}\left(\rho_{22}\left(\Pi_{32}^p + iG_{32}^p/2\right) - \rho_{33}\left(\left(\Pi_{23}^d\right)^* - i\left(G_{23}^d\right)^*/2\right)\right), \tag{4.28}$$

$$\frac{\partial \sigma_{31}}{\partial t} = -\sigma_{31}\Delta_{31} - i\Omega_p\sigma_{32} + i\frac{\varepsilon_p \varepsilon_d^*}{4\hbar^2}\sigma_{21}\left(\Pi_{32}^p + iG_{32}^p/2\right), \tag{4.29}$$

where we use the Rabi frequency of the probe field $\Omega_p = \mu_{21}\varepsilon_p/2\hbar$, and complex dressed decay rates

$$\Delta_{21} = \gamma_{21} + \frac{|\varepsilon_p|^2}{4\hbar^2}\frac{\Gamma_2^p}{2} + \frac{|\varepsilon_d|^2}{4\hbar^2}\frac{\Gamma_2^d}{2} + i\left(\frac{E_2 - E_1}{\hbar} - \omega_p - \frac{|\varepsilon_p|^2}{4\hbar^2}P_2^p - \frac{|\varepsilon_d|^2}{4\hbar^2}P_2^d\right),$$

$$\Delta_{32} = \gamma_{32} + \frac{|\varepsilon_p|^2}{4\hbar^2}\frac{\Gamma_2^p + \Gamma_3^p}{2} + \frac{|\varepsilon_d|^2}{4\hbar^2}\frac{\Gamma_2^d + \Gamma_3^d}{2} +$$
$$+i\left(\frac{E_3 - E_2}{\hbar} - \omega_p + \omega_d - \frac{|\varepsilon_p|^2}{4\hbar^2}\left(P_3^p - P_2^p\right) - \frac{|\varepsilon_d|^2}{4\hbar^2}\left(P_3^d - P_2^d\right)\right),$$

$$\Delta_{31} = \gamma_{31} + \frac{|\varepsilon_p|^2}{4\hbar^2}\frac{\Gamma_3^p}{2} + \frac{|\varepsilon_d|^2}{4\hbar^2}\frac{\Gamma_3^d}{2} + i\left(\frac{E_3 - E_1}{\hbar} - 2\omega_p + \omega_d - \frac{|\varepsilon_p|^2}{4\hbar^2}P_3^p - \frac{|\varepsilon_d|^2}{4\hbar^2}P_3^d\right),$$

including dynamic Stark shifts, transition broadening due to photoionization and phenomenological coherence decay rates γ_{ml}. We also introduce Raman Fano parameters $q^{(1)} = 2\Pi_{32}^p/G_{32}^p$ and $q^{(2)} = 2\Pi_{23}^d/G_{23}^d$ and assume that both $q^{(1)}$ and $q^{(2)}$ are real. In the vicinity of the two-photon resonance, $E_2 + \hbar\omega_p = E_3 + \hbar\omega_d$, they are approximately equal $q^1 \approx q^2 \approx q$ because of $\Pi_{32}^p \approx \left(\Pi_{23}^d\right)^*$, and $G_{32}^p \approx \left(G_{23}^d\right)^*$. Assuming

the quasi-stationarity condition, so that the duration of laser pulses τ satisfies the condition $\tau\left|\Delta_{21,31,32}\right| \gg 1$, we neglect time derivatives and obtain coherences that adiabatically follow the fields.

The two-photon coherence reads

$$\sigma_{32}=i\frac{\varepsilon_p\varepsilon_d^*}{4\hbar^2}\frac{G_{32}^p}{2}\left(\frac{\left|\Omega_p\right|^2(\rho_{11}-\rho_{22})(q+i)}{\Delta_{32}(\Delta_{21}\Delta_{31}+\frac{\left|\varepsilon_p\right|^2\left|\varepsilon_d\right|^2}{(4\hbar^2)^2}\frac{G_{32}^pG_{23}^d}{4}(q+i)^2)+\Delta_{21}\left|\Omega_p\right|^2}+\right.$$

$$\left.+\frac{(\rho_{22}(q+i)-\rho_{33}(q-i))(\Delta_{21}\Delta_{31}+\frac{\left|\varepsilon_p\right|^2\left|\varepsilon_d\right|^2}{(4\hbar^2)^2}\frac{G_{32}^pG_{23}^d}{4}(q+i)^2)}{\Delta_{32}(\Delta_{21}\Delta_{31}+\frac{\left|\varepsilon_p\right|^2\left|\varepsilon_d\right|^2}{(4\hbar^2)^2}\frac{G_{32}^pG_{23}^d}{4}(q+i)^2)+\Delta_{21}\left|\Omega_p\right|^2}\right). \tag{4.30}$$

In the limit of strong driving field ($\left|\varepsilon_d\right|^2 \gg \left|\varepsilon_p\right|^2$) Eq.(4.30) reduces to

$$\sigma_{32}=i\frac{\varepsilon_p\varepsilon_d^*}{4\hbar^2}\frac{G_{32}^p}{2}\frac{\rho_{22}(q+i)-\rho_{33}(q-i)}{i\Delta+\frac{\left|\varepsilon_d\right|^2}{4\hbar^2}\frac{\Gamma_2^d+\Gamma_3^d}{2}+\gamma_{32}}, \tag{4.31}$$

and

$$\sigma_{21}=\frac{i\Omega_p}{\Delta_{21}}(\rho_{11}-\rho_{22})=\frac{i\Omega_p(\rho_{11}-\rho_{22})}{iD+\frac{\left|\varepsilon_d\right|^2}{4\hbar^2}\frac{\Gamma_2^d}{2}+\gamma_{21}}, \tag{4.32}$$

where

$$\Delta=\frac{E_3-E_2}{\hbar}-\omega_p+\omega_d-\frac{\left|\varepsilon_d\right|^2}{4\hbar^2}\left(P_3^d-P_2^d\right),$$

$$D=\frac{E_2-E_1}{\hbar}-\omega_p-\frac{\left|\varepsilon_d\right|^2}{4\hbar^2}P_2^d.$$

We can now plug these expressions into the propagation equation for the probe field:

$$\frac{\partial\varepsilon_p}{\partial z}+\frac{n_p}{c}\frac{\partial\varepsilon_p}{\partial t}=\frac{4\pi i\omega_p}{cn_p}P,$$

with polarization of the medium at the probe field frequency given by:

$$P=N\left(\sigma_{21}\mu_{12}+\rho_{22}\frac{\varepsilon_p}{2\hbar}(P_2^p+i\Gamma_2^p/2)+\rho_{33}\frac{\varepsilon_p}{2\hbar}(P_3^p+i\Gamma_3^p/2)+\sigma_{32}\frac{\varepsilon_d}{2\hbar}(\Pi_{23}^d+iG_{23}^d/2)\right).$$

Here n_p is the non-resonant refractive index of the medium at the probe frequency.

The population of state 3 is negligible if the driving field is strong (EIT regime), so that the polarization response P reads

$$P = i\frac{\varepsilon_p N}{2\hbar}\left(\frac{|\mu_{21}|^2(\rho_{11}-\rho_{22})}{iD+\frac{|\varepsilon_d|^2}{4\hbar^2}\frac{\Gamma_2^d}{2}+\gamma_{21}}+\right.$$

$$\left.+\rho_{22}(-iP_2^p+\Gamma_2^p/2)+\rho_{22}(q+i)^2\frac{|\varepsilon_d|^2}{4\hbar^2}\frac{G_{32}^pG_{23}^d}{4}\frac{1}{i\Delta+\frac{|\varepsilon_d|^2}{4\hbar^2}\frac{\Gamma_2^d+\Gamma_3^d}{2}+\gamma_{32}}\right).$$

Now we can analyze the imaginary part of the polarization, which determines amplification at the probe wavelength:

$$Im(P) = -\frac{\varepsilon_p N}{2\hbar}\left[(\rho_{22}-\rho_{11})\frac{|\mu_{12}|^2\left(\frac{|\varepsilon_d|^2}{4\hbar^2}\frac{\Gamma_2^d}{2}+\gamma_{21}\right)}{D^2+\left(\frac{|\varepsilon_d|^2}{4\hbar^2}\frac{\Gamma_2^d}{2}+\gamma_{21}\right)^2}-\rho_{22}\frac{\Gamma_2^p}{2}-\right.$$

$$\left.\rho_{22}\frac{|\varepsilon_d|^2}{4\hbar^2}\frac{\Gamma_3^d\Gamma_2^p}{4}\frac{(q^2-1)\left(\frac{|\varepsilon_d|^2}{4\hbar^2}\frac{\Gamma_2^d+\Gamma_3^d}{2}+\gamma_{32}\right)+2q\Delta}{\Delta^2+\left(\frac{|\varepsilon_d|^2}{4\hbar^2}\frac{\Gamma_2^d+\Gamma_3^d}{2}+\gamma_{32}\right)^2}\right]. \tag{4.33}$$

Similar to Eq.(4.6) the first term in the above expression describes amplification due to population inversion at the operating transition. The second term, proportional to the population of the emitting excited state and to the rate of absorption of the probe field into the continuum, describes ESA. The third term, which is responsible for ESA suppression, is a consequence of the two-photon coherence σ_{32} built up by the driving and probe fields and due to EIT.

Introducing a dimensionless two-photon detuning

$$x = \frac{\Delta}{\frac{|\varepsilon_d|^2}{4\hbar^2}\frac{\Gamma_2^d+\Gamma_3^d}{2}+\gamma_{32}}$$

we can rewrite Eq.(4.33) as:

$$Im(P) = -\frac{\varepsilon_p N}{2\hbar}\left[(\rho_{22}-\rho_{11})\frac{|\mu_{21}|^2\left(\frac{|\varepsilon_d|^2}{4\hbar^2}\frac{\Gamma_2^d}{2}+\gamma_{21}\right)}{D^2+\left(\frac{|\varepsilon_d|^2}{4\hbar^2}\frac{\Gamma_2^d}{2}+\gamma_{21}\right)^2}-\rho_{22}\frac{\Gamma_2^p}{2}\times\right.$$

$$\times \left\{ \frac{\frac{|\varepsilon_d|^2}{4\hbar^2}\frac{\Gamma_3^d}{2}}{\frac{|\varepsilon_d|^2}{4\hbar^2}\frac{\Gamma_2^d+\Gamma_3^d}{2}+\gamma_{32}} \frac{(x+q)^2}{x^2+1} + \frac{\frac{|\varepsilon_d|^2}{4\hbar^2}\frac{\Gamma_2^d}{2}+\gamma_{32}}{\frac{|\varepsilon_d|^2}{4\hbar^2}\frac{\Gamma_2^d+\Gamma_3^d}{2}+\gamma_{32}} \right\} \Bigg]. \tag{4.34}$$

Here one immediately identifies the first term in large figure brackets proportional to $\propto (x+q)^2/(x^2+1)$ as an asymmetric Fano resonance factor [10], responsible for suppression of probe field absorption in the vicinity of a LICS. This absorption is completely cancelled at the two-photon detuning $x=-q$. Once it is set to zero, only the second term is left, describing residual excited-state absorption due to decoherence at the Raman transition $3 \leftrightarrow 2$. The decoherence rate has two contributions: 1) intrinsic coherence decay rate of the Raman transition γ_{32} and 2) power broadening $\left(|\varepsilon_d|^2 \big/ 4\hbar^2\right)\Gamma_{3,2}^d/2$ due to absorption of the driving field from level 2. If the power broadening is small compared to the intrinsic decay rate (or the driving field intensity is much less than the EIT threshold, which is the same): $\left(|\varepsilon_d|^2/4\hbar^2\right)\Gamma_{3,2}^d/2 \ll \gamma_{32}$, than there is no ESA suppression present. But if the intensity greatly exceeds the threshold ($\left(|\varepsilon_d|^2/4\hbar^2\right)\Gamma_{3,2}^d/2 \to \infty$), then the gain factor

$$Im(P) = -\frac{\varepsilon_p N}{2\hbar}\left[(\rho_{22}-\rho_{11})\frac{|\mu_{21}|^2\left(\frac{|\varepsilon_d|^2}{4\hbar^2}\frac{\Gamma_2^d}{2}+\gamma_{21}\right)}{D^2+\left(\frac{|\varepsilon_d|^2}{4\hbar^2}\frac{\Gamma_2^d}{2}+\gamma_{21}\right)^2} - \rho_{22}\frac{\Gamma_2^p}{2}\frac{\Gamma_2^d}{\Gamma_2^d+\Gamma_3^d}\right] \tag{4.35}$$

demonstrates ESA suppression (the second term in Eq.(4.35)) by a factor of $\Gamma_2^d/(\Gamma_2^d+\Gamma_3^d)$. Note that strong suppression requires $\Gamma_3^d \gg \Gamma_2^d$.

In the most favorable situation when the driving field is not absorbed from state 2, i.e. when $\Gamma_2^d=0$, according to Eq.(4.34) ESA is suppressed by a factor of $\gamma_{32}/\frac{|\varepsilon_d|^2}{4\hbar^2}\frac{\Gamma_3^d}{2}$, which is much less than unity in the EIT regime.

If the driving field is absorbed from state 2, a condition can be derived for lasing to be possible. Neglecting all losses of the probe field except for those due to ESA

and assuming the most favorable case $\rho_{11} = 0$, one finds that in order to achieve amplification the expression in square brackets in Eq.(4.35) has to be positive, being equivalent to:

$$\sigma_{SE} > \sigma_{ESA}\frac{\Gamma_2^d}{\Gamma_2^d + \Gamma_3^d}\left(1 + \frac{|\varepsilon_d|^2}{4\hbar^2}\frac{\Gamma_2^d}{2}/\gamma_{21}\right). \tag{4.36}$$

The temporal amplification coefficient is then given by the expression:

$$\alpha_{gain} = \frac{cN}{n_p^2}\left(\frac{\sigma_{SE}}{1 + \frac{|\varepsilon_d|^2}{4\hbar^2}\frac{\Gamma_2^d}{2}/\gamma_{21}} - \sigma_{ESA}\frac{\Gamma_2^d}{\Gamma_2^d + \Gamma_3^d}\right). \tag{4.37}$$

Even if it is positive, there has to be enough time for generation to develop before the upper operating state is depleted by ionization due to ESA of the driving field. In other words, in order for laser oscillation to build up gain has to exceed the rate at which population is pumped out of state 2 into the continuum:

$$\alpha_{gain} > \frac{|\varepsilon_d|^2}{4\hbar^2}\frac{\Gamma_2^d}{2}.$$

It yields the following requirement for the inversion density:

$$N > \frac{n_p^2 \frac{|\varepsilon_d|^2}{2\hbar^2}\frac{\Gamma_2^d}{2}}{c\left(\sigma_{SE}/(1 + \frac{|\varepsilon_d|^2}{4\hbar^2}\frac{\Gamma_2^d}{2}/\gamma_{21}) - \sigma_{ESA}\frac{\Gamma_2^d}{\Gamma_2^d+\Gamma_3^d}\right)}. \tag{4.38}$$

This requirement is a consequence of the fact that the temporal gain is proportional to the density of inverted atoms while the photoionization rate is independent of density and is determined only by the driving field intensity and photoionization efficiency. Thus, the higher the density the more likely laser generation is to develop before the inversion is pumped out by the driving field.

B. Discussion

In the present section we discuss how the proposed method of ESA reduction can be applied to realize UV lasing in rare-earth ion doped crystals. Typically in these

materials ESA transitions terminate in the CB of a host, so we mostly focus on this situation.

Let us turn to estimates for required driving field intensities for typical parameters of rare-earths, assuming that the driving field does not cause photoionization from level 2.

In the previous section it was shown that ESA is suppressed if the driving field intensity exceeds a threshold value, necessary for EIT to be established:

$$\frac{|\varepsilon_d|^2}{4\hbar^2}\frac{\Gamma_3^d}{2} \gg \gamma_{32}. \tag{4.39}$$

The ionization rate Γ_3^d for the driving field from level 3 can be expressed in terms of ionization cross-section as $\sigma_3^d = 2\pi\omega_d\Gamma_3^d/\hbar c$, while the field amplitude can be written as $|\varepsilon_d|^2 = 8\pi I^d/c$ in terms of intensity. The condition (4.39) can then be rewritten as

$$\frac{I^d\sigma_3^d\lambda_d}{4\pi\hbar c} \gg \gamma_{32},$$

leading to the threshold intensity

$$I^d \gg I_{th}^d = \gamma_{32}\frac{4\pi\hbar c}{\sigma_3^d\lambda_d} = \gamma_{32}\frac{2\hbar\omega_d}{\sigma_3^d}. \tag{4.40}$$

The physical meaning of the condition (4.40) is that the driving field intensity should be greater than the threshold corresponding to at least one or two photons per the ESA cross-section for the driving field during the decay time of the two-photon coherence σ_{32}. As follows from Eq.(4.40), the threshold intensity is proportional to the Raman transition coherence decay rate γ_{32} (here γ_{32} has actually to be replaced by an inhomogeneous width W_{32}^{inh}) and inversely proportional to the driving field wavelength and ionization cross-section from level 3. Thus, to achieve a lower threshold intensity a Raman transition width as narrow as possible, a driving field wavelength as long as possible, and an ionization cross-section from state 3 into the CB as large

as possible are required.

We consider two different configurations when level 2 is either of $4f^n$ or $4f^{n-1}5d$ type. In the first case the operating laser transition $2 \leftrightarrow 1$ is of intraconfigurational $4f^n \leftrightarrow 4f^n$, while in the latter case it is of interconfigurational $4f^{n-1}5d \leftrightarrow 4f^n$ type. The auxiliary level 3 should be of the same type as the upper operating level 2, so that the driving field can couple it to the same continuum as to which level 2 is coupled by the probe field. In other words, this is the requirement for existence of a Λ-system which involves driving and probe fields, two discrete states 2 and 3, and the same continuum. It means that the Raman transition $2 \leftrightarrow 3$ should be of intraconfigurational $4f^n \leftrightarrow 4f^n$ or $4f^{n-1}5d \leftrightarrow 4f^{n-1}5d$ type.

The widths of $4f^n \leftrightarrow 4f^n$ transitions can vary from tens of MHz [112, 113] in the best case to hundreds of GHz in the worst case. However, in good quality crystals most linewidths of such transitions lie in the range $1 - 10$ GHz. Typical photoionization cross-sections from $4f^n$ states are $\sigma_{ESA} \sim 10^{-18}$ cm^2. Assuming the wavelength of the driving field to lie in the range $\lambda_d \sim 0.3 - 1$ μm, we obtain the following estimate for the threshold intensity:

$$I_{th}^d \sim (1 \div 100)\, \frac{GW}{cm^2}.$$

The situation is more complicated if the emitting state 2 is of $4f^{n-1}5d$ type. The driving field intensity estimate depends on how narrow the transition $2 \leftrightarrow 3$ between the two $4f^{n-1}5d$ states can be made. There is no direct experimental data on these transition widths, so for an estimate we make the rather reasonable assumption that this width is of the same order as a typical linewidth of a $4f^n \leftrightarrow 4f^{n-1}5d$ transition. We should stress that this is the upper limit for the $4f^{n-1}5d \leftrightarrow 4f^{n-1}5d$ linewidth; it actually might be narrower. It is known that at room temperature $4f^{n-1}5d \rightarrow 4f^n$ emission and absorption form wide bands with a total bandwidth of

several tens or even hundreds of nm. However, this width originates from phonon sidebands of absorption/emission spectra. The lifetime of phonon states is very short (typically, in the picosecond range) compared to the metastable laser state lifetime; thus, the states with excited phonons cannot give rise to ESA. Where ESA trully originates is the pure electronic excited state of a dopant. The widths of these states can be very narrow compared to the total bandwidth of a transition. This fact is confirmed by low-temperature absorption and fluorescence measurements in crystals doped with rare-earths, where pure electronic transitions (so called zero phonon line (ZPL)) widths as narrow as 1 cm^{-1} and even smaller were observed. For example, in cerium-doped CaF_2 crystal the width of the ZPL was found to be 0.64 cm^{-1} at low temperature (6 K) [114]. A ZPL of the same width (1.6 cm^{-1}) was observed for the $4f^{13}5d \leftrightarrow 4f^{14}$ transition in Yb^{2+} doped into MgF_2 [104]. Generally, at low temperatures linewidths of the order of $10 - 100$ GHz can be obtained. Taking into account the fact that photoionization cross-sections from $4f^{n-1}5d$ states in lantanides are $\sigma_{ESA} \sim 10^{-17} - 10^{-18}$ cm^2 and assuming the same driving field wavelength range as in the above estimate, we arrive at approximately the same value for the driving field intensity as in the case of an intraconfigurational operating transition:

$$I_{th}^{d} \sim (10 \div 100)\,\frac{GW}{cm^2}.$$

However, data about ZPL widths of interconfigurational transitions are scarce, so in each particular case the possibility of reducing ESA from a $4f^{n-1}5d$ state should be carefully studied experimentally.

Such intensities are achievable in a pulsed regime. For example, for a 1 ns pulse, focused to a spot of 100 μm diameter, required energies of the driving laser pulse are $0.1 - 10$ mJ. It is necessary though that this intensity be smaller than the damage threshold intensity of a crystal.

The distinction between inter- and intraconfigurational operating transitions is crucial with respect to potential laser tunability. Typically, for $4f^n \leftrightarrow 4f^n$ transitions phonon sidebands in both emission and absorption are very weak, so that laser action can be realized only at a fixed frequency. Tunability in this case is restricted by the width of the electronic transition and cannot go beyond $\sim$ 10 GHz. On the other hand, for $4f^{n-1}5d \leftrightarrow 4f^n$ transitions phonon-assisted emission, red-shifted with respect to the ZPL, can be very broad (tens of nanometers). By applying a driving field of a certain frequency, one can reduce ESA losses for some particular wavelength within the phonon sideband of $4f^{n-1}5d \leftrightarrow 4f^n$ fluorescence. Thus, the desired laser wavelength can be chosen by tuning the frequency of the driving field.

As an example we consider a Pr^{3+}:$LiLuF_4$ crystal, which is a promising material for a UV laser [100, 115], since $4f5d$ states of Pr^{3+} ion can be efficiently populated by two-step upconversion pumping via intermediate metastable $4f^2$ levels. This pumping scheme helps to avoid color center formation due to ESA of UV pump photons into the CB. There was an attempt to achieve amplification on $4f5d(1) \rightarrow {}^3H_4$ transition at $\lambda = 255$ nm [116] under such upconversion pumping, but instead of gain 65% absorption of the probe beam was detected. As the authors point out, it was not successful due to ESA of probe photons from the $4f5d(1)$ emitting state into the CB. This problem can be overcome by the method, proposed in the project. Namely, an additional driving laser beam can be applied at another $4f5d \rightarrow CB$ transition in the way shown in Fig.26.

Room temperature emission from the lowest $4f5d(1)$ state occurs between 220 and 280 nm ($35710 - 45450$ cm^{-1}), and the transition to ${}^3H_4$ level has a wavelength of 222 nm [117]. The emitted photons are therefore absorbed in the CB at a wavenumber range of $\sim (82000 - 92000)$ cm^{-1}. The third $4f5d(3)$ band in the excitation spectrum is at ~ 62000 cm^{-1} (161 nm) and the driving field can be applied to the $4f5d(3) \rightarrow$

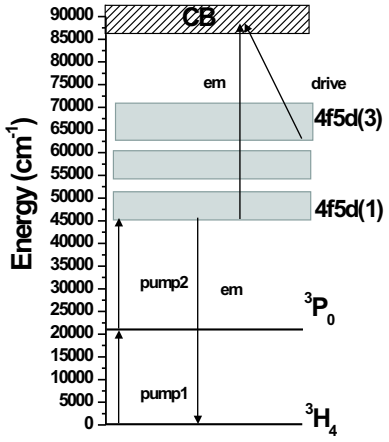

Fig. 26. Energy level scheme of Pr^{3+} ion in $LiLuF_4$.

CB transition. The required wavelength of the driving field is in the range $500 - 330$ nm, which corresponds to the difference in energy $20000 - 30000$ cm^{-1} between $4f5d(3)$ and the terminal state of ESA. If a two-step pumping scheme is used via the $^3P_0$ intermediate level, the second step pump field can simultaneously serve as the driving field, since pumping into $4f5d(1)$ from $^3P_0$ requires wavelengths in the range $330 - 400$ nm. By tuning the pump (and, simultaneously, driving) field, UV gain in the wavelength range of $220 - 240$ nm can be expected. A driving field of the wavelength $330 - 400$ nm will not be absorbed from the ground $^3H_4$ state and it will be only weakly absorbed from the emitting $4f5d(1)$ state into the high-energy edge of the $4f5d(3)$ band at $70000 - 75000$ cm^{-1} due to the parity-forbidden character of $5d \leftrightarrow 5d$ transitions. The intensity of the drive field, required to establish EIT and suppress ESA, given by Eq.(4.40), cannot be estimated because the decay rate of $4f5d(1) \leftrightarrow 4f5d(3)$ coherence is not known. Zero-phonon lines were observed in Pr^{3+}:$LiYF_4$ at low temperature (8 K) only for the first $4f5d(1)$ band [118], so it is not clear what is the rate of coherence decay between the two $4f5d$ states, connected

by driving and probe fields. In Pr^{3+}:$LiYF_4$ it was found that the ESA cross-section from the first $4f5d(1)$ band into the CB is comparable with the emission cross-section ($\sigma_{EM} = (2.0 \pm 0.2) \times 10^{-18}$ cm^2, $\sigma_{ESA} = (2.6 \pm 0.5) \times 10^{-18}$ cm^2 at room temperature) [105], so ESA needs to be suppressed only by a small amount in order to achieve positive gain.

ESA to the CB becomes important when the frequency of generated light is larger than $\omega_{BG}/2$, where ω_{BG} is the frequency of the onset of absorption from the ground state of an ion into the CB. It is certainly feasible to make the generated frequency as close as possible to ω_{BG}. However, it requires shorter wavelegths of the driving field. The requirement that the driving field is not absorbed from the emitting level into the CB means that $\omega_d < \omega_{BG} - \omega_{EM}$. On the other hand, the driving field frequency obviously satisfies the condition $\omega_d > 2\omega_{EM} - \omega_{BG}$, which is the consequence of the fact that state 3 lies in the bandgap of the crystal. These two conditions set a limit on the generated wavelength of a solid-state laser with suppressed ESA:

$$\omega_{EM} < 2\omega_{BG}/3 \tag{4.41}$$

In wide bandgap fluoride crystals, such as $LiYF_4$, $LiLuF_4$, YF_3, and LaF_3, the energy difference between the ground state of a dopant ion and the CB does not exceed ~ 80000 cm^{-1}; then, according to Eq.(4.41), the generated field wavelength is limited from below by $\lambda_{EM} > 190$ nm.

Apart from the discussion on rare-earth ion doped materials as potential candidates for solid-state UV lasing, we would like to mention that the same technique of ESA reduction can be implemented to realize visible and infrared lasing in crystals doped with transition metal ions. Of course, many laser crystals for this range already exist, but far more crystals do not lase due to ESA into either a charge transfer band or into a higher-lying electronic state. Examples of crystals in which the proposed

technique can be helpful to achieve lasing, are V^{3+}:$LiAlO_2$, $LiGaO_2$ (luminescence at $1400-1800$ nm) [119], Cr^{4+}:$LiAlO_2$, $LiGaO_2$ (luminescence at $1200-1600$ nm) [120], Ni^{2+}:$MgAl_2O_4$ (luminescence at $1100-1300$ nm) [121], and some others. For these materials the driving field wavelength lies in the visible or near infrared range.

As an example of how the ESA suppression technique can be applied in the visible region we consider a Ti^{3+}:$YAlO_3$ crystal (Ti:YAP). This crystal has as good mechanical and thermal characteristics as the well-known Ti^{3+}:Al_2O_3 (Ti:Sapphire) laser crystal. Its emission band extends from 540 nm to 800 nm with the maximum at 610 nm, thus it covers the whole range of frequencies where dye lasers are used. So this crystal can be a solid-state equivalent for dye lasers. Having so promising characteristics, this crystal is not an efficient laser material since laser action is difficult to obtain [122]. The problem with this crystal is ESA at a pump wavelength [123]. The ground-state absorption band of Ti:YAP extends from 400 nm up to 550 nm and ESA affects the range of frequencies $350-550$ nm with the ESA cross-section being about two orders of magnitude larger than the ground-state absorption one [123, 124]. For this crystal ESA suppression at the pump wavelength can be realized using the scheme of Fig.27. Doubly degenerate ground and excited states (Kramers doublets) of the lasing transition can be split by an external magnetic field. Varying the magnetic field amplitude the splitting is scanned across the two-photon resonance with the pump laser adjacent modes. At the point of the two-photon resonance ESA of the pump is supposed to be suppressed while ground-state absorption, responsible for creation of inversion, will not be affected, since the splitting in the ground state is different from that in the excited state and does not satisfy the two-photon resonance condition with the pump modes. In this configuration the coherent pump beam will not be absorbed from the populated excited electronic state and at the same time will produce inversion.

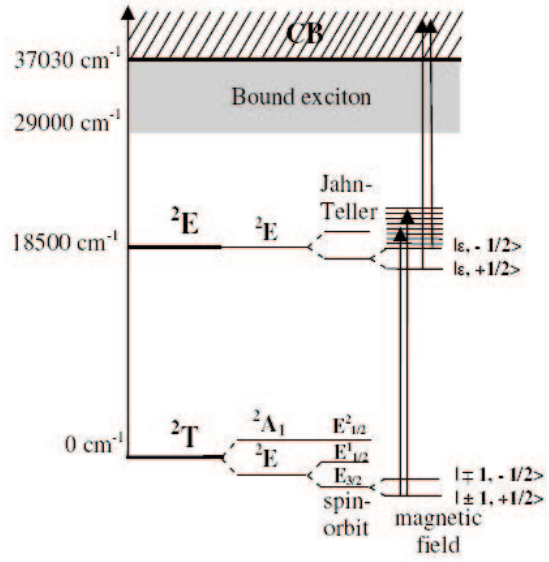

Fig. 27. Energy level diagram of Ti^{3+}:$YAlO_3$ including crystal field, spin-orbit interactions and Jahn-Teller effect. Arrows indicate a multimode coherent pump, and the scheme of its excited-state absorption suppression.

C. Nonlinear regime of short probe pulse propagation in a resonant amplifier with excited-state absorption

Estimates of the control field intensity, necessary for efficient ESA suppression, made for rare-earth ion activated crystals, show that required intensities are rather high (of the order of $10 - 100$ GW/cm^2) and obviously confine this technique to a pulsed regime, in which crystals can sustain such high peak intensity if the pulse duration is within the subnanosecond range [125]. It is necessary therefore to investigate how the method works in a pulsed regime. To that end, a theoretical and numerical analysis of dynamics of propagation and amplification of a probe pulse in a resonant amplifier with ESA is carried out in two different cases. First we analyze a two-level amplifying medium with ESA when the ESA cross-section σ_{ESA} is less than the stimulated emission cross-section σ_{SE} so that amplification is not inhibited. A

solitary probe wave of a dissipative soliton type forms in this case resembling the π-pulse encountered in resonant amplifiers with linear losses [126]. In the second part of the section we consider the case with the reversed relation between the cross-sections when either a cw or pulsed control field is applied to suppress ESA. A solitary wave solution, which forms in the case of a cw control field, is a pair of complimentary pulses similar to adiabatons [127] and at the same time bears similarity with the π-pulse in the sense that the area of the pulse is close to π and the asymmetric shape of the pulse is determined by the medium parameters rather than by initial conditions. At the same time, the solitary wave velocity and amplitude are governed by the initial amplitude of the control field.

1. Two-level amplifier with ESA

Consider a two-level amplifying medium with ESA into the higher-lying one-dimensional structureless continuum (see Fig.22b), by which CB states of a crystal are modelled. In this subsection we study the case when the ESA cross section is less than the stimulated emission one so that ESA does not prevent amplification. A probe field is described by a plane electromagnetic wave $E = (\varepsilon_p/2)e^{-i\omega_p t+ik_p z} + c.c.$, which is resonant to the initially inverted transition $2 \leftrightarrow 1$. It is well-known [126] that in an amplifier with linear non-resonant losses a steady-state solution exists of a form of a hyperbolic-secant π pulse traveling with the speed of light. In our system losses are nonlinear, depending on the population of the state 2, and thus a steady-state wave differs from the π pulse. As will be shown below, its area is less than π and it propagates with a velocity smaller than c.

Dynamic equations for the amplitude σ_{21} of the non-diagonal density matrix element $\rho_{21} = \sigma_{21}e^{-i\omega_p t+ik_p z}$ and populations ρ_{11}, ρ_{22} of discrete levels after adiabatic

elimination of continuum states read as [108]

$$\frac{\partial \sigma_{21}}{\partial t} = -\sigma_{21}\Delta_{21} + i\Omega_p(\rho_{11} - \rho_{22}), \tag{4.42}$$

$$\frac{\partial \rho_{11}}{\partial t} = i\sigma_{21}\Omega_p^* - i\sigma_{21}^*\Omega_p - \rho_{11}\Delta_{11}, \tag{4.43}$$

$$\frac{\partial \rho_{22}}{\partial t} = i\sigma_{21}^*\Omega_p - i\sigma_{21}\Omega_p^* - \rho_{22}\Delta_{22}. \tag{4.44}$$

The slowly varying amplitude of the wave electric field component is goverened by the wave equation:

$$\frac{n_p}{c}\frac{\partial \varepsilon_p}{\partial t} + \frac{\partial \varepsilon_p}{\partial z} = \frac{4\pi i N\omega_p}{cn_p}\left(\mu_{12}\sigma_{21} + \rho_{22}\frac{\varepsilon_p}{2\hbar}(P_2^p + i\Gamma_2^p/2)\right). \tag{4.45}$$

In the above expressions μ_{21} is the dipole moment matrix element of the $2 \leftrightarrow 1$ transition, and n_p is the refractive index of the host medium at the probe field frequaency. We also introduced the Rabi frequency of the field $\Omega_p = \mu_{21}\varepsilon_p/2\hbar$ and complex dressed decay rates:

$$\Delta_{21} = \frac{|\varepsilon_p|^2}{4\hbar^2}\frac{\Gamma_2^p}{2} + i\left(\omega_{21} - \omega_p - \frac{|\varepsilon_p|^2}{4\hbar^2}P_2^p\right) + \gamma_{21},$$

$$\Delta_{11} = \Gamma_1,$$

$$\Delta_{22} = \frac{|\varepsilon_p|^2}{4\hbar^2}\Gamma_2^p + \Gamma_2,$$

where ω_{21} is the amplifying transition frequency; γ_{21}, $\Gamma_{1,2}$ are the coherence and the population decay rates due to processes other that ESA (inhomogeneous broadening is neglected) and P_2^p and $\Gamma_2^p/2$ are real and imaginary parts of the following integral:

$$P_2^p + i\Gamma_2^p/2 = \lim_{\eta\to+0}\int \frac{|\mu_{c2}|^2\, dE_c}{(E_c - E_2)/\hbar - \omega_p - i\eta} = \tag{4.46}$$

$$= P\int \frac{|\mu_{c2}|^2\, dE_c}{(E_c - E_2)/\hbar - \omega_p} + i\pi\hbar\,|\mu_{c2}|^2_{E_c = E_2 + \hbar\omega_p}\,.$$

Expression (4.46) shows that P_2^p describes the dynamic Stark shift of the upper level energy E_2 due to field induced coupling to the continuum states $|c>$ with energies

E_c; μ_{c2} is the dipole moment of the corresponding transition $|2> \leftrightarrow |c>$, and Γ_2^p is related to the ionization rate from the upper level to the continuum.

In the theoretical analysis we assume for simplicity that $P_2^p = 0$ (flat continuum) and $\omega_p = \omega_{21}$, so that the pulse carrier frequency is in resonance with the central frequency of the amplifying transition. We also restrict ourselves to short pulses, when no coherence as well as population relaxation is taken into account except for the one due to ESA. In the following we will be looking for a shape-invariant wave solution moving with constant velocity V.

Having neglected relaxations, we went over to the zero amplifying transition linewidth limit, which greatly simplifies the analysis. In this limit $\sigma_{21} = -i\sqrt{\rho_{11}\rho_{22}}$ is pure imaginary and ε_p is real. The dynamics of the system can therefore be described in terms of state amplitudes since there is no coherence or population decay not related to the action of the coherent optical field. Thus, we set $\rho_{11} = a_1^2$, $\rho_{22} = a_2^2$ (with $\sigma_{21} = -ia_2a_1$). In a retarded frame the equations for the state and field amplitudes of a steady-state wave solution can be written in the following dimensionless way:

$$\frac{da_1}{d\tau} = ua_2, \tag{4.47}$$

$$\frac{da_2}{d\tau} = -ua_1 - u^2a_2, \tag{4.48}$$

$$\frac{du}{d\tau} = -\alpha^2(a_1a_2 - ua_2^2), \tag{4.49}$$

where retarded frame coordinates $\tau = T - Z/v$, $\xi = Z$ are expressed in terms of the dimensionless time and distance $T = 2\mu_{21}^2 t/\Gamma_2^p$, $Z = 2\mu_{21}^2 z n_p/\Gamma_2^p c$ with $v = Vn_p/c$ being the frame dimensionless velocity and $\frac{\partial}{\partial\xi} = 0$ is set in order to obtain a steady-state solution. Normalized field amplitude is defined as $u = \varepsilon_p\Gamma_2^p/4\hbar\mu_{21}$; $g = 1/v - 1 = c/n_pV - 1$;

$$\nu = \frac{\pi N\omega_p}{\hbar}\frac{(\Gamma_2^p)^2}{2\mu_{21}^2 n_p^2}$$

is an amplification coefficient, and dimensionless parameter α is expressed as $\alpha = \sqrt{\nu/g}$.

This set of equations has an integral

$$u^2/\alpha^2 + a_2^2 + 2a_1^2 = 1, \tag{4.50}$$

which reflects the fact that the energy is conserved, i.e. that the energy initially stored in the inverted medium goes either into the field or into ionization. The form of this integral suggests that the system evolves on a surface of an ellipsoid with axes (a_1,a_2,u). It is natural then to describe the evolution in terms of polar and azimuthal angles introduced on the ellipsoid surface:

$$u = \alpha\cos\Theta,\ a_1 = \frac{1}{\sqrt{2}}\sin\Theta\cos\phi,\ a_2 = \sin\Theta\sin\phi. \tag{4.51}$$

In terms of the angles and the modified time $\tau' = \tau\alpha$ the evolution is governed by the system:

$$\frac{d\Theta}{d\tau'} = \sin\Theta\sin\phi\left(\frac{\cos\phi}{\sqrt{2}} - \alpha\cos\Theta\sin\phi\right), \tag{4.52}$$

$$\frac{d\phi}{d\tau'} = \cos\Theta\left(\cos\phi\left[\frac{\cos\phi}{\sqrt{2}} - \alpha\cos\Theta\sin\phi\right] - \sqrt{2}\right). \tag{4.53}$$

It is convenient to analyze this system using the phase-plane formalism [128]. First of all, it is clear that there is a periodicity in both ϕ and Θ, so that only the range $0 \le \Theta \le \pi$, $-\pi \le \phi \le \pi$ needs to be considered. Let us turn now to stationary points of the system. Three regimes are possible depending on the value of α, describing different dynamics of the system. In the first one $\alpha < 2$, the stationary points are $\Theta = \pi/2$, $\phi = \pi n/2$ with n being an integer. Even values of n correspond to saddles while the odd ones correspond to unstable focuses. The corresponding phase space structure is depicted in Fig.28. There is a separatrix connecting the two stationary points, which escapes from the focus at $\tau' \to -\infty$ and enters the

saddle at $\tau' \to \infty$. Since for both stationary points $\Theta = \pi/2$, the amplitude of the optical field vanishes at $\tau' \to \pm\infty$, which means that the separatrix represents a soliton propagating in the medium. Its amplitude grows and oscillates on the leading edge while the trailing one decays without oscillations. At the leading edge $\rho_{22} = 1$ and $\rho_{11} = 0$, at the trailing edge $\rho_{22} = 0$ and $\rho_{11} = 1/2$. Other trajectories on the plane correspond to front-type stationary waves for which $u^2 \to \alpha^2$ and no population is left in the system as $\tau' \to \infty$, so that the incoming optical wave ionizes the medium completely. These solutions are of the same type as the solitary wave found in Ref.[129] where a two-level system with the upper state replaced by the continuum was considered. The continuum-coupled solutions found here are different in that the leading edge amplitude of the wave oscillates which is possible because of initial population inversion leading to amplification of small fluctuations of the field. The reason the solutions demonstrate oscillatory behavior is that the ionization rate is slow enough so that the system undergoes a number of Rabi flops at the optical transition. The number of oscillations can be estimated by linearizing the set of equations (4.52)-(4.53) in the vicinity of the focus stationary point. The eigenvalues of the corresponding linear set of equations for small deviations from the focus are $\lambda_{\pm}^{f} = \left(\alpha \pm i\sqrt{4-\alpha^2}\right)/2$. They show that smaller α gives more oscillations and, since $v = 1/\left(1+\nu/\alpha^2\right)$, smaller α corresponds to slower velocity of the soliton.

As for the saddle point, the eigenvalues of the linearized set of equations are $\lambda_{\pm}^{s} = \pm 1/\sqrt{2}$ with the corresponding eigenvectors $(\Theta - \pi/2, \phi) \sim (\pm 1, \pm 1)$ and $\sim (\pm 1, \mp 1)$. It results in the following asymptotic behavior of the system as $\tau' \to \infty$: $(1/2 - \rho_{11}) \sim 2\exp\left(-\tau'\sqrt{2}\right)$, $\rho_{22} \sim \exp\left(-\tau'\sqrt{2}\right)$, and $u \sim \alpha\exp\left(-\tau'/\sqrt{2}\right)$.

The situation is more complicated for $\alpha > 2$ because of several additional stationary points (see Fig.29). New saddles at $\Theta = \pi$, $\phi = n\pi + \phi_2$ and at $\Theta = 0$, $\phi = n\pi - \phi_2$ appear accompanied by additional stable nodes corresponding to each

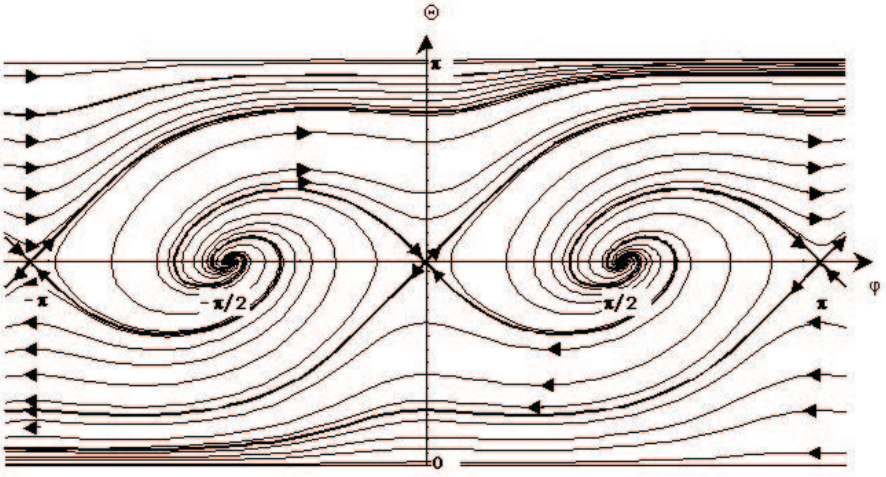

Fig. 28. The phase space spanning solutions of the set of equations (4.52)-(4.53) for $\alpha < 2$ (for this particular plot $\alpha = 0.7$). Trajectories marked bold are separatrixes.

additional saddle: ($\Theta = \pi$, $\phi = n\pi + \phi_1$) and ($\Theta = 0$, $\phi = n\pi - \phi_1$). The angles ϕ_1 and ϕ_2 are given by the expression:

$$\phi_{1,2} = \tan^{-1} \frac{\alpha \mp \sqrt{\alpha^2 - 4}}{2\sqrt{2}}. \tag{4.54}$$

As can be seen from Fig.29 there are no trajectories experiencing oscillatory behavior for $\alpha > 2$. The separatrix connecting the unstable node and saddle points at $\Theta = \pi/2$ represents a soliton as in the case $\alpha < 2$. Its behavior near the saddle point is the same, although the evolution at $\tau' \to -\infty$ as it leaves the node is different. It can be analyzed in the similar way, i.e. by linearizing equations (4.52)-(4.53) in the vicinity of the equilibrium point and subsequent evaluation of the eigenvalues and eigenvectors of the linearized set of equations. The eigenvalues for the node are:

$$\lambda_{\pm} = \frac{\alpha \pm \sqrt{\alpha^2 - 4}}{2}, \tag{4.55}$$

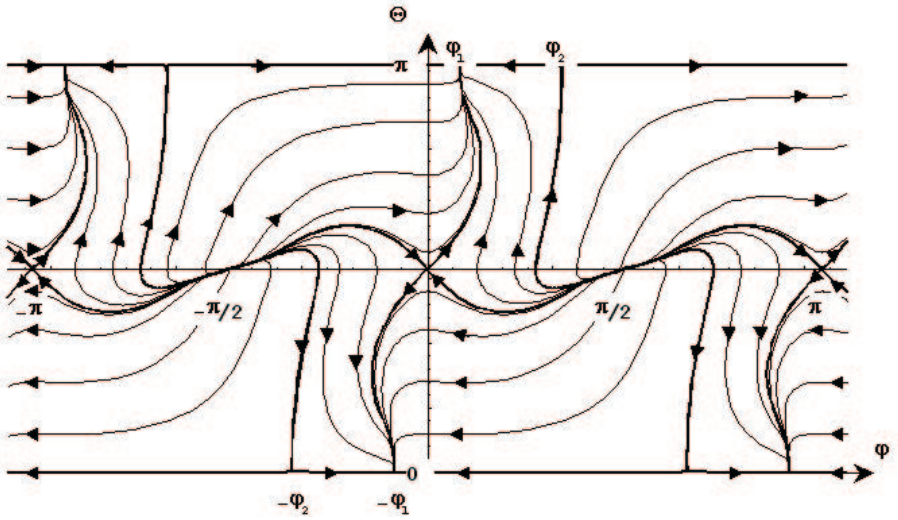

Fig. 29. The phase space structure describing solutions of the set of equations (4.52)-(4.53) in the case $\alpha > 2$ (for this particular plot $\alpha = 3.0$).

with the corresponding eigenvectors

$$(\Theta - \pi/2, \phi - \pi/2) \sim \pm \left(1, \sqrt{2}\lambda_{\mp}\right). \tag{4.56}$$

It is easy to find how populations of the two levels and the optical field intensity behave at the leading edge of the soliton. Substituting the expressions (4.55)-(4.56) into (4.51), one obtains populations and the field intensity for the two eigenmodes:

$$\rho_{11}^{\pm} \to \lambda_{\mp}^2 \exp\left(2\lambda_{\pm}\tau'\right), \tag{4.57}$$

$$\rho_{22}^{\pm} - 1 \to -\left(1 + 2\lambda_{\mp}^2\right) \exp\left(2\lambda_{\pm}\tau'\right), \tag{4.58}$$

$$\left(u^{\pm}\right)^2 \to \alpha^2 \left(2\lambda_{\mp}^2 - 1\right) \exp\left(2\lambda_{\pm}\tau'\right). \tag{4.59}$$

Obviously, the solution corresponding to λ_+ builds up faster than the one corresponding to λ_-, but on the other hand it uses population inversion inefficiently. It is clear that the optical field is amplified only if some population is transferred from level 2 to level 1 and is absorbed only if some population from level 2 goes into the continuum.

For the "$\pm$ "-solutions we obtain the following ratio of the amplification rate to the total depletion rate of the upper-state population:

$$R_{eff}^{\pm} = \frac{\lambda_{\mp}^2}{1 + 2\lambda_{\mp}^2}. \tag{4.60}$$

This ratio reflects the efficiency of usage of initial population inversion in the process of field amplification. The higher the λ is, the more economically the population inversion is being used. Thus, we see that the solution corresponding to the λ_- eigenvalue leads to more efficient amplification of the field compared to the one corresponding to λ_+, since $R_{eff}^{-} > R_{eff}^{+}$. Therefore, "-"-eigenmode corresponds to the soliton while "+"-eigenmode represents a front-type solution, which cannot support itself without continuous external energy supply from the trailing edge of the pulse.

It is evident that without continuous external pumping only the soliton-type solution, corresponding to the separatrix connecting the unstable node and the saddle, can propagate without changing its shape. From the above discussion we also see that on the one hand many solitons corresponding to different α's and, thus, travelling with different velocities can exist. On the other hand, only one can survive in the medium since it uses up initial population inversion completely. The question arises: which particular soliton survives if one starts with arbitrary initial conditions? For the soliton the rate at which it exponentially builds up is λ_-, which is larger for smaller α and, therefore, for slower solitons. On the other hand, from the expression for R_{eff}^{-} we see that the slower the soliton propagates the smaller R_{eff}^{-} is and, consequently, the lower the efficiency of amplification. It means that the growth rate competes with the effectiveness of inversion usage. Numerical simulations show that the soliton corresponding to $\alpha = 2$ is realized, so that the fast growing solution with the smallest velocity survives. The case $\alpha = 2$ corresponds to the bifurcation situation when the two stationary points at $\Theta = \pi,\ \phi = \phi_1$ and $\Theta = \pi,\ \phi = \phi_2$ merge forming a saddle-

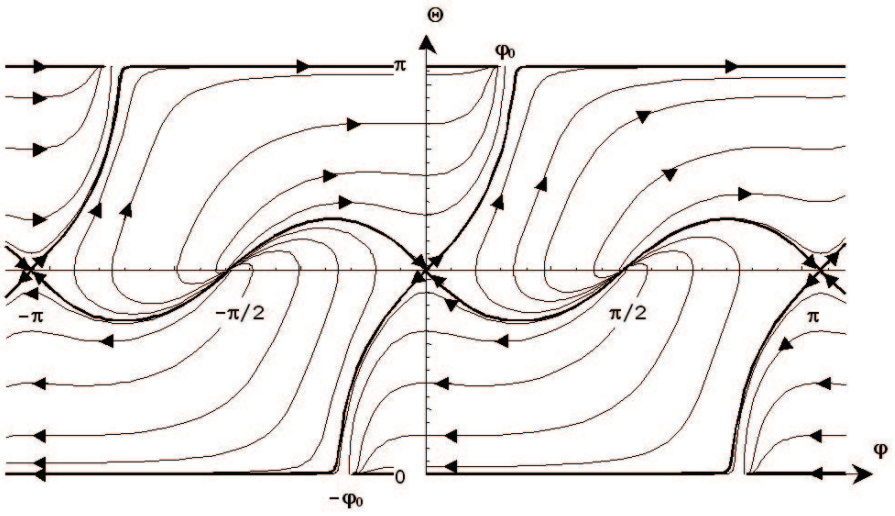

Fig. 30. The phase space structure of the set of equations (4.52)-(4.53) in bifurcation case $\alpha = 2$.

node. The latter behaves as a saddle if approached from one side of the attractive separatrix and as a stable node if approached from another side. At the same time, the unstable focus at $\Theta = \pi/2,\ \phi = \pi/2$ transforms into the unstable node. The corresponding phase diagram is shown in Fig.30.

The soliton moves slower than the speed of light. From the condition $\alpha = \sqrt{\nu/(c/n_p V - 1)} = 2$ the inverse pulse velocity is:

$$\frac{1}{V} = \frac{n_p}{c}\left(1 + \frac{\nu}{4}\right) = \frac{n_p}{c}\left(1 + \frac{\pi N \omega_p}{\hbar n_p^2}\frac{(\Gamma_2^p)^2}{8\mu_{21}^2}\right). \tag{4.61}$$

It is interesting to note that this velocity can be obtained from the well-known expression for the velocity of the 2π pulse in an absorbing medium in the limit when the pulse is shorter than the inhomogeneous broadening time of the transition [126]:

$$\frac{1}{V} = \frac{n_p}{c}\left(1 + \frac{2\pi N \omega_p \mu_{21}^2}{\hbar n_p^2} t_p^2\right), \tag{4.62}$$

where t_p is the pulse width. In our case the pulse width is $\tau_p' \sim 1$ or $t_p \sim \Gamma_2^p/4\mu_{21}^2$.

Substitution of this pulse width into (4.62) gives exactly the velocity of the steady-state pulse Eq.(4.61). The dimensionless pulse intensity, obtained from numerical calculation, is $u^2_{max} \approx 3.06$, the pulse full width at half maximum (FWHM) is $\tau'_p \approx 1.927$, and the pulse area obtained by numerically integrating the separatrix solution over time is given by the following expression (see Fig.32):

$$\Sigma = \int_{-\infty}^{\infty} \frac{\varepsilon_p \mu_{21}}{\hbar} dt = \int_{-\infty}^{\infty} u d\tau' \approx 2.66. \tag{4.63}$$

In Fig.31 results of a numerical solution of Eqs.(4.42)-(4.45) in the retarded frame are shown. The initial pulse of a small amplitude enters the medium at the left boundary $\xi = 0$ at $\tau = 0$. As is seen from Fig.31 for small $\xi's$, the pulse first evolves as the non-stationary π-pulse, its amplitude increases and its width decreases inversely proportionally to the amplitude, and it moves faster than c/n_p. The oscillating tail is also typical of the non-stationary π-pulse. As amplitude grows, the pulse eventually slows down and starts to transform into the steady-state dissipative soliton, described above, whose velocity is less than c/n_p and the area, shown in Fig.32, in the limit $\tau \to \infty$ agrees well with the value 2.66 obtained above by integrating the separatrix solution.

So far, due to a short duration of pulses we consider, we have neglected relaxation processes leading to decay of optical coherence, which is mathematically equivalent to the limit of infinitely narrow amplifying optical transitions. Although this approximation allows one to obtain analytical results, it is interesting to study finite width effects since in real media each electronic transition is broadened. In Fig.33 and Fig.32 the results of numerical solution of Eqs.(4.42)-(4.45), taking into account optical coherence relaxation, are shown. Only the final solution shape is shown to illustrate how it differs from the relaxation-free case. The main differences are: 1) the steady-state wave forms only if $\sigma_{SE} > \sigma_{ESA}$, which is rather obvious, 2) the formation

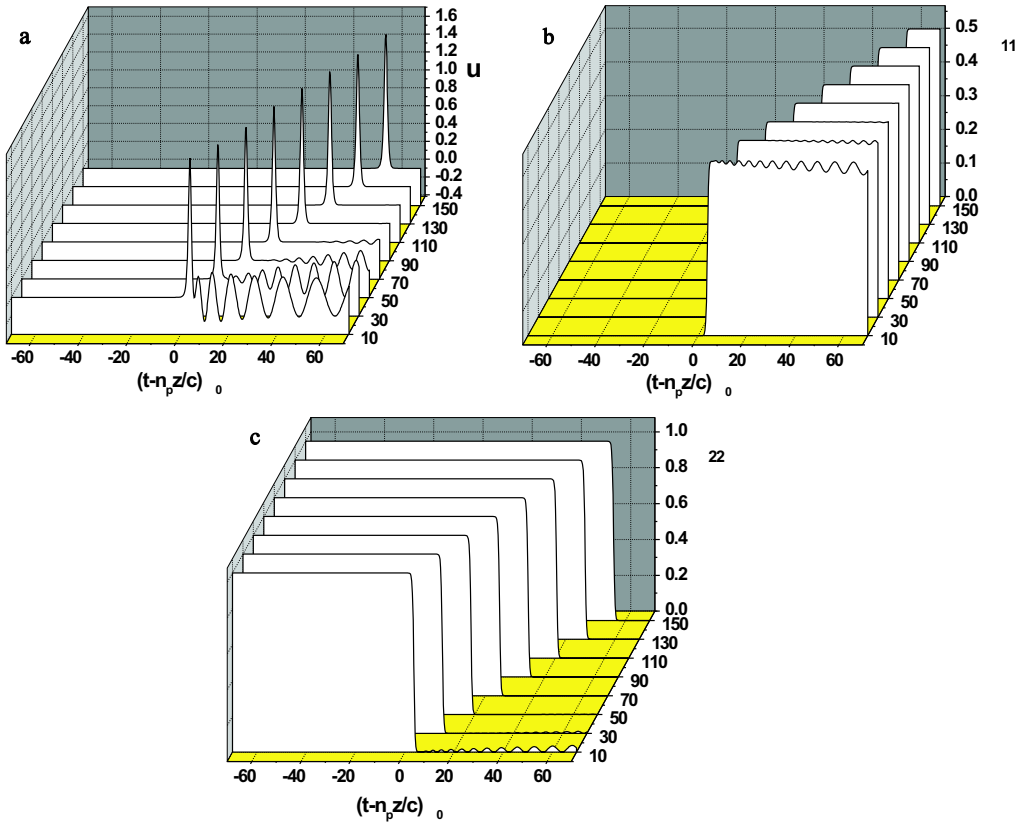

Fig. 31. Numerical solution of the system Eqs.(4.42)-(4.45) in the retarded frame in terms of dimensionless variables u, τ and ξ after various propagation distances: a) $u(\tau,\xi)$; b) $\rho_{11}(\tau,\xi)$; c) $\rho_{22}(\tau,\xi)$; parameter $\Omega_0 = 2\mu_{21}^2/\Gamma_2^p$ defines the pulse width. Initial pulse is Gaussian: $u(\tau,\xi=0) = 0.1\exp\left(-(2.5\tau)^2\right)$. In the calculation all relaxation processes except for ESA were neglected and $P_2^p = 0$, $\nu = 1$ were taken. Here and in subsequent figures the pulse propagates to the left in a laboratory frame.

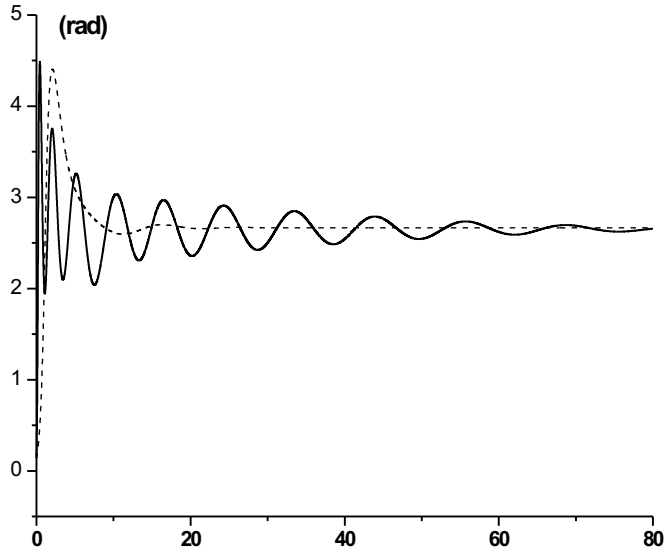

Fig. 32. Numerically calculated area $\Sigma = \int_{-\infty}^{\infty} \frac{\varepsilon_p \mu_{21}}{\hbar} dt$ of the steady-state pulse shown in Fig.31 (solid line) and in Fig.33 (dashed line).

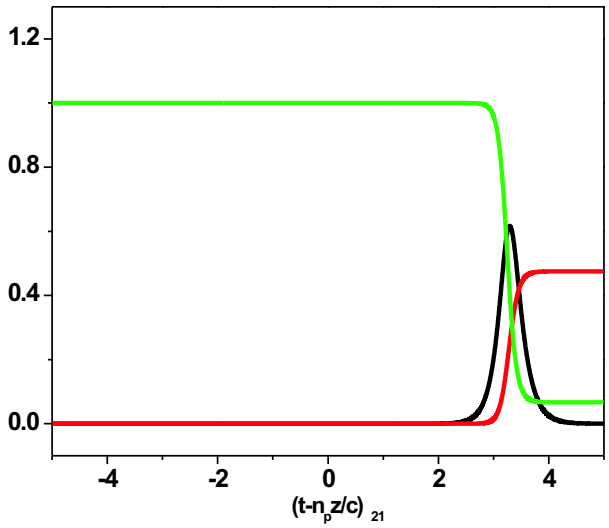

Fig. 33. Numerical solution of the system Eqs.(4.42)-(4.45) in the retarded frame for u (black curve), ρ_{11} (red curve) and ρ_{22} (green curve) in terms of dimensionless parameters τ and $\xi = 320$, taking into account optical coherence relaxation. All parameters are as in Fig.(31) except that $\gamma = \sigma_{SE}/\sigma_{ESA} = 4$ was assumed.

length of the pulse becomes shorter compared to the relaxation-free case, and 3) the population of the excited state ρ_{22} is not depleted completely and $\rho_{11} < 1/2$ in the steady-state regime. The reason is that the coherence "dies" faster than $\sqrt{\rho_{11}\rho_{22}}$, and as soon as the coherence vanishes, the field is no longer generated. So it does not "use" all population of the excited state, some is left when the pulse passes. The corresponding pulse area, given in Fig.32, is the same as in the relaxation-free case.

To simplify our analysis of the system with coherence relaxation we restrict ourselves to the situation in which the linewidth γ_{21} originates from the spontaneous decay of level 1 at a rate $\gamma_{21} = \Gamma_1/2$. This is a rather typical situation in the doped crystals where the amplifying transition terminates in the excited phonon states of

the ground electronic state, the former ones having extremely short lifetime. If no other dephasing mechanisms are present, one can still use state amplitudes as good variables. The set of equations (4.47)-(4.49) modifies as follows:

$$\frac{da_1}{d\tau} = ua_2 - \gamma a_1, \tag{4.64}$$

$$\frac{da_2}{d\tau} = -ua_1 - u^2 a_2, \tag{4.65}$$

$$\frac{du}{d\tau} = -\alpha(a_1 a_2 - u a_2^2). \tag{4.66}$$

Here γ is a normalized decay rate of the lower state population $\gamma = \Gamma_1 \Gamma_2^p / 4\mu_{21}^2$. There is no conservation integral in this case, therefore, one has to work in a 3-dimensional phase space instead of a 2-dimensional one. The stationary point of the set of equations (4.64)-(4.66) corresponding to our initial and final conditions (zero filed) is $u = 0$, $a_1 = 0$, and $a_2 = A$. In the vicinity of the stationary point the linearized version of Eqs.(4.64)-(4.66) includes only equations for a_1 and u since a_2 changes only in the second order. The corresponding two eigenvalues read as

$$\lambda_{\pm} = \frac{1}{2}\left(-\gamma + A^2\alpha^2 \pm \sqrt{(\gamma + A^2\alpha^2)^2 - 4A^2\alpha^2}\right). \tag{4.67}$$

Initial conditions correspond to $A = 1$. The same phase space analysis can be carried out as in the relaxation-free case. In analogy we look for the regime when the stationary point is an unstable node. This happens if $\gamma < \alpha^2$ and $\gamma < 1$, the last inequality being nothing but $\sigma_{SE}/\sigma_{ESA} > 1$, i.e. the standard condition of amplification. Following the same reasoning used in the non-decaying case, one finds that the optimal growth combined with economical usage of initial population inversion is achieved when $\gamma = 2\alpha - \alpha^2$. This condition gives the velocity of the

soliton:

$$V = \frac{c}{n_p\left(1+\frac{\nu}{2-\gamma+2\sqrt{1-\gamma}}\right)}. \tag{4.68}$$

As for population inversion remaining in the medium after the soliton passes through, it can be found by analyzing the expression (4.67) assuming some nonzero A. For $A_0 < A^2 < 1$, where $A_0 = \gamma/\left(2-\gamma+2\sqrt{1-\gamma}\right)$, the corresponding stationary point is an unstable focus (however, it is an unstable node at $A^2 = 1$). The focus becomes stable for $A_0^2 < A^2 < A_0$. Finally, for $A^2 < A_0^2$ the stable focus turnes into a stable node. It can be shown that the optimal combination of amplification efficiency and economicity of population inversion consumption is achieved if $A = A_0$, so that the population left in the upper level is $\rho_{22} = A_0^2 = \gamma^2/(2-\gamma)^2$. These analytical predictions for the pulse amplitude and population dymanics are confirmed by numerical simulations (see Fig.33).

Finally, in Fig.34 results of numerical modelling of the situation, when dispersive properties of the ESA transition are taken account of, are presented. Typically, the dynamic Stark shift due to the resonant interaction with the continuum is of the same order as the ionization rate [130], namely, $P_2^p \sim \Gamma_2^p/2$. This shift leads to the deviation of the phase difference between the field and the optical coherence σ_{21} from $\pi/2$, optimal for amplification. This, in turn, results in smaller amplitude and larger width of the pulse as the simulation results demonstrate.

2. Two-level amplifier with ESA suppresed by an additional control field

In this subsection we consider the case $\sigma_{SE} < \sigma_{ESA}$, when amplification cannot take place unless ESA from the upper level of an amplifying transition is suppressed using an additional control field applied in the way, shown in Fig.25. We analyze the dynamics of amplification and propagation of a probe pulse in the presence of an

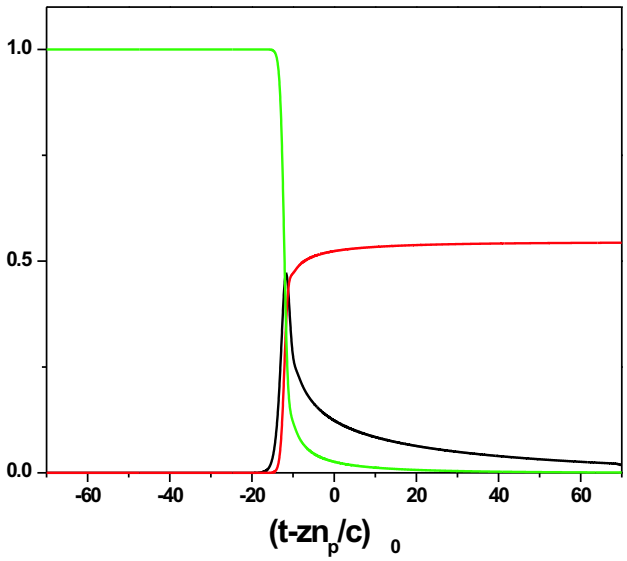

Fig. 34. Numerical solution of the system Eqs.(4.42)-(4.45) in the retarded frame, taking into account dispersion associated with the ESA transition, in terms of dimensionless variables τ, and $\xi = 400$. Field amplitude $|u|$, and populations ρ_{11}, ρ_{22} are shown as black, red and green curves. In the analysis $P_2^p = \Gamma_2^p/2$ was taken, the rest is as in Fig.31.

additional either cw or pulsed control field and study the evolution and interaction of the fields.

The system of dynamic equations for the amplitudes σ_{ml} of density matrix elements ρ_{ml}, determined by the standard expressions: $\sigma_{21} = \rho_{21}e^{-i\omega_p t+ik_p z}$, $\sigma_{32} = \rho_{32}e^{-i(\omega_p-\omega_c)t+i(k_p-k_c)z}$, $\sigma_{31} = \rho_{31}e^{-i(2\omega_p-\omega_c)t+i(2k_p-k_c)z}$, and populations of discrete levels ρ_{11}, ρ_{22} and ρ_{33} after adiabatically eliminating continuum variables is as follows (Ref.[108]):

$$\frac{\partial\sigma_{21}}{\partial t} = -\sigma_{21}\Delta_{21} + i\Omega_p(\rho_{11}-\rho_{22}) + i\frac{\varepsilon_p^*\varepsilon_c}{4\hbar^2}\sigma_{31}\left(\Pi_{23}^c + iG_{23}^c/2\right), \tag{4.69}$$

$$\frac{\partial\sigma_{32}}{\partial t} = -\sigma_{32}\Delta_{32} - i\Omega_p^*\sigma_{31} + i\frac{\varepsilon_p\varepsilon_c^*}{4\hbar^2}\left(\rho_{22}\left(\Pi_{32}^p + iG_{32}^p/2\right) - \rho_{33}\left(\left(\Pi_{23}^c\right)^* - i\left(G_{23}^c\right)^*/2\right)\right), \tag{4.70}$$

$$\frac{\partial\sigma_{31}}{\partial t} = -\sigma_{31}\Delta_{31} - i\Omega_p\sigma_{32} + i\frac{\varepsilon_p\varepsilon_c^*}{4\hbar^2}\sigma_{21}\left(\Pi_{32}^p + iG_{32}^p/2\right), \tag{4.71}$$

$$\frac{\partial\rho_{11}}{\partial t} = i\sigma_{21}\Omega_p^* - i\sigma_{21}^*\Omega_p - \Delta_{11}\rho_{11}, \tag{4.72}$$

$$\frac{\partial\rho_{22}}{\partial t} = i\sigma_{21}^*\Omega_p - i\sigma_{21}\Omega_p^* - \rho_{22}\Delta_{22} + i\frac{\varepsilon_p^*\varepsilon_c}{4\hbar^2}\sigma_{32}\left(\Pi_{32}^c + iG_{32}^c/2\right) - i\frac{\varepsilon_p\varepsilon_c^*}{4\hbar^2}\sigma_{32}^*\left(\left(\Pi_{23}^c\right)^* - i\left(G_{23}^c\right)^*/2\right), \tag{4.73}$$

$$\frac{\partial\rho_{33}}{\partial t} = -\rho_{33}\Delta_{33} + i\frac{\varepsilon_p\varepsilon_c^*}{4\hbar^2}\sigma_{32}^*\left(\Pi_{32}^p + iG_{32}^p/2\right) - i\frac{\varepsilon_p^*\varepsilon_c}{4\hbar^2}\sigma_{32}\left(\left(\Pi_{23}^p\right)^* - i\left(G_{23}^p\right)^*/2\right). \tag{4.74}$$

Here the complex dressed decay rates

$$\Delta_{21} = \gamma_{21} + \frac{|\varepsilon_p|^2}{4\hbar^2}\frac{\Gamma_2^p}{2} + \frac{|\varepsilon_c|^2}{4\hbar^2}\frac{\Gamma_2^c}{2} + i\left(\frac{E_2-E_1}{\hbar} - \omega_p - \frac{|\varepsilon_p|^2}{4\hbar^2}P_2^p - \frac{|\varepsilon_c|^2}{4\hbar^2}P_2^c\right),$$

$$\Delta_{32} = \gamma_{32} + \frac{|\varepsilon_p|^2}{4\hbar^2}\frac{\Gamma_2^p+\Gamma_3^p}{2} + \frac{|\varepsilon_c|^2}{4\hbar^2}\frac{\Gamma_2^c+\Gamma_3^c}{2} + i\left(\frac{E_3-E_2}{\hbar} - \omega_p + \omega_c - \frac{|\varepsilon_p|^2}{4\hbar^2}\left(P_3^p - P_2^p\right) - \frac{|\varepsilon_c|^2}{4\hbar^2}\left(P_3^c - P_2^c\right)\right),$$

$$\Delta_{31} = \gamma_{31} + \frac{|\varepsilon_p|^2}{4\hbar^2}\frac{\Gamma_3^p}{2} + \frac{|\varepsilon_c|^2}{4\hbar^2}\frac{\Gamma_3^c}{2} + i\left(\frac{E_3-E_1}{\hbar} - 2\omega_p + \omega_c - \frac{|\varepsilon_p|^2}{4\hbar^2}P_3^p - \frac{|\varepsilon_c|^2}{4\hbar^2}P_3^c\right),$$

$$\Delta_{11} = \Gamma_1,$$

$$\Delta_{22} = \Gamma_2 + \frac{|\varepsilon_p|^2}{4\hbar^2}\Gamma_2^p,$$

$$\Delta_{33} = \Gamma_3 + \frac{|\varepsilon_p|^2}{4\hbar^2}\Gamma_3^p + \frac{|\varepsilon_c|^2}{4\hbar^2}\Gamma_3^c$$

include dynamic Stark shifts, transition broadening due to photoionization as well as phenomenological coherence and population decay rates γ_{ij}, Γ_i.

Wave equations for the slowly varying amplitudes of the probe and control fields are:

$$\frac{\partial\varepsilon_p}{\partial z} + \frac{n_p}{c}\frac{\partial\varepsilon_p}{\partial t} = \frac{4\pi i N\omega_p}{n_p c}\left(\sigma_{21}\mu_{12} + \rho_{22}\frac{\varepsilon_p}{2\hbar}\left(P_2^p + i\Gamma_2^p/2\right) + \rho_{33}\frac{\varepsilon_p}{2\hbar}\left(P_3^p + i\Gamma_3^p/2\right) + \right.$$

$$\left. + \frac{\varepsilon_c}{2\hbar}\sigma_{32}\left(\Pi_{32}^c + iG_{32}^c/2\right)\right), \tag{4.75}$$

$$\frac{\partial\varepsilon_c}{\partial z} + \frac{n_c}{c}\frac{\partial\varepsilon_c}{\partial t} = \frac{4\pi i N\omega_c}{n_c c}\left(\rho_{22}\frac{\varepsilon_c}{2\hbar}\left(P_2^c + i\Gamma_2^c/2\right) + \rho_{33}\frac{\varepsilon_c}{2\hbar}\left(P_3^c + i\Gamma_3^c/2\right) + \right.$$

$$\left. + \frac{\varepsilon_p}{2\hbar}\sigma_{32}^*\left(\Pi_{32}^p + iG_{32}^p/2\right)\right), \tag{4.76}$$

where n_c is the refractive index of the host medium at the control field frequency. In the same way as in the previous section we neglect all coherence and population relaxation terms to simplify the theoretical analysis, assuming that pulses are sufficiently short. Other assumptions are: 1) $P_m^l = 0$ and $\Pi_{sq}^l = 0$, which is similar to the assumption of the flat continuum; 2) $\omega_p = (E_2 - E_1)/\hbar$ and $\omega_p - \omega_c = (E_3 - E_2)/\hbar$ so that the probe field is in one-photon resonance with the $1 \leftrightarrow 2$ transition and the control and probe fields are in a two-photon resonance with the transition $3 \leftrightarrow 2$; 3) $\Gamma_2^c = 0$ and $\Gamma_3^p = 0$ which means that the control (probe) field is not absorbed from the level 2 (3) into the continuum. From Eqs.(4.69)-(4.74) it follows that $\sigma_{21,31}$ are pure imaginary and σ_{32}, $\varepsilon_{p,c}$ are real. Hence we can use state amplitude description setting $\rho_{11} = a_1^2$, $\rho_{22} = a_2^2$, $\rho_{33} = a_3^2$ and $\sigma_{21} = -ia_1a_2$, $\sigma_{32} = a_2a_3$, $\sigma_{31} = -ia_1a_3$.

Introducing dimensionless time $T = 2t\mu_{21}^2/\sqrt{\Gamma_2^p\Gamma_3^c}$, coordinate $Z = 2z\mu_{21}^2/c\sqrt{\Gamma_2^p\Gamma_3^c}$, field amplitudes

$$u_1 = \varepsilon_p \frac{\sqrt{\Gamma_2^p\Gamma_3^c}}{4\hbar\mu_{21}},$$

$$u_2 = \varepsilon_c \frac{\sqrt{\Gamma_2^p\Gamma_3^c}}{4\hbar\mu_{21}},$$

taking into account that on resonance $G_{23}^c/\sqrt{\Gamma_2^p\Gamma_3^c} = 1$, $G_{32}^p/\sqrt{\Gamma_2^p\Gamma_3^c} = 1$, and going over to a retarded frame defined by coordinates $\tau = T - Z/v$, $\xi = Z$ with $v = Vn_c/c$, we rewrite Eqs.(4.69)-(4.74), (4.75)-(4.76) in the following way:

$$\frac{da_1}{d\tau} = u_1 a_2, \tag{4.77}$$

$$\frac{da_2}{d\tau} = -u_1 a_1 - u_1^2 a_2 q - u_1 u_2 a_3, \tag{4.78}$$

$$\frac{da_3}{d\tau} = -\frac{a_3 u_2^2}{q} - u_1 a_2 a_3, \tag{4.79}$$

$$\frac{du_1}{d\tau} = -\alpha_1^2 \left(a_1 a_2 - q u_1 a_2^2 - u_2 a_2 a_3\right), \tag{4.80}$$

$$\frac{du_2}{d\tau} = \alpha_2^2 \left(\frac{u_2 a_3^2}{q} + u_1 a_2 a_3\right), \tag{4.81}$$

where dimensionless parameters $q = \sqrt{\Gamma_2^p/\Gamma_3^c}$, $\alpha_1 = \sqrt{\nu_1/g_1}$ and $\alpha_2 = \sqrt{\nu_2/g_2}$ with $g_{1,2} = c/n_{p,c}V - 1$ and $\nu_{1,2} = \pi N\omega_{p,c}\Gamma_2^p\Gamma_3^c/2\hbar n_{p,c}^2\mu_{21}^2$ were introduced and $\frac{\partial}{\partial\xi} = 0$ was set in order to find a steady-state solution.

This system has two conservation integrals: one is the energy conservation integral similar to Eq.(4.50)

$$\frac{u_1^2}{\alpha_1^2} + a_2^2 + 2a_1^2 = 1, \tag{4.82}$$

and another one is:

$$\frac{u_2^2}{\alpha_2^2} + a_3^2 = \frac{\left(u_2^0\right)^2}{\alpha_2^2}. \tag{4.83}$$

The last integral is typically encountered in the case of a stationary wave propagating

in a two-level medium with the upper level replaced by the continuum. The integrals correspond to the initial conditions (before the probe pulse enters the medium): $\rho_{11}(\tau \to -\infty) = \rho_{33}(\tau \to -\infty) = 0$, $\rho_{22}(\tau \to -\infty) = 1$, and $u_2(\tau \to -\infty) = u_2^0$, $u_1(\tau \to -\infty) = 0$. The initial conditions describe the case of a cw control field.

Having the integrals, we can reduce the system (4.77)-(4.81) to three equations. It is convenient to use new variables:

$$a = a_1, \tag{4.84}$$

$$b = a_2\sqrt{1 - 2a_1^2 - a_2^2}, \tag{4.85}$$

$$c = a_3, \tag{4.86}$$

and a new time $\tau' = \tau\alpha_1$, so that the system (4.77)-(4.81) can be rewritten as:

$$\frac{da}{d\tau'} = b, \tag{4.87}$$

$$\frac{db}{d\tau'} = -a(1 - 2a^2) + 2\sqrt{\left(\frac{1}{2} - a^2\right)^2 - b^2}\left(\alpha b + c\sqrt{\beta^2 - \alpha_2^2 c^2}\right), \tag{4.88}$$

$$\frac{dc}{d\tau'} = -\frac{\sqrt{\beta^2 - \alpha_2^2 c^2}}{\alpha}\left(c\sqrt{\beta^2 - \alpha_2^2 c^2} + \alpha b\right). \tag{4.89}$$

The system (4.87)-(4.89) can be analyzed along the same lines as in the previous subsection using the phase space technique. The stationary point of the system corresponding to our initial conditions is: $a = 0$, $b = 0$, $c = 0$. Linearizing the system in the vicinity of the stationary point we arrive at the following characteristic equation for eigenvalues:

$$\lambda^3 + \lambda^2\left(\frac{\beta^2}{\alpha} - \alpha\right) + \lambda + \frac{\beta^2}{\alpha} = 0, \tag{4.90}$$

where parameters $\alpha = q\alpha_1$ and $\beta = u_2^0$ were introduced.

In analogy with the previous subsection we conclude that the continuum-coupled

soliton is realized when the stationary point is of an unstable node type. Coefficients of Eq.(4.90) allow only one such solution: one eigenvalue is negative, two other eigenvalues are positive - so-called saddle-node point. Again, one positive eigenvalue describes fast growing solution, the other one represents the solution which uses population inversion efficiently. It is necessary to look for the case, when the faster solution has minimum growth rate, corresponding to the minimum ionization rate and the most effective usage of inversion. Repeating the procedure of the previous subsection we analyze the situation, when the characteristic equation has two equal positive eigenvalues. These are given by the expression:

$$\lambda_{1,2} = \frac{\alpha_1}{3^{2/3}} \left(\left(9\beta^2/\alpha + \sqrt{81(\beta^2/\alpha)^2 - 3)} \right)^{1/3} + \left(9\beta^2/\alpha - \sqrt{81(\beta^2/\alpha)^2 - 3)} \right)^{1/3} \right), \tag{4.91}$$

and it is easy to show that $\lambda_{1,2}$ are always real. The negative eigenvalue in this case is:

$$\lambda_3 = \frac{\alpha_1}{3} \left((\alpha - \beta^2/\alpha) - 2\sqrt{(\alpha - \beta^2/\alpha)^2 - 3} \right). \tag{4.92}$$

There is an additional relation between $\lambda_{1,2}$ and λ_3: $\lambda_{1,2}^2 + 2\lambda_{1,2}\lambda_3 - 1 = 0$, which allows one to obtain the relation between α and β and thus to obtain the velocity of the steady-state pulse. The relation between α and β^2/α is depicted in Fig.35. For $\beta \to 0$ we see that $\alpha \to 2$, as expected from the two-level case. For sufficiently large β ($\beta^2/\alpha \gg 1$), the relation is $\alpha = 3.5 + 1.09\beta^2/\alpha$, which means that $\alpha \approx \beta$. This last relation gives the steady-state solution velocity as:

$$\frac{1}{V} = \frac{n_p}{c} + \frac{\pi N \omega_p (\Gamma_2^p)^2}{2c\hbar n_p \mu_{21}^2 \left(u_2^0\right)^2}, \tag{4.93}$$

which is exactly the group velocity of the pulse in the EIT regime [131], if one recalls that for large intensity of the control field the width of the EIT resonance is: $\Gamma_{EIT} \approx$

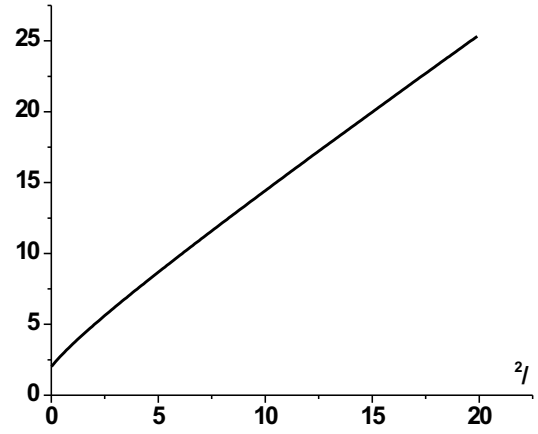

Fig. 35. Relation between α and β^2/α, determined from the relation between roots λ_1 and λ_3.

$|\varepsilon_c|^2\Gamma_c^3/8\hbar^2 = 2\left(u_2^0\right)^2\mu_{21}^2/\Gamma_2^p$, so that

$$\frac{1}{V_{EIT}} = \frac{n_p}{c} + \frac{\pi N\omega_p\Gamma_2^p}{c\hbar n_p}\frac{1}{\Gamma_{EIT}} = \frac{n_p}{c} + \frac{N\sigma_{ESA}}{2\Gamma_{EIT}}. \tag{4.94}$$

Changing the amplitude of the control field one can either accelerate or slow down the soliton. When the control field intensity is close to the ESA suppression threshold for the probe field, the wave has the lowest velocity. This happens when $|\varepsilon_c|^2\Gamma_3^c/8\hbar^2 \sim \gamma_{32}\left(\sigma_{ESA} - \sigma_{SE}\right)/\sigma_{SE}$. The situation is similar to the one typically observed in slow-light experiments [132].

For $\beta \gg 1$, we obtained that $\alpha \approx \beta$, meaning that $\alpha^{-1},\ \beta^{-1}$ are small parameters. This suggests that there are two different regimes of system evolution, adiabatic and non-adiabatic, and a small parameter $\mu = 1/\beta \ll 1$ characterizes the non-adiabaticity of the interaction of the fields and the medium [133]. The system (4.87)-(4.89) can be cast as:

$$\frac{da}{d\tau'} = b, \tag{4.95}$$

$$\mu\frac{db}{d\tau'} = -a\mu\left(1-2a^2\right) + 2\sqrt{\left(\frac{1}{2}-a^2\right)^2 - b^2}\left(b + c\sqrt{1-\frac{\alpha_2^2c^2}{\beta^2}}\right), \tag{4.96}$$

$$\mu\frac{dc}{d\tau'} = -\sqrt{1-\frac{\alpha_2^2c^2}{\beta^2}}\left(b + c\sqrt{1-\frac{\alpha_2^2c^2}{\beta^2}}\right). \tag{4.97}$$

In order to analyze adiabatic evolution we let $\mu \to 0$. The derivatives in the left hand sides are of the order of unity and, multiplied by μ, can be neglected. Then we get the adiabatic evolution condition:

$$b + c\sqrt{1-\frac{\alpha_2^2c^2}{\beta^2}} = 0, \tag{4.98}$$

which is the same as $a_2\varepsilon_p\sqrt{\Gamma_2^p} + a_3\varepsilon_c\sqrt{\Gamma_3^c} = 0$. This expression means that the system is in the "dark" or decoupled superposition of the states $|2>$ and $|3>$, non-interacting with the fields. As follows from Eqs.(4.95)-(4.96) the adiabatic evolution is governed by the system of equations:

$$\frac{da}{d\tau'} = b, \tag{4.99}$$

$$\frac{db}{d\tau'} = -2a\left(\frac{1}{2}-a^2\right), \tag{4.100}$$

having the following solution:

$$a = \pm\frac{1}{\sqrt{2}}\tanh(\tau'/\sqrt{2}), \tag{4.101}$$

$$b = \pm\frac{1}{2}\frac{1}{\cosh^2(\tau'/\sqrt{2})}, \tag{4.102}$$

and from Eq.(4.98):

$$c = \sqrt{\frac{\beta^2}{2\alpha_2^2}\left(1-\sqrt{1-\frac{\alpha_2^2}{\beta^2}\frac{1}{\cosh^4(\tau'/\sqrt{2})}}\right)}. \tag{4.103}$$

In fact, the system never reaches the "dark" state because of the constant perturbation due to amplificaton of the probe field, although it approaches it in the limit

$\tau' \to \infty$. So Eqs.(4.101)-(4.103) correctly describe only the trailing edge amplitude behavior, when the system evolves into another stationary point $a = \pm 1/\sqrt{2}$, $b = 0$, $c = 0$. The asymptotic behavior is then $1/2 - \rho_{11} \sim 2\exp(-\tau'\sqrt{2})$, $\rho_{22} \sim \exp(-\sqrt{2}\tau')$, $\rho_{33} \sim \exp(-2\sqrt{2}\tau')$, $u_1 \sim \alpha_1 \exp(-\tau'/\sqrt{2})$, and $u_2 \to u_2^0$.

The leading edge of the pulse rises during the time $\tau' \sim 1/\beta$, which is equivalent to $t \sim 8\hbar^2/|\varepsilon_c|^2\Gamma_3^c$ and it is nothing but the inverse time γ_{pump}^{-1} of optical pumping by the control field via the continuum. At this non-adiabatic stage, during which the probe field main growth takes place, the populations of states 2 and 3 are redistributed by the probe and control fields so that the "bright" state becomes empty. After that the populations are in the "dark" state and no further growth of the probe pulse occurs, as was shown above its amplitude eventually decreases to zero on the time scale $\tau' \sim 1$ or $t \sim \sqrt{\frac{\Gamma_2^p}{\Gamma_3^c}}\frac{2\hbar}{|\varepsilon_c|\mu_{21}}$.

In Fig.36 results of a numerical solution of Eqs.(4.69)-(4.74), (4.75)-(4.76) are presented, showing the formation of the steady-state solitary wave. Interaction of the probe and control pulses when their intensities become comparable leads to the formation of a propagating pair of complimentary pulses, similar to adiabatons. Numerical analysis shows that the amplitude and velocity of the probe pulse depend on the initial control field amplitude and for $\beta \gg 1$ grow respectively linearly and quadratically with the amplitude. The dip in the control beam intensity profile moves at the group velocity of the probe pulse, while the bump travels with the control field group velocity. The same behavior was observed already in the first experiment studying propagation dynamics of a probe pulse in the EIT regime (Ref.[134]). In Ref.[133] it was shown that in a three-level atomic system a pair of adiabatons rapidly decays after some propagation distance if the upper state decay rate exceeds the effective fields Rabi frequency. In our case the decay rate of the coherences at ESA transitions significantly exceeds all other decay rates and Rabi frequencies. In spite of this, a

shape-invariant pair of pulses forms. The reason is that although losses to the continuum are present, amplification at the $2 \leftrightarrow 1$ transition allows the probe field to adjust to the changes of the states 2 and 3 populations, so that the system stays in the "dark" state.

In a more realistic situation it is necessary to take into account probe absorption from state 3, since it will inevitably take place unless some special probe beam polarization is chosen. In Fig.37 results of a numerical solution of the system Eqs.(4.69)-(4.74), (4.75)-(4.76), taking into account probe absorption from the state 3 are presented. The main difference is that the control field does not return to the value it had before the probe pulse had arrived, since depletion of the state 3 population by the probe into the continuum destroys the "dark" state, which, in turn, leads to additional losses for both the probe and the control field.

The above analysis assuming cw control field allowed us to obtain some analytical results and find how the steady-state probe pulse parameters depend on the control field amplitude. As was shown in Ref.[108] intensities of the control field required to suppress ESA are close to a damage threshold of many crystals, so this technique is feasible only in a pulsed regime. We analyzed numerically the case of a pulsed control field taking into account probe absorption from state 3 and optical coherence relaxation. In Fig.38 the results of calculations are presented. A strong control pulse and a weak probe pulse, both of Gaussian shape, are sent into the medium such that at $\tau = 0$ the maximal amplitude part of the control pulse enters the medium's boundary $\xi = 0$ and the probe pulse is shifted to the leading edge of the control pulse. The probe pulse first is amplified because ESA is suppressed by the strong control field. As its amplitude grows the probe field starts to transform into the steady-state pulse descibed above (note the step it produces in the control pulse profile, similar to that of Fig.37). The transformation into the steady-state soliton is accompanied

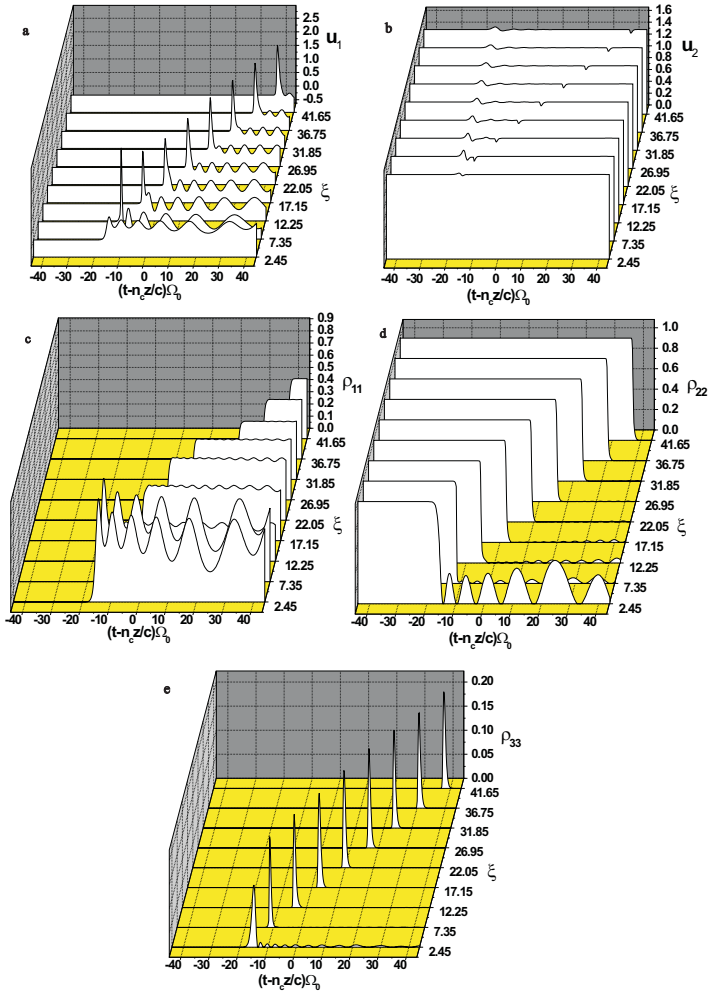

Fig. 36. Numerical solution of Eqs.(4.69)-(4.74), (4.75)-(4.76) in the retarded frame with a cw control field, neglecting probe absorption from state 3. Probe pulse is defined at the entrance to the medium as: $u_1(\tau, \xi = 0) = 0.0003 \exp(-16(\tau + 27)^2)$; other parameters are: $\beta = 1.43$, $\Gamma_2^p = \Gamma_3^c$, $\nu_1 = 1$, $\nu_2 = 3$, $n_p = n_c = 1$, parameter $\Omega_0 = 2\mu_{21}^2/\sqrt{\Gamma_2^p \Gamma_3^c}$ describes inverse pulse width.

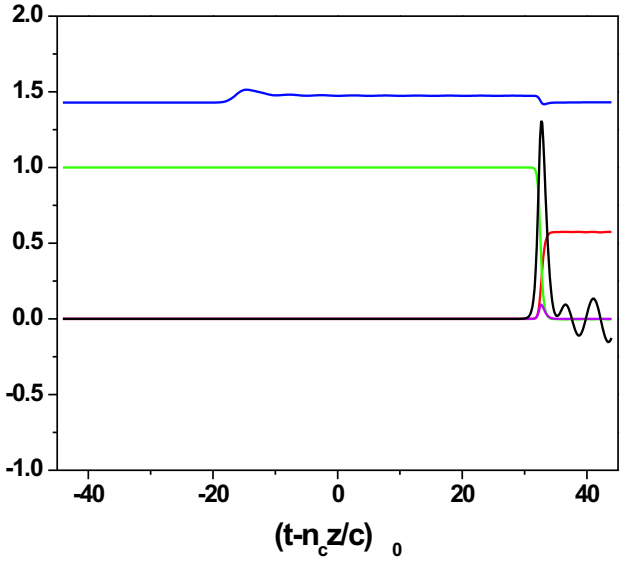

Fig. 37. Numerical solution of Eqs.(4.69)-(4.74), (4.75)-(4.76) with a cw control field, taking into account probe absorption from state 3. Normalized propagation distance is $\xi = 36.75$; $\Gamma_2^p = \Gamma_3^c = \Gamma_3^p$. Probe and control fields are shown as black and blue curves, populations ρ_{11}, ρ_{22}, and ρ_{33} are given by red, green and violet curves, respectively. Other parameters are as in Fig.36.

by deceleration of the probe pulse, which leads to its lagging behind the control pulse, which moves with its group velocity. As the probe pulse shifts towards the trailing edge of the control pulse, where the conditions for ESA suppression are not met because of an insufficient control field amplitude, it gets absorbed and eventually vanishes. This calculation shows that for optimal amplification it is necessary that the probe pulse leaves the medium before this absorption starts.

Let us make estimates of the parameters of the control and probe pulse for rare-earth and transition metal ion doped crystals. First, we consider the soliton described in Sec.C. For an estimate the velocity of the soliton, given by Eq.(4.61), can be rewritten in the following way:

$$V = \frac{c}{n_p \left(1 + \frac{Nc(\sigma_{ESA})^2}{4\sigma_{SE}\gamma_{21}}\right)},$$

where $\sigma_{ESA} = 2\pi\omega_p\Gamma_2^p/2cn_p\hbar$, $\sigma_{SE} = 2\pi\omega_p\mu_{21}^2/\gamma_{21}cn_p\hbar$ are the ESA and stimulated emission cross-sections and γ_{21} is the width of the amplifying transition. Typical values of the parameters determining the velocity are: ESA cross-section from a metastable state of an ion ($3d$, $4f$ or $5d$) into the conduction band is $\sigma_{ESA} \sim 10^{-19} - 10^{-17}$ cm^2, ion density $N \sim 10^{19}$ cm^{-3}, and homogeneous linewidth of an amplifying optical transition at liquid helium temperature $\gamma_{21} \sim 10 - 100$ GHz. In this estimate we assume that the homogeneous linewidth is greater than the inhomogeneous one and that $\sigma_{ESA} \sim \sigma_{SE}$. The velocity estimate gives a value of the order of several tens percent of c. At the early stage of pulse propagation, when it evolves as the nonstationary π pulse, the amplitude of the pulse grows linearly with distance as $u \sim Z\nu$. It begins to transform into the steady-state solution when $u \sim 1$, so the characteristic distance of soliton formation is $Z_{ch} \sim 1/\nu$, which is equivalent to $z \sim (\sigma_{ESA}N)^{-1}$ and for the parameters cited above it gives a reasonable value of

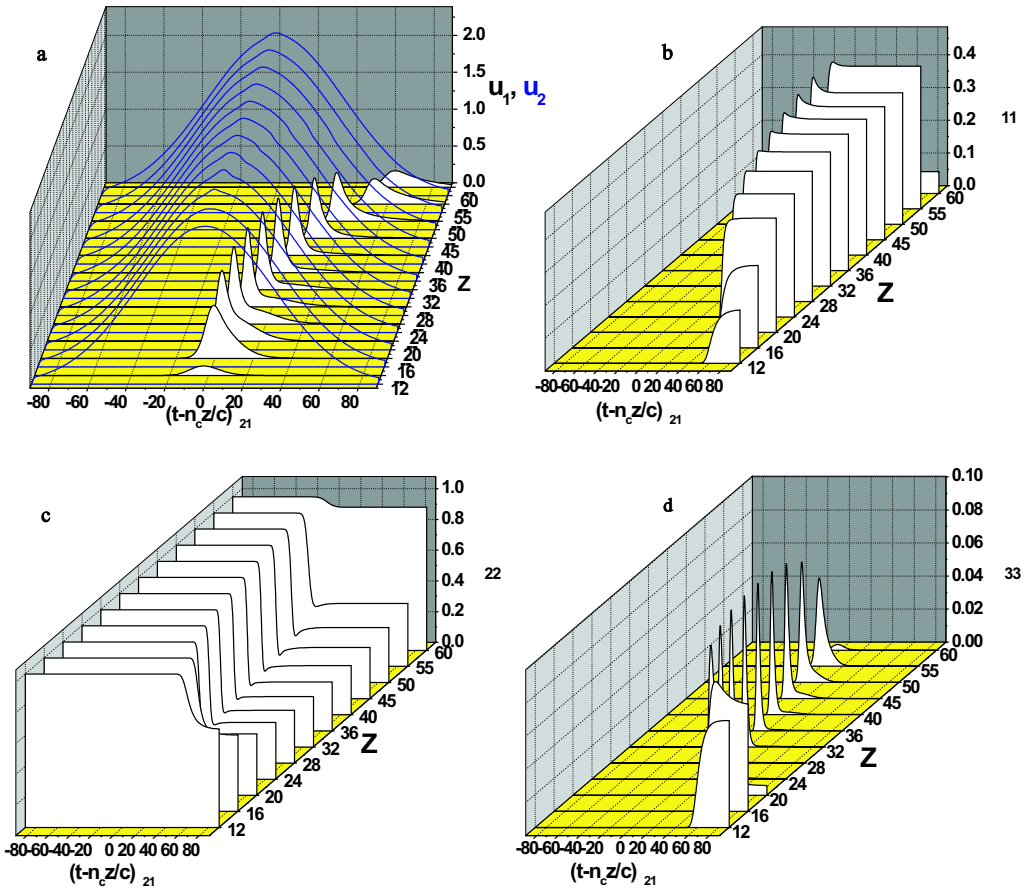

Fig. 38. Numerical solution of the system Eqs.(4.69)-(4.74), (4.75)-(4.76) in the retarded frame with pulsed control field, taking into account probe absorption from state 3 and both optical and two-photon coherence relaxations. Fields are given at the entrance to the medium as: $u_1 = 0.0003 \exp\left(-(t + 55\gamma_{21}^{-1})^2/(0.5\gamma_{21}^{-1})^2\right)$, $u_2 = 2.14 \exp\left(-t^2/(50\gamma_{21}^{-1})^2\right)$. Parameters are: $\sigma_{ESA}/\sigma_{SE} = 2$, $\gamma_{32} = 0.01\gamma_{21}$, $\gamma_{31} = \gamma_{21}$, $\nu_1 = 1$, $\nu_2 = 3$, $n_p = n_c = 1$ and $Z = z\gamma_{21}/c$.

$z \sim 0.1 - 1$ cm. The peak intensity of the soliton can be estimated from the condition that the peak Rabi frequency is $\Omega_p \sim 1/t_p$, giving

$$I \sim \frac{c\hbar^2 \mu_{21}^2}{\pi(\Gamma_p^2)^2} = \frac{\sigma_{SE}}{\sigma_{ESA}} \frac{\hbar\omega_p \gamma_{21}}{2n_p \sigma_{ESA}}.$$

Assuming again $\sigma_{SE} \sim \sigma_{ESA}$ and $\hbar\omega_p \sim 2$ eV, we arrive at the peak intensity $I \sim 100$ GW/cm^2, for a pulse duration of several ps and a beam diameter of the order of 1 mm it would result in a pulse energy ~ 1 mJ.

Finally we consider the three-level case with the control field suppressing ESA. As the numerical analysis shows the optimal probe amplification happens if the control field duration is $\sim 100\gamma_{21}^{-1}$. Taking $\gamma_{21} \sim 10 - 100$ GHz we obtain the control pulse duration of the order of $0.1 - 1$ ns. The peak intensity of the control pulse has to exceed a threshold value $I_{th} = 4\pi\gamma_{32}\hbar c/\sigma_{ESA}\lambda_c$ (Ref.[108]) and for interconfigurational $4f^{n-1}5d \rightarrow 4f^n$ transitions with parameters $\sigma_{ESA} \sim 10^{-17} - 10^{-18}$ cm^2, $\gamma_{32} \sim \gamma_{21} \sim 10 - 100$ GHz and control field wavelength $\lambda_c \sim 0.3 - 1$ μm it gives $I_{th} \sim 10 - 100$ GW/cm^2. It gives an estimate of the required fluence of the control field of $1 - 10$ J/cm^2, which is close for the damage threshold of the crystals, but is still tolerable [125]. As can be seen from Fig.38 the length of the crystal optimal for probe amplification is given by the dimensionless value of $Z \sim 30$, which gives the reasonable crystal length of $z \sim 1 - 10$ cm. The resulting amplitude of the steady-state probe pulse is of the order of the control pulse amplitude, so the peak intensity of the probe pulse in the best case will be comparable to that of the control pulse. As was shown in Section A3 the linear gain is given by the expression $\alpha_{gain} = (\sigma_{SE} - \sigma_{ESA}/(I_c/I_{th} + 1))\, N$, if the ESA cross-section is reduced such that the expression in brackets is of the order of $\sigma_{SE} \sim 10^{-19} - 10^{-18}$ cm^2, at the density of dopant ions $N \sim 10^{18} - 10^{19}$ cm^{-3} the linear gain is high: $\alpha_{gain} \sim 1 - 10$ cm^{-1}. The duration of the pulse is short, in terms of dimensionless time it is expressed as

$\tau' \sim 1/\beta$, which is equivalent to $t_p \sim \gamma_{21}^{-1}(\sigma_{ESA}/\sigma_{SE}\beta^2)$. Taking into account that $\beta^2 \geq \beta_{th}^2 = \gamma_{32}\sigma_{ESA}/\gamma_{21}\sigma_{SE}$ we have that $t_p \leq \gamma_{32}^{-1}$, so that pulse duration will be $t_p \sim 1 - 10$ ps. It gives an upper estimate of the probe field fluence $\sim 0.01 - 1$ J/cm^2 and the energy $\sim 0.1 - 10$ mJ for a 1 mm beam diameter. As follows from the numerical analysis the control pulse is not depleted during the probe amplification, it changes only slightly (see the small step on the control pulse profile in Fig.38). Thus, if a cavity is used, the same control pulse can pass trough a crystal periodically, producing a train of amplified pulses at a desired wavelength. The efficiency of the scheme proposed is, therefore, determined by the efficiency of the use of an incoherent pump and can be comparable to that of typical solid-state lasers.

D. Conclusions

It was theoretically demonstrated that excited state absorption, which prevents the realization of UV or VUV lasers in rare-earth and transition metal ion doped crystals, can be greatly reduced by applying an additional driving laser field. The approach is based on the effect of electromagnetically induced transparency. Estimates for typical parameters of laser crystals show that requirements for the driving field are experimentally feasible. An additional advantage of the proposed technique is that it allows one to tune the laser wavelength by tuning the driving field wavelength due to selective reduction of the lasing threshold in a narrow spectral region in the vicinity of a two-photon resonance with the driving field. Due to high intensities of the driving field required for efficient ESA suppression, the technique will most probably be confined to a pulsed regime. Propagation and amplification dynamics of a probe pulse in a resonant amplifying medium with excited-state absorption from an upper level are analyzed analytically and numerically. Continuum-coupled soliton

solutions are found. Namely, it is shown that a steady-state solution of a dissipative soliton type forms in the system if the stimulated emission cross-section exceeds the excited-state absorption cross-section. If this condition is not fulfilled naturally, the ESA cross-section can be decreased by applying an additional control laser beam to some transition, adjacent to the ESA transition. The continuum-coupled solitons are formed in the presence of a cw control field, on the one hand the control and probe fields form in this case a complimentary pair of pulses closely resembling adiabatons, on the other hand the probe pulse is very similar to the π pulse encountered in resonant amplifiers with linear losses. In a more realistic situation of a pulsed control field amplification of the probe pulse is transient and for optimal amplification it is necessary that the medium has some specific length. Estimates of parameters of the pulses for rare-earth and transition metal ion doped crystals predict generation of pulses of picosecond duration and several tens gigawatt per cm^2 peak intensity, corresponding to mJ energy.

CHAPTER V

COMPRESSION OF MÖSSBAUER RADIATION INTO ULTRASHORT PULSES

A. Overview of the Mössbauer effect and coherent transient phenomena observed in Mössbauer experiments

The Mössbauer effect is recoilless gamma-ray emission and absorption by radioactive nuclei in solids [135]. For a free nucleus emission and absorption of a photon is always accompanied by recoil. If a nucleus decays from state $|e>$ to state $|g>$ emitting a photon of energy E_γ, momentum conservation requires that the momentum of the photon and of the nucleus be equal and opposite. The nucleus, therefore, experiences recoil and receives an energy $E_{recoil} = E_\gamma^2/2Mc^2$, where M is the mass of the nucleus, c is the speed of light. Energy conservation gives the energy of the emitted photon: $E_{eg} = E_\gamma + E_{recoil}$, with E_{eg} being the nuclear transition energy. It means that the energy of the photon is red-shifted with respect to the nuclear transition energy. The same reasoning shows that in order for the photon to be absorbed its energy has to be blue-shifted with respect to the transition energy. So emission and absorption profiles are separated by twice the recoil energy. For gamma-rays this separation is typically much greater than the natural linewidth of nuclear transitions and the profiles do not overlap. In a gas due to thermal motion of atoms all transitions are Doppler broadened but the recoil energy for gamma-ray transitions is comparable to or exceeds the Doppler width, thus making experiments with resonance absorption or fluorescence extremely difficult. The Mossbauer effect eliminates both recoil and Doppler broadening and leads to unbroadened nuclear transitions. The origin of the effect is that if a nucleus is imbedded in a solid it can with a finite probability emit a gamma-quantum without recoil. To be precise, the recoil is taken up by

the solid as a whole. The recoil energy given to the entire solid is approximately $E_{recoil}^{solid} = E_{recoil} M_{atom}/M_{solid}$, where M_{atom} and M_{solid} are the atom and the solid host masses, respectively. Compared to the free atom the recoil energy is reduced by the ratio M_{atom}/M_{solid}. This extremely small energy goes into motion of the entire solid and can be neglected. The transition energy is thus shared between the gamma ray and the phonons. A Mössbauer transition occurs if the state of the lattice remains unchanged, and the gamma ray gets the entire transition energy. In an idealized case when the Debye model is used to describe host lattice vibrations, the probability of recoilless emission/absorption is given by the expression:

$$f = \exp\left(-\frac{3E_{recoil}}{2k_B\Theta_D}\left[1 + 4\left(\frac{T}{\Theta_D}\right)^2 \int_0^{\Theta_D/T} \frac{x\,dx}{e^x - 1}\right]\right), \tag{5.1}$$

where T is the temperature and Θ_D is the Debye temperature of the host, k_B is the Boltzmann constant. This probability can be quite high even at room temperature, for many ^{57}Fe containing materials it can reach values close to unity. Since the atom does not leave its lattice site it cannot acquire translational motion, so there is no Doppler broadening, transitions are extremely narrow, with widths close to natural (typically in the kHz to tens MHz range).

The possibility to experimentally observe narrow resonances in nuclear emission/absorption provides a basis for a fine spectroscopic technique, called Mössbauer spectroscopy [136]. In materials research Mössbauer spectroscopy is commonly used to study hyperfine interactions in energy (frequency) domain. In a standard Mössbauer experiment the source is mechanically shifted back and forth relative to the position of a stationary resonant absorber. This leads to a linear Doppler shift in the spontaneously emitted gamma-ray energy. As a result, a spectroscopical scan can be performed in a narrow energy range that is usually still large enough for observing

the hyperfine split resonance lines in various materials. This Doppler scan is typically performed at small maximum velocities (of the order of 10 mm/s for ^{57}Fe) and at relatively modest frequencies (several Hz). The hyperfine structure becomes thus directly mapped by the Doppler velocity.

A dramatic change is observed when the Doppler scanning period is shortened so much that the scanning frequency starts to be comparable with the linewidth of the transition (inverse of the lifetime of the excited state of the emitting nucleus). In this so-called transient regime the lifetime enters the analysis and gives a timescale for the effects to be observed. Coherent transient effects such as dynamical beats [54, 137], quantum beats [46, 138], Mössbauer transients [139]-[143], gamma-echo [51, 144] are intensively studied since late 1970's using frequency modulated Mössbauer radiation. These effects proved to be useful spectroscopic tools for determination of hyperfine interaction parameters such as isomer shifts, recoiless fractions, quadrupole splittings etc. Both synchrotron [141]-[143] and conventional Mössbauer sources are used in experiments where transient effects are observed. In the latter case the technique is as follows: radiation of a source achieves time-dependent phase modulation, either sinusoidal or stepwise, usually via mechanical displacement [51],[137]-[139] or by application of radiofrequency magnetic field which leads to mechanical vibrations through magnitostriction as well as to time-varying splitting of levels [140, 145]. The phase-modulated radiation emitted by the source passes through a resonant absorber and gets some amplitude modulation which is detected in time-domain transmission measurments. In the case of sinusoidal phase modulation three regimes are possible depending on the frequency of modulation: if the frequency is much less than the linewidth of an absorber resonance, we have conventional Mössbauer measurements, if the frequency of modulation becomes of the order of the linewidth the regime is called Mössbauer transients, and if the frequency greatly exceeds the linewidth of the

resonance, the resulting transients are "quantum-beats of recoiless gamma radiation" [137]. Stepwise phase modulation of the source radiation gives rise to gamma-echo phenomenon [51]. Mössbauer transients observed in [139] were used to calibrate mechanical displacements of a source and to determine linewidths and recoilless fractions of both the source and the absorber; in experiments with alternating magnetic fields transients allowed to determine the gyromagnetic ratio of an excited state of the ^{67}Zn nucleus [145].

In the research project a method of manipulation of Mössbauer radiation (produced either by a radioactive Mossbauer source or by coherent nuclear scattering of synchrotron radiation in a Mossbauer absorber) is suggested, which would result in generation of a train of short pulses of coherent gamma radiation with pulse duration much shorter than the nucleus excited state lifetime [146]. The idea of the method has similarities on the one hand with the well known in optics Chirped Pulse Compression technique [147] and on the other hand with a technique, used to study coherent transient effects in Mössbauer experiments. Namely, gamma radiation emitted by a Mössbauer source becomes frequency modulated (chirped) by mechanical vibration of the source due to the Doppler effect, and afterwards it is propagated through a compressor, providing group velocity dispersion. At the exit of the system the frequency modulated radiation gets temporarily compressed into a sequence of short pulses. The compressor can be either a far-detuned resonant Mössbauer absorber of appropriate thickness or a system of Bragg scattering crystals, used as diffraction gratings.

B. Intensity of frequency modulated Mössbauer radiation

Let a Mössbauer source vibrate at some frequency δ along z axis, then emitted radiation will be frequency modulated due to the Doppler effect. We assume that the source thickness is much less than the corresponding acoustic wavelengh therefore all parts of the source move in phase. Otherwise it is nessesary to average over amplitude and phase distributions as in [148]. In the ideal case of a thin source, which we consider, the position of the source depends on time as:

$$z_s = z_0 \sin(\delta t + \varphi),$$

where z_0 is the amplitude of vibration.

Mössbauer radiation consists of well-separated, mutually incoherent gamma-quanta of spontaneous emission (though each individual gamma-quantum is highly coherent) and thus differs significantly from a "classical" field emitted by a laser. However the results of transient Mössbauer experiments can be very successfully explained both qualitatively and quantitatively using classical electrodynamics of a damped harmonic oscillator [149]. In the optical spectral region comparison of classical and quantum electrodynamical theories [150] has shown that former ones can not correctly account for higher order correlation properties of light. For Mössbauer radiation a similar problem was revealed in measurement of, for example, the intensity correlation function $< |E(t)|^2 |E(t')|^2 >$ of the radiation, where $E(t)$ is the total field from all individual source nuclei. Fortunatly, the classical model gives the same first order correlation function of the field associated with a spontaneously emitted photon, $< E(t)E^+(t') >$, as a quantum electrodynamical theory [151]. These results explain why there were no descripancies in classical interpretation of experiments, where only the transmitted or scattered intensity (first order correlation) was measured.

So we will treat the radiation emitted by a single line source classically. Let us assume that the electric field component of the radiation of the source is:

$$E_s \sim e^{-\Gamma_s(t-t_0)/2 - iw_s t}\theta(t-t_0) + c.c.$$

At some distance z from the source and at a moment t the electric field of radiation will be equivalent to the field at some earlier moment t':

$$E_s(z,t) = E_s(z = z_s(t'), t'),$$

where t' is determined by the condition:

$$c(t-t') = z - z_s(t') = z - z_0 \sin(\delta t' + \varphi).$$

If we take into account the condition $z_0\delta/c << 1$, i.e. that the maximum vibrational velocity is much less than the speed of light, we obtain in the zeroth order that

$$t' = t - z/c.$$

Then in the first order

$$t' = t - z/c + z_0/c\ \sin(\delta(t - z/c) + \varphi).$$

So the field associated with a gamma photon emitted by a nucleus in the source is described by

$$E_s(z,t) \sim e^{-\Gamma_s(t'-t_0)/2 - iw_s t'}\theta(t'-t_0) + c.c. = \tag{5.2}$$

$$= e^{-\Gamma_s[t-t_0-z/c+z_0/c\ \sin(\delta(t-z/c)+\varphi)]/2 - iw_s t + ik_s z - ik_s z_0 \sin(\delta(t-z/c)+\varphi)} \times$$

$$\times\theta\left[t - t_0 - z/c + z_0/c\ \sin(\delta(t-z/c)+\varphi)\right] + c.c.$$

Here we assume that radiation propagates in the positive z direction, k_s is the wave number of the radiation, Γ_s is the inverse lifetime of an excited state of a nucleus, c

is the speed of light, $\theta(t)$ is the unit step function, t_0 is the moment when the excited nucleus is formed. In the following we neglect modulation of decay in comparison with modulation of phase since $w_s >> \Gamma_s$, so finally

$$E_s(z,t) \sim e^{-\Gamma_s(t-t_0-z/c)/2-iw_st+ik_sz-ik_sz_0\sin(\delta(t-z/c)+\varphi)}\theta(t-t_0-z/c)+c.c. \qquad (5.3)$$

Following the lines of [152] let us rewrite Eq.(5.3) as a sum over all acoustic sidebands generated via vibration of the source:

$$E_s(t,z) \sim \sum_n J_n(a)e^{-iw_nt+ik_nz-\Gamma_s(t-t_0-z/c)/2-in\varphi}\theta(t-t_0-z/c)+c.c.= \qquad (5.4)$$

$$= \sum_n J_n(a)e^{-iw_nt_0-in\varphi}\left(-\frac{1}{2\pi i}\int\limits_{-\infty}^{\infty} c_n(w,t_0)e^{-iw(t-z/c)}dw\right)+c.c.,$$

where

$$c_n(w,t_0) = \frac{e^{iwt_0}}{w-w_n+i\Gamma_s/2},\ t > t_0+z/c,$$

$w_n = w_s + n\delta$ and $k_n = k_s + n\delta/c$ are the frequency and the wavenumber of n'th acoustic sideband, $a = k_sz_0$ is the modulation index (number of acoustic sidebands generated).

C. Resonant Mössbauer absorber used as a compressor

A common feature of all previous Mössbauer transient experiments is that they were carried out at a condition of resonance between incident radiation and an absorber. It led to considerable resonant absorption and as a consequence to a small amplitude of intensity variation with time. Our idea is the following: if we detune the central frequency of the source radiation far off resonance with an absorber such that the whole spectrum of the radiation "lies" on the tail of the resonance dispersion curve, we get rid of resonance absorption having at the same time some dispersion of refractive

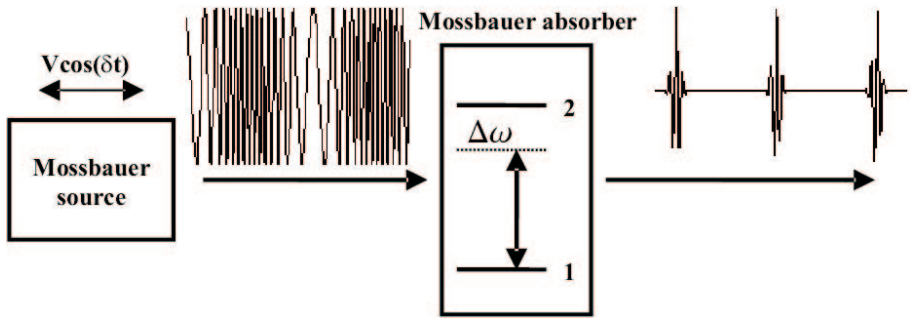

Fig. 39. Schematic diagram of the generation of short gamma-ray pulses with a resonant Mossbauer absorber used as a dispersive element.

index. Though dispersion decays as $\sim 1/(w - w_s)$, absorption decays even faster as $\sim 1/(w - w_s)^2$, so it is possible to neglect absorption while having considerable dispersion.

We assume that the absorber consists of two-level nuclei, as shown in Fig.39, and use density-matrix approach to describe them. The coherence ρ_{21} is then goverened by the equation:

$$\frac{d\rho_{21}}{dt} = -iw_a\rho_{21} + in_{12}\frac{\mu_{21}E}{\hbar} - \gamma_a\rho_{21}, \tag{5.5}$$

where w_a is the frequency of $2 \leftrightarrow 1$ transition, $n_{12} = \rho_{11} - \rho_{22}$ is the population difference between ground and excited states, μ_{21} is the dipole moment matrix element, γ_a is the coherence relaxation rate. Crystal structure of the absorber is not taken into account.

In a steady state the Fourier transform $\sigma_{21}(w, t_0, z)$ of the amplitude of the off-diagonal element $\rho_{21} = \int_{-\infty}^{\infty} \sigma_{21}(w, t_0, z)e^{-iw(t-z/c)}dw$ follows from Eq.(5.5):

$$\sigma_{21}(w, t_0, z) = -\frac{n_{12}\mu_{21}E(w, t_0, z)/\hbar}{w - w_a + i\gamma_a},$$

where $E(w, t_0, z)$ is the Fourier transform of the slowly varying amplitude of the electric field component of the radiation.

For a steady regime, which we consider (Fourier transforms do not depend on time), the propagation equation for the field has the form:

$$\frac{\partial E(w,t_0,z)}{\partial z}+\gamma E(w,t_0,z)=\frac{2\pi i\mu_{21}Nf_a w}{c}(\sigma_{21}(w,t_0,z)+\sigma_{12}(w,t_0,z))\approx$$

$$\approx\frac{2\pi i\mu_{21}Nf_a w}{c}\sigma_{21}(w,t_0,z),$$

where N is the number density of resonant nuclei in the absorber, f_a is the absorber's recoilless fraction, γ describes non-resonant absorption losses. We neglect the term $\sigma_{12}(w,t_0,z)=\sigma_{21}^*(-w,t_0,z)$ due to rotating wave approximation since we restrict ourselves to the case when the width of the generated spectrum $2a\delta << w_a$. Finally for the absorber situated between plates $z=z_{abs}$ and $z=z_{abs}+L$ we obtain the result:

$$E_s(w,t_0,z_{abs}+L)=\exp\left[-\left(\gamma L+\frac{ib}{w-w_a+i\gamma_a}\right)\right]E_s(w,t_0,z_{abs}),$$

where

$$b=2\pi n_{12}\mu_{21}^2 wNf_aL/\hbar c\approx 2\pi\mu_{21}^2 k_sNf_aL/\hbar, \tag{5.6}$$

since the field is weak so that $n_{12}\approx 1$.

The coefficients c_n after radiation passes through the absorber transform as $c_n\rightarrow c_n'$, where

$$c_n'=c_n\exp\left[-\left(\gamma L+\frac{ib}{w-w_a+i\gamma_a}\right)\right],$$

and the field changes as

$$E_s(t,z)\sim\sum_n J_n(a)e^{-iw_nt_0-\gamma L-in\varphi}\left(-\frac{1}{2\pi i}\int\limits_{-\infty}^{\infty}\frac{e^{-ib/(w-w_a+i\gamma_a)-iw(t-t_0-z/c)}}{w-w_n+i\Gamma_s/2}dw\right)\times$$

$$\times\theta(t-t_0-z/c)+c.c. \tag{5.7}$$

In the integrand of Eq.(5.7) $a(w)=e^{-ib/(w-w_a+i\gamma_a)}$ is the absorber response, the

inverse Fourier transform of which is $a(t) = \delta(t) - be^{-iw_a t - \gamma_a t}\sigma(bt)\theta(t)$, where $\sigma(x) = J_1(2\sqrt{x})/\sqrt{x}$. The inverse Fourier transform of $c_n(w, t_0)$ is

$$c_n(t, t_0) = -ie^{-iw_n(t-t_0)-\Gamma_s(t-t_0)/2}\theta(t - t_0).$$

So the integral in Eq.(5.7) can be rewritten as

$$-\frac{1}{2\pi i}\int_{-\infty}^{\infty} c_n(w, t_0)a(w)e^{-iw(t-z/c)}dw = -\frac{1}{2\pi i}2\pi\int_{-\infty}^{\infty} c_n(t - z/c - t', t_0)a(t')dt' =$$

$$= \int_{-\infty}^{\infty}\left[\delta(t') - be^{-iw_a t' - \gamma_a t'}\sigma(bt')\theta(t')\right]e^{-iw_n(t-t_0-z/c-t')-\Gamma_s(t-t_0-z/c-t')/2}\theta(t-t_0-z/c-t')dt' =$$

$$= e^{-iw_n(t-t_0-z/c)-\Gamma_s(t-t_0-z/c)/2}\theta(t-t_0-z/c)\left[1 - b\int_0^{t-t_0-z/c} e^{-i(w_a-w_n)t'-(\gamma_a-\Gamma_s/2)t'}\sigma(bt')dt'\right].$$

It leads to the following expression for the field:

$$E_s(t, z) \sim \sum_n J_n(a)e^{-iw_n t + ik_n z - \gamma L - \Gamma_s(t-t_0-z/c)/2 - in\varphi}\theta(t - t_0 - z/c)\times \tag{5.8}$$

$$\times\left[1 - b\int_0^{t-t_0-z/c} e^{-i(w_a-w_n)t'-(\gamma_a-\Gamma_s/2)t'}\sigma(bt')dt'\right] + c.c. =$$

$$= e^{-iw_s t + ik_s L - \gamma L - \Gamma_s(t-t_0-z/c)/2 - ia\sin(\delta(t-z/c)+\varphi)}\theta(t - t_0 - z/c)\times$$

$$\times\left[1 - be^{ia\sin(\delta(t-z/c)+\varphi)}\int_0^{t-t_0-z/c} e^{i\Delta w t' + ia\sin(\delta(t'-t+z/c-\varphi)-(\gamma_a-\Gamma_s/2)t'}\sigma(bt')dt'\right] + c.c.,$$

where $\Delta w = w_s - w_a$ is the detuning of the center frequency of incident radiation from the absorber resonant frequency.

Finally we arrive at the expression for the resulting time-dependence of intensity of a gamma photon emitted at time t_0:

$$I(t, t_0, z) \sim e^{-2\gamma L - \Gamma_s(t-t_0-z/c)}\theta(t - t_0 - z/c)\times \tag{5.9}$$

$$\times \left| 1 - be^{ia\sin(\delta(t-z/c)+\varphi)} \int_0^{t-t_0-z/c} e^{i\Delta w t' + ia\sin(\delta(t'-t+z/c-\varphi)) - (\gamma_a - \Gamma_s/2)t'} \sigma(bt')dt' \right|^2 .$$

In order to elucidate the way the transmitted signal becomes compressed, we rewrite Eq.(5.8) in a different way. The integral in Eq.(5.7) can be calculated by a contour integration in the complex w plane [149], giving the result

$$E_s(t,z) \sim \sum_n J_n(a) e^{-iw_n t + ik_n z - \gamma L - \Gamma_s(t-t_0-z/c)/2 - in\varphi} \theta(t-t_0-z/c) \times$$

$$\times \Big\{ e^{-ib/(w_n - w_a + i(\gamma_a - \Gamma_s/2))} - e^{-(\gamma_a - \Gamma_s/2 + i(w_a - w_n))(t-t_0-z/c)} \times$$

$$\times \sum_{k=1}^{\infty} \left(\frac{-ib}{w_n - w_a + i(\gamma_a - \Gamma_s/2)} \right)^k \frac{J_k(2\sqrt{b(t-t_0-z/c)})}{(b(t-t_0-z/c))^{k/2}} \Big\} + c.c. \qquad (5.10)$$

The second term in figure brackets converges rapidly if the following condition is fulfilled:

$$\frac{b}{\left[(\Delta w + n\delta)^2 + (\gamma_a - \Gamma_s/2)^2\right]^{1/2}} \frac{1}{\left[b(t-t_0-z/c)\right]^{1/2}} < 1 \qquad (5.11)$$

In our case the detuning from resonance is large ($\Delta w >> \gamma_a$), so (5.11) is satisfied for $t > t_0 + z/c + \frac{b}{(\Delta w)^2}$, then the second term in (5.10) can be neglected. As is clear then from Eq.(5.10) the field at the exit of the absorber is just a sum of incident acoustic sidebands with each sideband having absorption coefficient and refractive index determined by its frequency due to resonant nature of interaction with the absorber's nuclei:

$$E_s(t,z) \sim \sum_n J_n(a) e^{-iw_n t + ik_n z - \gamma L - \Gamma_s(t-t_0-z/c)/2 - in\varphi} e^{-ib/(w_n - w_a + i(\gamma_a - \Gamma_s/2))} \times$$

$$\times \theta(t-t_0-z/c) + c.c. \qquad (5.12)$$

The phase shift for n'th sideband comes from the term $e^{-ib/(w_n - w_a + i(\gamma_a - \Gamma s/2))}$ which, if we neglect absorption, becomes $e^{-ib/(\Delta w + n\delta)} \approx e^{-(ib/\Delta w)\left[1 - n\delta/\Delta w + (n\delta/\Delta)^2\right]}$ for $n\delta << \Delta w$. The quadratic term in Taylor expansion provides group velocity dispersion,

as a result different sidebands propagate through the absorber with different group velocities. The length of the absorber at which signal compression is optimal can be estimated by the requirement that "red-shifted" sidebands reach the exit of the absorber at the same time as "blue-shifted" sidebands. It gives the condition:

$$\left|1/V_g^{red} - 1/V_g^{blue}\right| L = 2\pi/\delta$$

or

$$\frac{\left|\frac{dV_g}{dw}(w=w_s)\right| \delta w}{V_g^2(w=w_s)} L = \left|\frac{d^2k}{dw^2}(w=w_s)\right| \delta w \cdot L = 2\pi/\delta,$$

where δw is the spectral width of the vibrationally generated spectrum and

$$k(w) = k_s - Re(\frac{b/L}{w - w_a + i\gamma_a}) = k_s - \frac{b}{L}\frac{w - w_a}{(w-w_a)^2 + \gamma_a^2}.$$

So under our assumptions $\frac{d^2k}{dw^2}\Big|_{w=w_s} = \frac{2b\Delta w}{L}\frac{3\gamma_a^2 - (\Delta w)^2}{((\Delta w)^2+\gamma_a^2)^3} \approx -\frac{2b}{L(\Delta w)^3}$ and we get the condition

$$b = \frac{\pi \left|\Delta w\right|^3}{2a\delta^2}, \tag{5.13}$$

from which the length of the absorber can be extracted. Fig.40 gives the time-dependence of the transmitted radiation intensity, calculated according to the general expression Eq.(5.9), which gives the same result as the simplified formula Eq.(5.12).

As can be seen, instead of the familiar monotonically decaying exponential it is a sequence of pulses with maximum amplitude decaying exponentially within a characteristic time equal to the lifetime of the excited state of an emitting nucleus. This time dependence can be observed using the coincidence technique [51]. In the coincidence technique a ^{57}Fe nucleus in the excited state is formed as a result of a cascade decay of a parent nucleus ^{57}Co, in the last cascade process a gamma quantum of 122 keV is emitted. This photon serves as a precursor, giving the time of the excited state formation. A detector is switched on at this moment and waits for

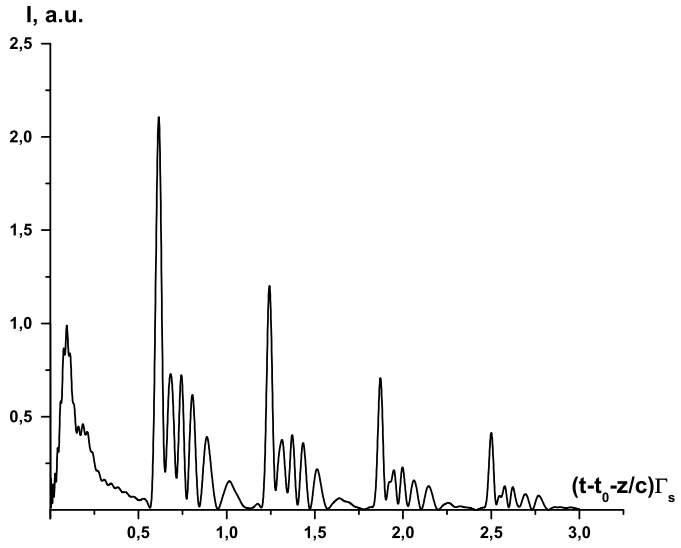

Fig. 40. Time-dependence of the intensity of a "compressed" single photon.

the 14.4 keV gamma quantum. Once it is detected, the detector is switched off, and the procedure is repeated. In this way the time distribution between the two gamma photons is measured resulting in the decay profile of the excited state of the nucleus. This technique has to be modified, though, in order to observe the decay curve shown in Fig.40. The reason is that this decay process can be measured only if the excited nuclei emit photons in the same phase of the source's vibration. Since the spontaneous emission time is not correlated with the source movement, the photons can be emitted at any phase of vibration. To obtain the decay shown in Fig.40 it is necessary, therefore, to tie the time of excited state formation to some particular phase. It can be done by subtracting for every decay event from the time between the precursor and 14.4 keV photon detection the time difference between the actual decay time and the next nearest moment the phase goes through the reference value. Another type of experiment can be envisaged in which the time of excited

state formation is not known, so the intensity has to be averaged over t_0. In this case the measurement time is not synchronized with formation of the excited state of a nucleus, but with the phase of source motion, as in conventional Doppler-scan Mössbauer measurements.

If we take into account both recoilless and recoiled parts of emitted radiation, the intensity is given by the following expression:

$$I(t,L) = I_0 \Big(1 - 2f_s b \cdot Re \Big[e^{-ia\sin(\delta(t-z/c)+\phi)} \int_0^\infty e^{-i\Delta w t' - (\gamma_a+\Gamma_s/2)t' + ia\sin(\delta(t-t'-z/c)+\phi)}\sigma(bt')dt'\Big]$$
$$+2f_s b^2 \cdot Re\left[\int_0^\infty dt\prime e^{i\Delta w t\prime - ia\sin(\delta(t-t'-z/c+\varphi)+(\Gamma_s/2-\gamma_a)t'}\sigma(bt') \int_{t\prime}^\infty dt'' e^{-i\Delta w t'' + ia\sin(\delta(t-t''-z/c)+\varphi)-(\Gamma_s/2+\gamma_a)t''}\sigma(bt'')\right]\Big), \quad (5.14)$$

where I_0 is the off-resonance intensity. Typical intensity time-dependence, calculated using (5.14), is shown in Fig.41.

Now let us make numerical estimates of the optimal length of the absorber and the duration of a single pulse achievable with this technique. As an example we consider ^{57}Fe resonance assuming both the absorber and the source be single-line. From Eq.(5.6) $b = 2\pi\mu_{21}^2 k_s N\ f_a L/\hbar = 3\pi N\ f_a L\Gamma_s/2k_s^2(1+\alpha)$, where α is the internal conversion coefficient. The optimal b is given by Eq.(5.13), the optimal lenght is then:

$$L_{opt} = \frac{|\Delta w|^3 k_s^2(1+\alpha)}{3a\delta^2 N\ f_a\Gamma_s} = \frac{|\Delta w|^3 (\Delta E^{res})^2(1+\alpha)}{3a\delta^2 N\ f_a\Gamma_s(c\hbar)^2}$$

For the ^{57}Fe resonance $\Delta E^{res} = 14.4$ keV, the density of resonant atoms can be as high as $N = 10^{22}$ cm^{-3}, $f_a \approx 1$ up to room temperature, $\alpha \approx 9$, $\Gamma_s = 1.1$ MHz. If we detune far off-resonance such as $\Delta w = 100\Gamma_s$, and take the modulation frequency

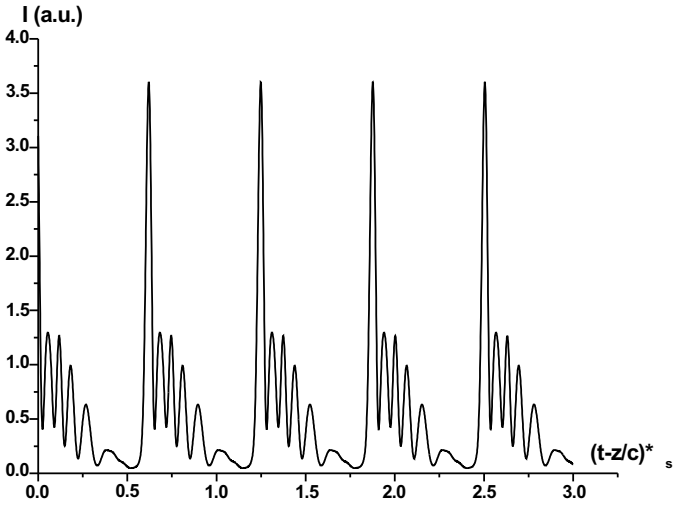

Fig. 41. Intensity of gamma radiation after averaging over t_0 - formation time of the excited state of a nucleus in a source.

be rather high as in experiments with "quantum beats of recoilles gamma radiation" [137] $\delta = 10\Gamma_s$, so that $a = 10$ sidebands are generated, then the optimal length $L_{opt} \sim 1$ mm. At this length the pulse duration would be $T_{pulse} \sim 1/2a\delta \approx 0.7$ ns which is two orders of magnitude shorter than the decay time of the excited state of the ^{57}Fe nucleus (100 ns).

Nonresonant losses become significant for an absorber of such thickness. For energies corresponding to Mössbauer transitions $(10 - 100$ keV) they will be almost entirely due to electric dipole contribution to photoelectric absorption. For example, for stainless steel fully enriched in ^{57}Fe the electronic absorption coefficient $\gamma \approx 0.05$ μm^{-1} [143], which leads to intensity attenuation by a factor of $exp(-50)$ for 1 mm thickness. As a result no radiation would penetrate through the absorber. The attenuation coefficient although can be reduced by as much as two orders of magnitude if one makes use of the Borrmann effect [153]. This effect takes place in the so-called

Laue geometry, when the Bragg condition is satisfied for transmitted waves. Namely, two waves with wave vectors difference matching to some reciprocal lattice vector will be strongly reflected one into the other. Two linear combinations of the waves constitute then two eigenmodes which propagate through the crystal. The wave field of these modes consists of traveling waves along the direction of propagation (given by the sum wave vector of the two initial waves) and standing waves perpendicular to that direction. One of the eigenmodes (the Borrmann mode) has nodes of its electric field coincide with the equilibrium positions of atoms in the crystal. This has the effect of producing a gamma-ray waveguide such that gamma-rays can be transmitted through "thick" crystals with very little attunuation due to reduction of photoabsorption. At the same time the Borrmann mode will strongly couple to Mössbauer nuclei with magnetic dipole transitions since in this mode each nucleus lies in a region of strong magnetic field. This mode will couple to higher-multipole transitions as well since the electric field gradient and higher derivatives of the field are also large at nuclear sites. The other eigenmode has anti-nodes of its electric field at atoms equilibrium positions, thus it propagates with enchanced absorption. Radiation in the Borrman mode will penetrate much further in a good crystal than radiation in a non-Borrmann mode. In [154] the case of 2 mm thick ^{56}FeTi absorber is theoretically considered. Its electronic absorption lenght is $\gamma = 27.9$ μm and for $L = 2$ mm the intensity attenuation would be $\approx exp(-71.68)$. It was predicted though that in a two-beam Borrmann mode 6% of the radiation still will be transmitted through such a crystal. Another possibility is to use materials with low nonresonant losses, where the host is made of light elements, examples are $FeCl_2 \cdot (2-4)H_2O$ crystals, in which the Mössbauer effect was detectable with the sample thickness of 0.35 mm [155] and of 1 mm [156].

D. Compressor made of Bragg scattering crystals

Another possible way of compressing Mössbauer radiation into short pulses is to use a system of diffracting gratings in which photons of different energies traverse different path length in analogy to optics [157]. For gamma-rays Bragg scattering crystals such as Si, Al_2O_3, BeO, Be, noncubic polytypes of SiC can be utilized as gratings. Bragg reflection angular dispersion can be used to spatially separate energy sidebands and make them travel different paths. Dispertion relation is easily calculated from the angular and energy dependence of Bragg reflection intensity [158]. Let us assume that for some wavelength k the Bragg condition is fulfilled: $2kd\sin\theta = 2\pi$, where d is the corresponding interplanar distance. If the wavenumber slightly differs from resonant, $k + dk$, the diffraction angle will be $\theta + \delta\theta$, where

$$\frac{d\theta}{dk} = -\frac{2}{k\cot\theta} \tag{5.15}$$

In order to maximize the angular spread between adjacent sidebands large Bragg angles are preferred. Schematic of the proposed crystal system is shown in Fig.42a, which is almost analogous to the scheme used in [159] to construct an ultra high resolution monohromator. Here we propose to use four high-order asymmetric reflections with large asymmetry angles. First and second crystals basically do the main job, namely, they impose different phase changes on sidebands. The third crystal is a mirror reflection of the second one and together with the fourth crystal serves the purpose of reducing the beam cross-section to its original size. For the first, second and fourth crystals asymmetry angles are negative, for the third - positive. High asymmetry of the first reflection allows to achieve large angular acceptance to match the angular spread of incident radiation. Asymmetry factor of the first crystal $b_1 = \sin(\theta + \alpha_1)/\sin(\theta - \alpha_1)$ is less than unity so that angular divergence of the

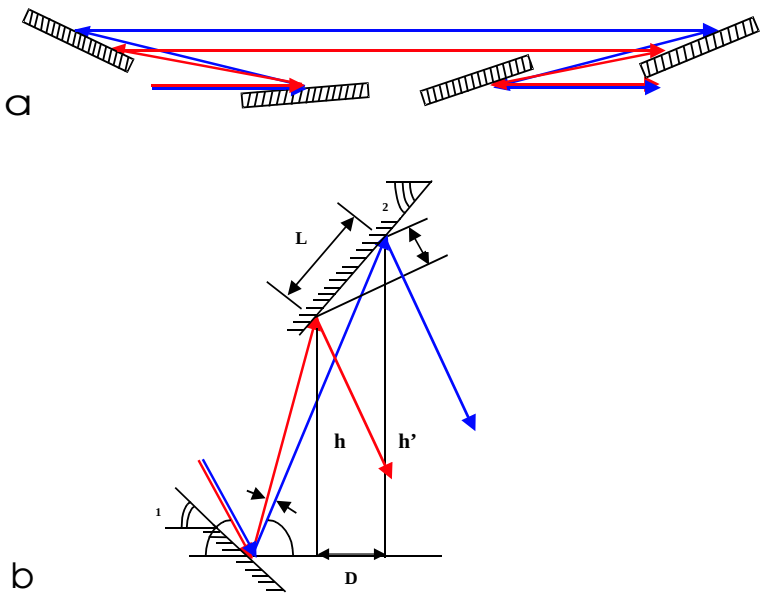

Fig. 42. Diagram illustrating the compression scheme based on a system made of four Bragg-scattering crystals and the way of making "red" and "blue" sidebands accumulate necessary for optimal compression phase difference.

reflection can be made smaller than the angular spread between adjacent energy sidebands resulting from angular dispersion of the reflection. It is well known [160] that for example in silicon crystals high order reflections at large Bragg angles have small Darwin widths on the order of a few μrad at 10 keV and they are futher reduced as energy increases. The asymmetry angle of the third crystal $\alpha_3 = -\alpha_2$, so that angular acceptance of the third reflection matches angular divergence of the second reflection. Angular divergence of the third reflection will be large, but sidebands are already spatially separated and almost phase shifted when they arrive at the third crystal. The fourth crystal has negative asymmetry angle, and angular acceptance of the fourth reflection can be adjusted to match angular divergence of the third reflection. Due to resulting small angular divergence of the fourth reflection the beam will be collimated at the exit.

As can be seen from Fig.42b the total optical path difference between "blue" and "red" sidebands is:

$$\Delta z = z_{blue} - z_{red} = 2 \cdot \left(\frac{h\prime}{\sin\theta} - \frac{h}{\sin(\theta + \delta\theta)} + \Delta \right),$$

where

$$h' = h + L\cos(\pi/2 + \alpha_2) = h - L\sin\alpha_2,$$

$$D = \frac{h'}{\tan\theta} - \frac{h}{\tan(\theta + \delta\theta)} = L\sin(\pi/2 + \alpha_2) = L\cos\alpha_2,$$

which gives

$$L = \left(\frac{h'}{\tan\theta} - \frac{h}{\tan(\theta + \delta\theta)} \right) / \cos\alpha_2,$$

$$h' = h - \tan\alpha_2 \left(\frac{h'}{\tan\theta} - \frac{h}{\tan(\theta + \delta\theta)} \right),$$

so that

$$h' = h \frac{\tan(\theta + \delta\theta) + \tan\alpha_2}{\tan\theta + \tan\alpha_2} \frac{\tan\theta}{\tan(\theta + \delta\theta)}$$

and up to the first order in $\delta\theta$:

$$h' \simeq h \left(1 - \frac{\sin\alpha_2 \delta\theta}{\sin\theta \sin(\theta + \alpha_2)} \right),$$

$$\Delta = L\cos(2(\pi/2 - \theta) + \theta + \alpha_2) =$$

$$= -\frac{\cos(\theta - \alpha_2)}{\cos\alpha_2} \left(\frac{h'}{\tan\theta} - \frac{h}{\tan(\theta + \delta\theta)} \right) = -h \frac{\cos(\theta - \alpha_2)\delta\theta}{\sin\theta \sin(\theta + \alpha_2)}.$$

Finally

$$\Delta z = -\frac{4h\sin\alpha_2\delta\theta}{\sin(\theta + \alpha_2)} = \frac{8h\tan\theta\sin\alpha_2\delta k}{k\sin(\theta + \alpha_2)} = \frac{8h\sin\theta\sin\alpha_2\delta w}{w\cos\theta\sin(\theta + \alpha_2)},$$

where we used dispersion relation Eq.(5.15).

The field at the entrance to the crystal system is given by Eq.(5.4), at the exit

of the system it becomes:

$$E_s(t,z) \sim \sum_{n=-\infty}^{\infty} J_n(a) e^{-iw_n t + ik_n(z+\Delta z_n) - \Gamma_s(t-t_0-z/c)/2} \theta(t-t_0-z/c) + c.c.,$$

where the path difference between n'th and central sideband is

$$\Delta z_n = -\frac{8h \sin\alpha_2 \sin\theta \, dw_n}{w_s \sin(\theta+\alpha_2)\cos\theta} = -\frac{8h \sin\alpha_2 \sin\theta \, n\delta}{w_s \sin(\theta+\alpha_2)\cos\theta}.$$

It leads to the following expression for the field:

$$E_s(t,z) \sim e^{-iw_s t + ik_s z - \Gamma_s(t-t_0-z/c)/2} \theta(t-t_0-z/c) \times$$

$$\times \sum_{n=-\infty}^{\infty} J_n(a) e^{-in\delta(t-z/c+\frac{8h\sin\alpha_2\sin\theta}{c\sin(\theta+\alpha_2)\cos\theta}) - i(n\delta)^2 \frac{8h\sin\alpha_2\sin\theta}{w_s c\sin(\theta+\alpha_2)\cos\theta}} + c.c.$$

Applying the same requirement for optimal compression that a "red" sideband, which reaches the first crystal with a delay π/δ compared to a "blue" sideband, leaves the system of crystals simultaneously with the "blue" one, we get the condition:

$$z_{blue} - z_{red} = \frac{8h\,|\sin\alpha_2|\sin\theta\, 2a\delta}{w_s \sin(\theta+\alpha_2)\cos\theta} = c\frac{\pi}{\delta}.$$

It determines the characteristic size of the crystal system:

$$h = \frac{\pi c w_s}{16\delta^2 a} \frac{\sin(\theta+\alpha_2)\cos\theta}{|\sin\alpha_2|\sin\theta}, \tag{5.16}$$

$$L = \frac{\pi c}{4\delta\,|\sin\alpha_2|\sin\theta}. \tag{5.17}$$

The intensity of recoilless radiation after it leaves the crystal system is given by the expression:

$$I_{recoilless}(t,z) \sim \left| \sum_{n=-\infty}^{\infty} J_n(a) e^{-in\delta(t-z/c+\frac{8h\sin\alpha_2\sin\theta}{c\sin(\theta+\alpha_3)\cos\theta}) - i(n\delta)^2 \frac{8h\sin\alpha_2\sin\theta}{w_s c\sin(\theta+\alpha_2)\cos\theta}} \right|^2.$$

Now let us again consider the ^{57}Fe example. For numerical estimates we assume that the maximal vibrational velocity of the source is $V_{max} \sim 1$ m/s, which was

achieved for $LiNbO_3$ single crystal transducer [161], and the vibrational frequency is $\delta \sim 1$ GHz. Single crystal transducers cannot provide such high frequency of vibration, but it can be easily achieved in acoustic superlattices made of $LiNbO_3$ [162]. We also assume the following parameters of the compression system: $\theta = \pi/2 - \Delta\theta$, $\theta + \alpha_2 \approx \Delta\theta$, where $\Delta\theta \ll 1$, so that the incident radiation is almost backscattered. The asymmetry angle of the first crystal need not be as large as of the second one, the only requirement is that angular divergence of the first reflection should be less than the angular spread between adjacent sidebands. From (5.15) $\delta\theta_{adj} = 2\delta/(w_s \cot\theta)$ and if we assume $\Delta\theta \sim 1$ mrad, we get $\delta\theta_{adj} \approx 0.6$ μrad. Any α_1 which would give narrower angular divergence will suffice. The characteristic size of the system for these parameters is according to Eqs.(5.16), (5.17):

$$h \approx \frac{\pi c^2 (\Delta\theta)^2}{16\delta V_{max}},$$

$$L \approx \frac{\pi c}{4\delta}.$$

The higher the modulation frequency δ, the smaller the size of the crystal system. For $\delta = 1$ GHz, the length of the second crystal is $L = 3.75$ cm, and the separation between the first and the second crystals is $h \approx 3$ m. In this case $a = 12$ sidebands will be generated and the pulse duration will be $T_{pulse} \sim 1/2a\delta \sim 7$ ps.

The numerically calculated time dependence of compressed Mossbauer radiation at the exit of the crystal system for ^{57}Fe is shown in Fig.43. The pulse duration is 30 ps, the size of the crystal system required for optimal compression is $h \approx 1$ m. The difference in the theoretically predicted and numerically calculated size h required for optimal compression is most probably due to the sinusoidal modulation of the frequency. The expression (5.16) for the optimal size was calculated assuming linear frequency chirp since the compression system with linear group velocity dispersion

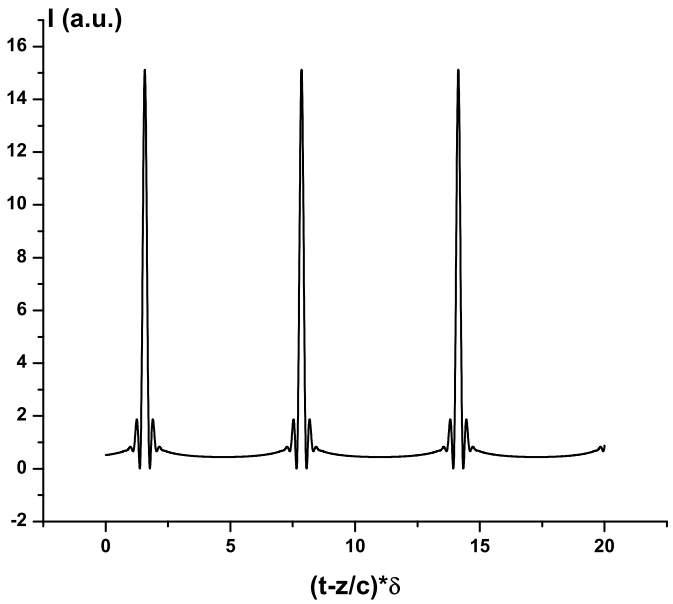

Fig. 43. Time dependence of recoilless radiation passed through the crystal system, depicted in Fig.4.

provides optimal compression for signals with linear frequency chirp.

E. Discussion

Coherent radiation in the hard X-ray and gamma range due to its extremely short wavelength (less than 1 Å) may have a lot of applications. It could establish new records in all areas where high precision and high spatial resolution is required: spectroscopy, crystallography, microscopy, lithography, holography, optical tomography, etc. If this radiation is delivered in the form of coherent short pulses, this may allow one to perform time-resolved measurements of structure dynamics at a single atom level with temporal resolution determined by the duration of a pulse.

Recently developed ultrashort pulse X-ray sources [163, 164] are used in a number of fields to study material properties, chemical and biological reactions on time scales up to picoseconds [165]. Novel sources based on generation of harmonics of femtosecond laser radiation in gases are limited in wavelength from below by 10 nm.

Synchrotrons and laser synchrotron radiation sources [164, 166] are able to produce high flux and high brightness ultrashort X-ray pulses with broad spectral width, typically $\Delta E/E \sim 1 \div 10\%$, but it is not coherent. Coherent radiation can be obtained from a synchrotron using frequency filters or forward scattering by a Mössbauer absorber, but not in the form of ultra-short pulses.

The method that is proposed in the project would provide a compact, laboratory-scale, near-monochromatic (with neV spectral width), low-cost, source of short (sub-nanosecond scale) pulses of gamma radiation. In comparison with synchrotron radiation the advantage of the proposed technique is a better control over the phase of coherent pulses. Ideally, pulses can be transform-limited. It is also worth noting that due to discrete nature of Mössbauer radiation the proposed technique offers a

fascinating possibility of manipulation of spectral properties of a single gamma photon. Namely, a photon can be temporarily compressed into a sequence of short pulses whose amplitude decays exponentially within a Mössbauer transition excited state lifetime.

CHAPTER VI

SUMMARY

The main goal of the work was to extend atomic and molecular interference phenomena most intensively studied in alkali vapors to new media, such as rare-earth and transition metal ion doped crystals and plasma, and to find new applications. The main results of this work are the following:

1. We proposed to apply the coherent population trapping effect to measure magnetic fields in a plasma, medium which is less used and studied in EIT/CPT experiments in comparison with alkali vapors. A theoretical analysis and a demonstration experiment performed in a neon discharge show the ability of the proposed technique to measure both the strength and the orientation of the field. The technique might be applicable to both cold and hot plasma configurations.

2. We extended the theory of atomic and molecular interference and coherence phenomena from gaseous to solid materials and analyzed the behavior of the EIT resonance (its width and contrast), as well as the achievable group velocity of light and efficiency of non-linear interactions in solid media with a long-lived spin coherence. Estimates of the parameters of the resonance and required driving field intensity are given for a particular class of materials, namely, rare-earth and transition metal ion doped crystals, known to have narrow both optical and spin transitions. For these materials required driving field intensities are in the range $1 - 10^3$ W/cm^2 compared to $1 - 100$ mW/cm^2 in gaseous media, but due to high density of ions the efficiency of EIT/CPT based non-linear interactions can be as high as in gases.

3. We proposed a technique of suppression of excited-state absorption in laser crystals, using the electromagnetically induced transparency effect. The technique may be useful for obtaining tunable laser action in ultraviolet range in rare-earth

ion doped crystals. Estimates of the control field intensity required for efficient ESA suppression were made for these crystals, showing that the technique is feasible in a pulsed regime. Numerical and analytical analysis of the weak probe pulse amplification in a crystal with ESA, suppressed by a pulsed strong control field, shows that pulses of picosecond duration with peak intensity of several tens gigawatts per cm^2 can be obtained at the length of the crystal of several cm.

4. We analyzed theoretically the possibility to extend the chirped pulse compression technique from the visible to gamma range of frequencies which may be used for production of ultrashort pulses of Mössbauer radiation. In a compressor, providing necessary group velocity dispersion, made of a far-detuned resonant Mössbauer absorber, pulses of sub-nanosecond duration can be obtained. With a system of Bragg scattering crystals used to provide the dispersion pulses of several tens picoseconds are feasible.

REFERENCES

[1] R.W. Wood, and A. Ellet, Proc. R. Soc. London Ser. A, **102**, 190 (1923); Phys. Rev., **24**, 243 (1924).

[2] W. Hanle, Z. Phys., **30**, 93 (1924).

[3] G. Moruzzi and F. Strumia, editors, *The Hanle Effect and Level-Crossing Spectroscopy*, (Plenum Press, New York, 1991).

[4] S.L. McCall, and E.L. Hahn, Phys. Rev. Lett., **18**, 908 (1967).

[5] E.L. Hahn, Phys. Rev., **80**, 580 (1950).

[6] N.A. Kurnit, I.D. Abella, S.R. Hartmann, Phys. Rev. Lett., **13**, 567 (1964).

[7] S.P. Hartmann, IEEE J. Quantum Electron., **4**, 802 (1998); P. Hu, S. Geschwind, T.M. Jedju, Phys. Rev. Lett., **37**, 1357 (1976).

[8] G.W. Series, Phys. Rev., **136**, A684 (1964); S. Baskin, W.S. Bichel, D. Fink, and R.K. Wangsness, Phys. Rev. Lett., **15**, 284 (1965).

[9] R.L. Shoemaker, and R.G. Brewer, Phys. Rev. Lett., **28**, 1430 (1972); R.G. Brewer, and E.L. Hahn, Phys. Rev. A, **8**, 464 (1973).

[10] U. Fano, Phys. Rev., **124**, 1866 (1961).

[11] N.C. Wong, E.S. Kintzer, J. Mlynek, R.G. DeVoe, R.G. Brewer, Phys. Rev. B, **28**, 4993 (1983).

[12] K. Chiang, E.A. Whittaker, and S.R. Hartmann, Phys. Rev. B, **23**, 6142 (1981).

[13] B.S. Mathur, H. Tang, R. Bulos, and W. Happer, Phys. Rev. Lett., **21**, 1035 (1968).

[14] J. Mlynek, K.H. Drake, G. Kersten, D. Frölich, and W. Lange, Opt. Lett., **6**, 87 (1981).

[15] G. Alzetta, A. Gozzini, L. Moi, and G. Orriols, Nuovo Cimento B, **36**, 5 (1976); H.R. Gray, R.M. Whitley, and C.R. Stroud, Jr., Opt. Lett., **3**, 218 (1978).

[16] O. Kocharovskaya, Y.I. Khanin, JETP Lett., **48**, 630 (1988); M.O. Scully, S.-Y. Zhu, A. Gavrielides, Phys. Rev. Lett., **62**, 2813 (1989); S.E. Harris, Phys. Rev. Lett., **62**, 1033 (1989).

[17] O. Kocharovskaya and Y.I. Khanin, Zh. Eksp. Theor. Fiz., **90**, 1610 (1986); O. Kocharovskaya, and P. Mandel, Phys. Rev. A, **42**, 523 (1990); K.-J. Boller, A. Imamoglu, S.E. Harris, Phys. Rev. Lett., **66**, 2593 (1991); J.E. Field, K.H. Hahn, S.E. Harris, Phys. Rev. Lett., **67**, 3062 (1991).

[18] S.E. Harris, Phys. Today, **50**, 36 (1997); J.P. Marangos, J. Mod. Opt., **45**, 471 (1998).

[19] Y.I. Heller, A.K. Popov, Opt. Commun., **18**, 7 (1976); Y.I. Heller, V.F. Lukinykh, A.K. Popov, and V.V. Slabko, Phys. Lett. A, **82**, 4 (1981).

[20] P.L. Knight, M.A. Lauder, and B.J. Dulton, Phys. Rep., **190**, 1 (1990).

[21] M.O. Scully, Phys. Rep., **219** , 191 (1992).

[22] E. Arimondo, in *Progress in Optics XXXV*, edited by E. Wolf (Elsevier Science, Amsterdam, 1996), p. 257-354.

[23] K. Bergmann, H. Theuer, and B.W. Shore, Rev. Mod. Phys., **70**, 1003 (1998).

[24] A. Kasapi, M. Jain, G.Y. Yin, S.E. Harris, Phys. Rev. Lett., **74**, 2447 (1995); L.V. Hau, S.E. Harris, Z. Dutton, C.H. Behroozi, Nature (London), **397**, 594 (1999); D. Budker, D.F. Kimball, S.M. Rochester, V.V. Yashchuk, Phys. Rev. Lett., **83**, 1767 (1999); M.M. Kash, V.A. Sautenkov, A.S. Zibrov, L. Hollberg, G.R. Welch, *et al.*, Phys. Rev. Lett., **82**, 5229 (1999); S. Inouye, R.F. Low, S. Gupta, T. Pfau, A. Gorlitz, *et al.*, Phys. Rev. Lett., **85**, 4225 (2000); A.V. Turukhin, V.S. Sudarshanam, M.S. Shahriar, J.A. Musser, B.S. Ham, and P.R. Hemmer, Phys. Rev. Lett., **88**, 023602 (2002).

[25] O. Kocharovskaya, Yu. Rostovtsev, M.O. Scully, Phys. Rev. Lett., **86**, 628 (2001); D. Strekalov, A.B. Matsko, N. Yu, L. Maleki, Phys. Rev. Lett., **93**, 023601 (2004).

[26] C. Liu, Z. Dutton, C.H. Behroozi, L.V. Hau, Nature (London), **409**, 490 (2001); D.F. Phillips, A. Fleischhauer, A. Mair, R.L. Walsworth, M.D. Lukin, Phys.Rev.Lett., **86**, 783 (2001); M.D. Lukin, Rev. Mod. Phys., **75**, 457 (2003).

[27] L.D. Landau and E.M. Lifshitz, *Electrodynamics of Continuous Media*, Teoreticheskaya fizika (Izd. 2-e), Vol. 8, 2nd rev. and enl. edition, (Butterworth-Heinemann, Oxford, 1995).

[28] S.E. Harris, J.E. Field, A. Kasapi, Phys. Rev. A, **46**, R29 (1992).

[29] S.E. Harris, J.E. Field, and A. Imamoglu, Phys. Rev. Lett., **64**, 1107 (1990).

[30] S.E. Harris, L.V. Hau, Phys. Rev. Lett., **82**, 4611 (1999).

[31] K. Hakuta, L. Marmet, and B.P. Stoicheff, Phys. Rev. Lett., **66**, 596 (1991).

[32] G.S. Agarwal, and S.P. Tewari, Phys. Rev. Lett., **70**, 1417 (1993); A.J. Merriam, S.J. Sharpe, H. Xia, D. Manuszak, G.Y. Yin, and S.E. Harris, Opt. Lett.,

24, 625 (1999); C. Dorman, I. Kucukkara, and J.P. Marangos, Phys. Rev. A, **61**, 013802 (1999).

[33] M.D. Lukin, P.R. Hemmer, M. Loffler, M.O. Scully, Phys. Rev. Lett., **81**, 2675 (1998); B.S. Ham, P.R. Hemmer, M.S. Shahriar, Phys. Rev. A, **59**, R2583 (1999).

[34] Y.Q. Li and M. Xiao, Opt.Lett., **21**, 1064 (1996); B. Lu, W.H. Burkett, and M. Xiao, Opt.Lett., **23**, 804 (1998).

[35] D.A. Braje, V. Balic, S. Goda, G.Y. Yin, and S.E. Harris, Phys. Rev. Lett., **93**, 183601 (2004).

[36] H. Schmidt, A. Imamoglu, Opt. Lett., **21**, 1936 (1996); H. Wang, D. Goorsky, and M. Xiao, Phys. Rev. Lett., **87**, 073601 (2001).

[37] A. Imamoglu, H. Schmidt, G. Woods, M. Deutsch, Phys. Rev. Lett., **79**, 1467 (1997).

[38] M. Jain, H. Xia, G.Y. Yin, A.J. Merriam, and S.E. Harris, Phys. Rev. Lett., **77**, 4326 (1996); A.J. Merriam, S.J. Sharpe, H. Xia, D. Manuszak, G.Y. Yin, and S.E. Harris, Opt. Lett., **24**, 625 (1999).

[39] S.E. Harris and A.V. Sokolov, Phys. Rev. Lett., **81**, 2894 (1998); A.V. Sokolov, D.R. Walker, D.D. Yavuz, G.Y. Yin, and S.E. Harris, Phys. Rev. Lett., **85**, 562 (2000).

[40] M.Y. Shverdin, D.R. Walker, D.D. Yavuz, G.Y. Yin, and S.E. Harris, Phys. Rev. Lett., **94**, 033904 (2005).

[41] V.G. Arkhipkin, Yu.I. Heller, Phys. Lett. A, **98**, 12 (1983).

[42] O. Kocharovskaya, Phys. Rep., **219** , 175 (1992); G.G. Padmabandu, G.R. Welch, I.N. Shubin, E.S. Fry, D.E. Nikonov, M.D. Lukin, *et al.*, Phys. Rev. Lett., **76**, 2053 (1996); O. Kocharovskaya, R. Kolesov, Yu. Rostovtsev, Laser Phys., **9**, 745 (1999); J. Mompart and R. Corbalan, J. Opt. B: Quantum Semiclass. Opt., **2**, R7 (2000).

[43] M.O. Scully, Phys. Rev. Lett., **67**, 1855 (1991); A.S. Zibrov, M.D. Lukin, L. Hollberg, D.E. Nikonov, M.O. Scully, H.G. Robinson, V.L. Velichansky, Phys. Rev. Lett., **76**, 3935 (1996).

[44] R. Wynands, and A. Nagel, Appl. Phys. B, **68**, 1 (1999); S. Knappe, R. Wynands, J. Kitching, H.G. Robinson, and L. Hollberg, J. Opt. Soc. Am. B, **18**, 1545 (2001); S. Knappe, V. Shah, P.D.D. Schwindt, L. Hollberg, J. Kitching, L.-A. Liew, and J. Moreland, Appl. Phys. Lett., **85**, 1460 (2004).

[45] M.O. Scully, and M. Fleischhauer, Phys. Rev. Lett., **69**, 1360 (1992); D. Budker, V.V. Yashchuck, and M. Zolotorev, Phys. Rev. Lett., **81**, 5788 (1998); A. Nagel, L. Graf, A. Naumov, E. Mariotti, V. Biancalana, D. Meschede, and R. Wynands, Europhys. Lett., **44**, 31 (1998); I. Novikova, A.B. Matsko, G.R. Welch, Opt. Lett., **26**, 1016 (2001); D. Budker, W. Gawlik, D.F. Kimball, S.M. Rochester, V.V. Yashchuk, A. Weis, Rev. Mod. Phys., **74**, 1153 (2002).

[46] G.T. Trammel, J.P. Hannon, Phys. Rev. B, **18**, 165 (1978); E. Gerdau, R. Rüffer, R. Hollatz, J.P. Hannon, Phys. Rev. Lett., **57**, 1141 (1986).

[47] Yu. V. Shvyd'ko, T. Hertrich, U. van Bürck, E. Gerdau, O. Leupold, J. Metge, H.D. Rüter, S. Schwendy, G.V. Smirnov, W. Potzel, and P. Schindelmann, Phys. Rev. Lett., **77**, 3232 (1996).

[48] F. Vagizov, Hyperf. Int., **61**, 1359 (1990); I. Tittonen, P. Helisto, M. Lippmaa, and T. Katila, Hyperf. Int., **71**, 1465 (1992).

[49] R. Coussement, Y. Rostovtsev, J. Odeurs, G. Neyens, H. Muramatsu, S. Gheysen, R. Callens, K. Vyvey, G. Kozyreff, P. Mandel, R. Shakhmuratov, and O. Kocharovskaya, Phys. Rev. Lett., **89**, 107601 (2002).

[50] O. Kocharovskaya, R. Kolesov, Y. Rostovtsev, Phys. Rev. Lett., **82**, 3593 (1999).

[51] P. Helisto, I. Tittonen, M. Lippmaa, and T. Katila, Phys. Rev. Lett., **66**, 2037 (1991); I. Tittonen, M. Lippmaa, P. Helisto, T. Katila, Phys. Rev. B, **47**, 7840 (1993).

[52] Yu. Kagan, A.M. Afanas'ev, and V.G. Kohn, J. Phys. C: Solid State Phys., **12**, 615 (1979).

[53] Yu. Kagan, and A.M. Afanas'ev, in *Proceedings of International Atomic Energy Agency Symposium on Mossbauer Spectroscopy and Applications*, (IAEA, Vienna, 1972), p. 143.

[54] G.T. Trammel, and J.P. Hannon, Phys. Rev. B, **18**, 165 (1978); J.P. Hannon, and G.T. Trammell, Hyperf. Int., **123**, 127 (1999).

[55] M. Hämäläinen, R. Hari, R. Ilmoniemi, J. Knuutila, and O.V. Lounasmaa, Rev. Mod. Phys., **65**, 413 (1993).

[56] A.L. Bloom, Appl. Opt., **1**, 61 (1962); E.B. Alexandrov, and V.A. Bonch-Bruevich, Optical Engin., **31**, 711 (1992); E.B. Alexandrov, V.A. Bonch-Bruevich, and N.N. Yacobson, Sov. J. Opt. Technol., **60**, 754 (1993).

[57] D. Budker, D.F. Kimball, S.M. Rochester, V.V. Yashchuk, and M. Zolotorev, Phys. Rev. A, **62**, 043403 (2000); I.K. Kominis, T.W. Kornack, J.C. Allred, and M.V. Romalis, Nature (London), **422**, 596 (2003).

[58] P.D.D. Schwindt, S. Knappe, V. Shah, L. Hollberg, J. Kitching, L.-A. Liew, and J. Moreland, Appl. Phys. Lett., **85**, 6409 (2004).

[59] I.H. Hutchinson, *Principles of Plasma Diagnostics* (Cambridge University Press, Cambridge, United Kingdom, 2002).

[60] K. Muraoka, M. Maeda, *Laser-Induced Diagnostics of Plasmas and Gases* (Institute of Physics Publishing, Bristol, 2001).

[61] P.M. Anisimov, R.A. Akhmedzhanov, I.V. Zelensky, R.L. Kolesov, E.A. Kuznetsova, JETP, **123**, 912 (2003) [ZhETF **96**, 801 (2003)].

[62] R. Akhmedzhanov, I. Zelensky, R. Kolesov, E. Kuznetsova, Phys. Rev. E, **69**, 036409 (2004).

[63] H. Asahi, K. Motomura, K.-I. Harada, and M. Mitsunaga, Opt. Lett., **28**, 1153 (2003).

[64] E. Kuznetsova, O. Kocharovskaya, P. Hemmer, and M.O. Scully, Phys. Rev. A, **66**, 063802 (2002).

[65] T. Udem, A. Huber, B. Gross, J. Reichert, M. Prevedelli, *et al.*, Phys. Rev. Lett. **79**, 2646 (1997); J. Reichert, M. Niering, R. Hozwarth, M. Weitz, T. Udem, *et al.*, Phys. Rev. Lett. **84**, 3232 (2000).

[66] R.J. McLean, R.J. Ballagh, and D.M. Warrington, J. Phys. B: At. Mol. Phys., **18**, 2371 (1985).

[67] I.I. Sobelman, L.A. Vainshtein, E.A. Yukov, *Excitation of Atoms and Broadening of Spectral Lines* (Springer-Verlag, New York, 1981).

[68] V.E. Golant, A.P. Zhilinsky, S.A. Sakharov, *Fundamentals of Plasma Physics* (Wiley, New York, 1980).

[69] Y. Zhao, C. Wu, B.-S. Ham, M.K. Kim, and E. Awad, Phys. Rev. Lett., **79**, 641 (1997).

[70] B.-S. Ham, S.M. Shahriar, and P.R. Hemmer, Opt. Lett., **22**, 1138 (1997); B.-S. Ham, S.M. Shahriar, M.K. Kim, and P.R. Hemmer, Opt. Lett., **22**, 1849 (1997).

[71] B.-S. Ham, P.R. Hemmer, S.M. Shahriar, Opt. Commun., **144**, 227 (1997).

[72] K.Yamamoto, K. Ichimura, N. Gemma, Phys. Rev. A, **58**, 2460 (1998).

[73] K. Yamamoto, K. Ichimura, N. Gemma, Phys. Rev. A, **58**, 4116 (1998).

[74] B.-S. Ham, S.M. Shahriar, P.R. Hemmer, J. Opt. Soc. Am. B, **16**, 801 (1999).

[75] C. Wei, N.B. Manson, Phys. Rev. A, **60**, 2540 (1999); C. Wei, N.B. Manson, J. Opt. B: Quantum Semiclassical Opt., **1**, 464 (1999).

[76] P.R. Hemmer, A. Turukhin, S.M. Shahriar, J. Musser, Opt. Lett., **26**, 361 (2001).

[77] G.B. Serapiglia, E. Paspalakis, C. Sirtori, K.L. Vodopyanov, C.C. Phillips, Phys. Rev. Lett., **84**, 1019 (2000).

[78] H. Schmidt, K.L. Campman, A.C. Gossard, and A. Imamoglu, Appl. Phys. Lett., **70**, 3455 (1997); J. Faist, F. Capasso, C. Sartori, K.W. West, and L.N. Pfeiffer, Nature, **390**, 589 (1997).

[79] M. Phillips, and H. Wand, Phys. Rev. Lett., **89**, 186401 (2002); M.C. Phillips, H. Wang, I. Rumyantsev, N.H. Kwong, R. Takayama, and R. Binder, Phys. Rev. Lett., **91**, 183602 (2003).

[80] R.W. Boyd, and D.J. Gauthier, in *Progress in Optics XXXXIII*, edited by E. Wolf (Elsevier Science, Amsterdam, 2002), p. 497-529.

[81] A. Javan, O. Kocharovskaya, H. Lee, and M.O. Scully, Phys. Rev. A, **66**, 015802 (2002).

[82] M.S. Feld and A. Javan, Phys. Rev., **177**, 540 (1969).

[83] A.V. Taichenachev, A.M. Tumakin, and V.I. Yudin, JETP Letters, **72**, 119 (2000).

[84] M.D. Lukin, M. Fleischhauer, A.S. Zibrov, H.G. Robinson, V.L. Velichansky, L. Hollberg, and M.O. Scully, Phys. Rev. Lett., **79**, 2959 (1997).

[85] P.A. Tanner, C.S.K. Mak, and M.D. Faucher, Chem. Phys. Lett., **343**, 309 (2001).

[86] D. Piehler, and N. Edelstein, Phys. Rev. A, **41**, 6406 (1990); D. Van Der Voort, and G. Blasse, J. Sol. State Chem., **87**, 350 (1990).

[87] D.M. Boye, R.M. Macfarlane, Y. Sun, and R.S. Meltzer, Phys. Rev. B, **54**, 6263 (1996); S. Lizzo, A.H. Velders, A. Meijerink, G.J. Dirksen, and G. Blasse, J. Lum., **65**, 303 (1996).

[88] T. Hoshina and S. Kuboniwa, J. Phys. Soc. Jpn., **31**, 828 (1971).

[89] G.J. Pryde, M.J. Sellars, and N.B. Manson, Phys. Rev. Lett., **84**, 1152 (2000).

[90] I.T. Jacobs, G.D. Jones, K. Zdansky, and R.A. Satten, Phys. Rev. B, **3**, 2888 (1971); M.H. Crozier, Phys. Rev., **137**, A1781 (1965).

[91] T. Yosida, M. Yamaga, D. Lee, T.P.J. Han, H.G. Gallagher, and B. Henderson, J. Phys.: Condens. Matter, **9**, 3733 (1997).

[92] J.M. Baker, and F.I.B. Williams, Proc. R. Soc. London Sect. A, **257**, 283 (1962).

[93] L. Biyikli, and Z. Hasan, J. Lum., **83/84**, 373 (1999).

[94] Z. Hasan, L. Biyikli, and P.I. Macfarlane, Appl. Phys. Lett., **72**, 3399 (1998).

[95] R.M. Macfarlane, and J.C. Vial, Phys. Rev. B, **36**, 3511 (1987).

[96] L.E. Erickson, Phys. Rev. B, **16**, 4731 (1977).

[97] S. Kück, Appl. Phys. B, **72**, 515 (2001).

[98] D.J. Ehrlich, P.F. Moulton, R.M. Osgood, Opt. Lett., **4(6)**, 184 (1979); D.J. Ehrlich, P.F. Moulton, R.M. Osgood, Opt. Lett., **5(8)**, 339 (1980); M.A. Dubinskii, V.V. Semashko, A.K. Naumov, R.Yu. Abdulsabirov, and S.L. Korableva, Laser Phys., **3(1)**, 216 (1993); C.D. Marshall, J.A. Speth, S.A. Payne, W.F. Krupke, G.J. Quarles, V. Castillo, B.H.T. Chai, J. Opt. Soc. Am. B, **11(10)**, 2054 (1994).

[99] R.W. Waynant, Appl. Phys. B, **28**, 205 (1982); R.W. Waynant and P.H. Klein, Appl. Phys. Lett., **46**, 14 (1985).

[100] M.F. Joubert, and R. Moncorge, Opt. Mater., **22**, 95 (2003).

[101] S. Nicolas, M. Laroche, S. Girard, et al., J. Phys.: Condens. Matter, **11**, 7937 (1999).

[102] Y.M. Cheung and S.K. Gayen, Phys. Rev. B, **49**, 14827 (1994).

[103] D.S. Hamilton, S.K. Gayen, G.J. Pogatshnik, R.D. Ghen, W.J. Miniscalo, Phys. Rev. B, **39**, 8807 (1989).

[104] S. Lizzo, A. Meijerink, G.J. Dirksen, and G. Blasse, J. Lum., **63**, 223 (1995).

[105] J.K. Lawson and S.A. Payne, Opt. Materials, **2**, 225 (1993).

[106] S.A. Payne, C.D. Marshall, A.J. Bayramian, and J.K. Lawson, in *Tunable Solid-State Lasers*, ed. by W.Strëek, E.ëukowiak, B. Nissen-Sobocinska, Proc. SPIE, **3176**, 68 (1997).

[107] J.S. Cashmore, S.M. Hooker, and C.E. Webb, Appl. Phys. B, **64**, 293 (1997).

[108] E. Kuznetsova, R. Kolesov, O. Kocharovskaya, Phys. Rev. A, **70**, 043801 (2004).

[109] R.C. Alig, Z.J. Kiss, J.P. Brown, and D.S. McClure, Phys. Rev., **186**, 276 (1969).

[110] G.S. Agarwal and W. Harshawardhan, Phys. Rev. Lett., **77**, 1039 (1996); M. Yan, E.G. Rickey, and Y. Zhu, Phys. Rev. A, **64**, 043807 (2001).

[111] K. Böhmer, T. Halfmann, L.P. Yatsenko, Phys. Rev. A, **66**, 013406 (2002).

[112] R.M. Macfarlane, A. Cassanho, and R.S. Meltzer, Phys. Rev. Lett., **69**, 542 (1992).

[113] R.M. Macfarlane, R.S. Meltzer, and B.Z. Malkin, Phys. Rev. B, **58**, 5692 (1998).

[114] S.K. Gayen, D.S. Hamilton, and R.H. Bartram, Phys. Rev. B, **34**, 7517 (1986).

[115] E. Sarantopoulou, A.C. Cefalas, M.A. Dubinskii, C.A. Nicolaides, R.Y. Abdulsabirov, *et al.*, Opt. Lett. **19**, 499 (1994).

[116] S. Nicolas, E. Descroix, M.F. Joubert, Y. Guyot, M. Laroche, *et al.*, Opt. Mater., **22**, 139 (2003).

[117] S. Nicolas, E. Descroix, Y. Guyot, M.F. Joubert, R.Y. Abdulsabirov, *et al.*, Opt. Mater., **16**, 233 (2001).

[118] M. Laroche, J.L. Doualan, S. Girard, J. Margerie, R. Moncorge, *et al.*, J. Opt. Soc. Am. B, **17**, 1291 (2000).

[119] S. Kück and P. Jander, Opt. Materials, **13**, 299 (1999).

[120] S. Kück and S. Hartung, Chem. Phys., **240**, 387 (1999).

[121] N.V. Kuleshov, V.G. Shcherbitsky, V.P. Mikhailov, S. Hartung, T. Danger, *et al.*, J. Lum., **71**, 265 (1997).

[122] J. Kvapil, M. Koselja, J. Kvapil, B. Perner, V. Skoda, *et al.*, Chech. J. Phys. B, **38**, 237 (1988).

[123] T. Wegner, and K. Petermann, Appl. Phys. B, **49**, 275 (1989).

[124] S.A. Basun, T. Danger, A.A. Kaplyanskii, P.S. McClure, K. Petermann, *et al.*, Phys. Rev. B, **54**, 6141 (1996).

[125] R.M. Wood, *Laser Induced Damage in Optical Materials* (Institute of Physics, Bristol, England, 2003).

[126] G.L. Lamb Jr., Rev. Mod. Phys., **43**, 99 (1971).

[127] R. Grobe, F.T. Hioe, and J.H. Eberly, Phys. Rev. Lett., **73**, 3183 (1994).

[128] M.I. Rabinovich, and D.I. Trubetskov, *Oscillation and Waves in Linear and Nonlinear Systems* (Kluwer Academic Publishers, Netherlands, 1989).

[129] F.T. Hioe, C.E. Carroll, Phys. Rev. A, **56**, 2292 (1997).

[130] N.J. Kylstra, E. Paspalakis, P.L. Knight, J. Phys. B, **31**, L719 (1998).

[131] S.E. Harris, J.E. Field, A. Kasapi, Phys. Rev. A, **46**, R29 (1992).

[132] A.B. Matsko, O. Kocharovskaya, Y. Rostovtsev, G.R. Welch, A.S. Zibrov, M.O. Scully, Adv. At. Mol. Opt. Phys., **46**, 191 (2001).

[133] M. Fleischhauer, and A.S. Manka, Phys. Rev. A, **54**, 794 (1996).

[134] A. Kasapi, M. Jain, G.Y. Yin, S.E. Harris, Phys. Rev. Lett., **74**, 2447 (1995).

[135] R.L. Mössbauer, Z. Physik, **151**, 124 (1958); R.L. Mössbauer, Z. Naturforsch., **14a**, 211 (1959).

[136] N.N. Greenwood and T.C. Gibb, *Mossbauer Spectroscopy* (Chapman and Hall, London, 1971); T.E. Granshaw, B.W. Dale, G.O. Longworth, C.E. Johnson, *Mossbauer Spectroscopy and Its Applications* (Cambridge University Press, New York, 1985).

[137] G.J. Perlow, Phys. Rev. Lett., **40**, 896 (1978).

[138] S.L. Popov, G.V. Smirnov, U. van Bürck, and W. Potzel, Europhys. Lett., **28**, 439 (1994).

[139] E. Ikonen, P. Helisto, T. Katila, and K. Riski, Phys. Rev. A, **32**, 2298 (1985).

[140] E. Ikonen, P. Helisto, J. Hietaniemi, and T. Katila, Phys. Rev. Lett., **60**, 643 (1988).

[141] W. Sturhahn, E. Gerdau, R. Hollatz, R. Rüffer, H.D. Rüten, and W. Tolksdorf, Europhys. Lett., **14**, 821 (1991).

[142] E.E. Alp, W. Sturhahn, and T. Toellner, Nucl. Instr. and Meth. in Phys. Res. B, **97**, 526 (1995).

[143] G.V. Smirnov, Hyperf. Int., **123/124**, 31 (1999).

[144] P. Helisto, and I. Tittonen, Hyperf. Int., **135**, 167 (2001).

[145] E. Ikonen, J. Hietaniemi, and T. Katila, Phys. Rev. B, **38**, 6380 (1988).

[146] E. Kuznetsova, R. Kolesov, O. Kocharovskaya, Phys. Rev. A, **68**, 043825 (2003).

[147] D. Strickland, G. Mourou, Opt. Commun., **56**, 219 (1985).

[148] T.E. Cranshaw, and P. Reivari, Proc. Phys. Soc., **90**, 1059 (1967).

[149] F.J. Lynch, R.E. Holland, and M. Hamermesh, Phys. Rev., **120**, 513 (1960).

[150] J.F. Clauser, Phys. Rev. D, **9**, 853 (1974); H. Kimble, M. Dagenais, and L. Mandel, Phys. Rev. A, **18**, 201 (1978).

[151] J. Javanainen, P. Helisto, E. Ikonen, T. Katila, Phys. Rev. Lett., **55**, 2063 (1985).

[152] J.E. Monahan, and G.J. Perlow, Phys. Rev. A, **20**, 1499 (1979).

[153] G. Borrmann, Z. Phys., **42**, 157 (1941).

[154] J.T. Hutton, J.P. Hannon, and G.T. Trammell, Phys. Rev. A, **37**, 4269 (1988).

[155] H. Spiering, S. Hösl, and H. Vogel, Phys. Stat. Solidi B, **85**, 87 (1978).

[156] Dr. R. Kolesov and Dr. F. Vagizov, Personal Communication, Department of Physics, Texas A&M University.

[157] E.B. Treacy, Phys. Lett., **28A**, 34 (1968).

[158] J.L. Amoros, M.J. Buerger, and M.C. de Amoros, *The Laue Method* (New York, Academic Press, 1975).

[159] M. Yabashi, K. Tamasaki, S. Kikuta, and T. Ishikawa, Rev. Sci. Inst., **72**, 4080 (2001).

[160] T.S. Toellner, Hyperf. Int., **125**, 3 (2000).

[161] M.K. Kurosawa, M. Chiba, and T. Higuchi, Smart. Mater. Struct., **7**, 305 (1998).

[162] Y.Y. Zhu, and N.B. Ming, J. Appl. Phys., **72**, 904 (1992).

[163] M. Drescher, M. Hentschel, R. Kienberger, G. Tempea, C. Spielmann, G.A. Reider, P.B. Corcum, F. Krauz, Science, **291**, 1923 (2001); M.M. Murnane, H.C. Kapteyn, M.D. Rosen, and R.W. Falcone, Science, **251**, 531 (1991).

[164] M. Uesaka, H. Kotaki, K. Nakajima, H. Harano, K. Kinoshita, *et al.*, Nucl. Instr. and Meth. A, **455**, 90 (2000).

[165] D.A. Reis, M.F. DeCamp, P.H. Bucksbaum, R. Clarke, E. Dufresne, M. Hertlein, R. Merlin, R. Falcone, H. Kapteyn, M.M. Murnane, J. Larsson, T. Missalla, Phys. Rev. Lett., **86**, 3072 (2001); C. Rose-Petruck, R. Jimenez, T. Guo, A. Cavalleri, C.W. Siders, F. Raksi, J.A. Squier, B.C. Walker, K.R. Wilson, C.P.J. Barty, Nature, **398**, 310 (1999); F.L. Brown, and K.R. Wilson, J. Chem. Phys., **111**, 6238 (1999); E.A. Galburt, and B.L. Stoddard, Phys.

Today, **54**, 33 (2001); V. Srajer, Z. Ren, T.-Y. Teng, M. Schmidt, T. Ursby, D. Bourgeois, C. Pradervand, W. Schildkamp, M. Wulff, K. Moffat, Biochem., **40**, 13802 (2001).

[166] R.W. Schoenlein, H.H.W. Chong, T.E. Glover, P.A. Heimann, W.P. Leemans, *et al.*, C.R. Acad. Sci. IV - Phys., **2**, 1373 (2001).

APPENDIX A

The mechanisms of inhomogeneous broadening at optical and spin transitions in solids, caused by dipole-dipole and spin-spin interactions, respectively, are essentially different from each other. In particular, inhomogeneous broadening of spin transitions typically is smaller than that of optical transitions, which is very favorable for the appearance of atomic interference effects. One has to average the susceptibility of a Λ system over the frequency distributions of one- and two-photon transitions independently:

$$\chi = \int d(\omega_{ab}) f(\omega_{ab}) \int d(\omega_{cb}) f(\omega_{cb}) \eta \left\{ \frac{\rho_{ab}}{\alpha} \right\}, \tag{A.1}$$

where ω_{ab}, ω_{cb} are the frequencies of the $a \rightarrow b$ and $c \rightarrow b$ transitions, $f(\omega_{ab(cb)})$ is the normalized frequency distribution function, ρ_{ab} is the coherence of the $a \rightarrow b$ transition induced by radiation fields, and $\eta = N\mu_{ab}^2/2\hbar$. The Rabi frequency of the probe field with frequency ν is defined by $\alpha = \mu_{ab}E_p/2\hbar$. The matrix element of the dipole moment between levels a and b is μ_{ab}, E is the probe field amplitude, and N is the atomic density.

For simplicity we model the frequency distribution with a Lorentzian function with full width at half maximu (FWHM) $2W^{ab(cb)}$ such that

$$f(\omega_{ab(cb)}) = \frac{W^{ab(cb)}/\pi}{(\Delta\omega_{ab(cb)})^2 + (W^{ab(cb)})^2}. \tag{A.2}$$

The susceptibility (A.1) can now be evaluated by two contour integrations in the complex plane. Let us first integrate over $\Delta\omega_{ab}$. We choose the lower half plane,

which contains two poles:

$$\Delta\omega_{ab} = -iW^{ab},\ -iy = -i\sqrt{\gamma^2 + \frac{\Omega^2\gamma(1+3w_{cb}/w_{ab})}{2w_{cb}}}.$$

So $\chi = \chi_1 + \chi_2$, where χ_i are the contributions from the two poles. For the pole $\Delta\omega_{ab} = -iW^{ab}$ we have

$$\chi_1 = \frac{i\eta}{2}\frac{(\gamma_{cb} + i\Delta + i\Delta\omega_{cb})(\gamma^2 + \frac{\gamma\Omega^2}{w_{cb}} + (iW^{ab} + \Delta\omega_{cb})^2) - \Omega^2(W^{ab} + \gamma - i\Delta\omega_{cb})}{[(W^{ab} + \gamma + i\Delta)(\gamma_{cb} + i\Delta + i\Delta\omega_{cb}) + \Omega^2]\,[y^2 + (iW^{ab} + \Delta\omega_{cb})^2]}.$$

The second pole $\Delta\omega_{ab} = \Delta\omega_{cb} - iy$ yields

$$\chi_2 = -\frac{i\eta}{2}\frac{W^{ab}\left[\Omega^2(y+\gamma) - (\gamma_{cb} + i\Delta + i\Delta\omega_{cb})(\gamma^2 - y^2 + \frac{\gamma\Omega^2}{w_{cb}})\right]}{y\,[(W^{ab})^2 + (\Delta\omega_{cb} - iy)^2]\,[(y + \gamma + i(\Delta + \Delta\omega_{cb}))(\gamma_{cb} + i\Delta + i\Delta\omega_{cb}) + \Omega^2]}.$$

Now we carry on an integration over $\Delta\omega_{cb}$, choosing again the lower half plane, since it contains fewer poles.

The χ_1 term contains the following poles in the lower half plane: $\Delta\omega_{cb} = -iW^{cb}$, $-i(W^{ab} + y)$ and $\Delta\omega_{cb} = -i(W^{ab} - y)$. The last one lies in the lower plane only if $y < W^{ab}$. So there will be either two or three poles, depending on the value of y.

The χ_2 term, multiplied by Eq.(A2) corresponding to the $c \to b$ transition, contains the poles: $\Delta\omega_{cb} = -iW^{cb}$ and $\Delta\omega_{cb} = -i(W^{ab} - y)$. Again, there are either two or one pole(s) in the lower half-plane depending on whether y is greater or less then W^{ab}. It turns out that the contributions to χ_1 and χ_2 from the pole $\Delta\omega_{cb} = -i(W^{ab} - y)$ when $y < W^{ab}$ exactly cancel each other, so we are left with only three terms, χ_{11} and χ_{12} stemming from the integration of χ_1, and χ_{21} resulting from the integration of χ_2, where

$$\chi_{11} = -\frac{i\eta}{2AZ_{11}}(B_{11} - \Delta^2 - i\Delta W^{ab})(C_{11} - i\Delta D_{11}),$$

$$A = y^2 - (W^{ab} - W^{cb})^2 \approx y^2 - (W^{ab})^2,$$

$$Z_{11} = \left[(\gamma + W^{ab})(\gamma_{cb} + W^{cb}) + \Omega^2 - \Delta^2\right]^2 + \Delta^2\left[\gamma + \gamma_{cb} + W^{ab} + W^{cb}\right]^2 \approx$$

$$\approx \left[W^{ab}W^{cb} + \Omega^2 - \Delta^2\right]^2 + \Delta^2(W^{ab})^2,$$

$$B_{11} = (\gamma + W^{ab})(\gamma_{cb} + W^{cb}) + \Omega^2 \approx W^{ab}W^{cb} + \Omega^2,$$

$$C_{11} = \Omega^2(\gamma + W^{ab} - W^{cb}) + (\gamma_{cb} + W^{cb})\left((W^{ab} - W^{cb})^2 - \gamma^2 - \frac{\gamma\Omega^2}{w_{cb}}\right) \approx$$

$$\approx \Omega^2 W^{ab} + W^{cb}(W^{ab})^2 - \frac{\gamma\Omega^2}{w_{cb}}W^{cb},$$

$$D_{11} = \gamma^2 + \frac{\gamma\Omega^2}{w_{cb}} - (W^{ab} - W^{cb})^2 \approx \frac{\gamma\Omega^2}{w_{cb}} - (W^{ab})^2.$$

Here the following assumptions were used: $W^{ab} >> \gamma, W^{cb}$; $W^{cb} >> \gamma_{cb}$ and $w_{ab} >> w_{cb}$. All of these inequalities typically hold for EIT experiments in solids.

The second term is

$$\chi_{12} = -\frac{i\eta W^{cb}}{2y(y + W^{ab})^2 Z_{12}}(B_{12} - \Delta^2 - i\Delta(2W^{ab} + y))(C_{12} - i\Delta D_{12}),$$

where

$$Z_{12} = \left[(\gamma + W^{ab})(y + \gamma_{cb} + W^{ab}) + \Omega^2 - \Delta^2\right]^2 + \Delta^2\left[\gamma + \gamma_{cb} + y + 2W^{ab}\right]^2 \approx$$

$$\approx \left[W^{ab}(y + W^{ab}) + \Omega^2 - \Delta^2\right]^2 + \Delta^2\left[y + 2W^{ab}\right]^2,$$

$$B_{12} = (\gamma + W^{ab})(y + \gamma_{cb} + W^{ab}) + \Omega^2 \approx W^{ab}(y + W^{ab}) + \Omega^2,$$

$$C_{12} = \Omega^2(\gamma - y) - \frac{\gamma\Omega^2}{2w_{cb}}(1 - \frac{3w_{cb}}{w_{ab}})(\gamma_{cb} + y + W^{ab}) \approx \Omega^2(\gamma - y) - \frac{\gamma\Omega^2}{2w_{cb}}(y + W^{ab}),$$

$$D_{12} = \frac{\gamma\Omega^2}{2w_{cb}}(1 - \frac{3w_{cb}}{w_{ab}}) \approx \frac{\gamma\Omega^2}{2w_{cb}}.$$

Finally,

$$\chi_{21} = -\frac{i\eta W^{ab}}{2y\left[(W^{ab})^2 - (y + W^{cb})^2\right]Z_{21}}(B_{21} - \Delta^2 - i\Delta(2W^{cb} + \gamma_{cb} + \gamma + y))(C_{21} - i\Delta D_{21}),$$

where

$$Z_{21} = \left[(\gamma + y + W^{cb})(\gamma_{cb} + W^{cb}) + \Omega^2 - \Delta^2\right]^2 + \Delta^2 \left[\gamma + \gamma_{cb} + y + 2W^{cb}\right]^2 \approx$$

$$\approx \left[(\gamma + y + W^{cb})W^{cb} + \Omega^2 - \Delta^2\right]^2 + \Delta^2 \left[\gamma + y + 2W^{cb}\right]^2,$$

$$B_{21} = (\gamma + y + W^{cb})(\gamma_{cb} + W^{cb}) + \Omega^2 \approx (\gamma + y + W^{cb})W^{cb} + \Omega^2,$$

$$C_{21} = \Omega^2(\gamma + y) - \frac{\gamma\Omega^2}{2w_{cb}}(1 - \frac{3w_{cb}}{w_{ab}})(\gamma_{cb} + W^{cb}) \approx \Omega^2(\gamma + y) - \frac{\gamma\Omega^2}{2w_{cb}}W^{cb},$$

$$D_{21} = \frac{\gamma\Omega^2}{2w_{cb}}(1 - \frac{3w_{cb}}{w_{ab}}) \approx \frac{\gamma\Omega^2}{2w_{cb}}.$$

VITA

Yelena Anatolyevna Kuznetsova

Personal Information:

Born: 1975, Nizhny Novgorod, Russia.

Address: 53 Internatsional'naya Street, Neclyudovo, Nizhegorodsky region, 606460, Russia

Employment:

1999- present Research Assistant at Texas A&M University since Sept. 99.

1996-1999 Junior Researcher at the Institute of Applied Physics, Nizhny Novgorod, Russia.

Education:

1999 - 2005: Ph.D., Physics; Texas A&M University.

1998: Master of Science, Physics; Nizhny Novgorod State University, Russia.

1996: Bachelor of Science, Physics; Nizhny Novgorod State University, Russia.

Honors and Awards:

2004 - Ethel Ashworth-Tsutsui Memorial Award for Research.

2004 - Division of Laser Science of American Physical Society Student Travel Grant for participation in the Frontiers in Optics 2004/Laser Science XX Conference, Rochester, New York, 10-14 October 2004.

2004 - Best Student Presentation, Texas Section Fall Meeting 2004, 7-9 October, Waco, Texas.

The typist for this thesis was Yelena Anatolyevna Kuznetsova.